



國立中山大學材料與光電科學學系

博士論文

以微米壓縮量測不同金屬玻璃微米柱之尺寸效應

Effects of Sample Size on Various Metallic Glass Micropillars

in Microcompression

研究生：賴炎暉 撰

指導教授：黃志青 博士

中華民國 九十八 年 十一 月

國立中山大學研究生學位論文審定書

本校材料與光電科學學系博士班

研究生賴炎暉（學號：D953060006）所提論文

以微米壓縮量測不同金屬玻璃微米柱之尺寸效應
Effects of Sample Size on Various Metallic Glass
Micropillars in Microcompression

經本委員會審查並舉行口試，符合博士學位論文標準。

學位考試委員簽章：

朱瑾

郭義清

黃志青

洪六文

何明

指導教授

黃志青
謝克昌

系主任/所長

謝誌

回顧這幾年來的研究生活，首先，我要感謝我的恩師 黃志青教授，在學期間承蒙老師對學業與研究上的殷勤指導和細心教誨，令我受益豐碩，此外老師的待人處事之道，也讓學生十分敬佩，並成為我學習效法的典範。另外，更衷心地感謝口試委員，何扭今教授、張六文教授、義守大學的鄭憲清教授以及台灣科技大學的朱瑾教授，在論文的審查以及口試過程中，給予學生許許多多寶貴的建議與指正，讓本論文更加完整充實。

也要感謝所上以及奈米中心的各實驗室的技術員，感謝你們在實驗上的指導與協助，尤其是電子顯微鏡技術員王良珠小姐、林明政先生、陳貴香小姐、歐傑電子能譜儀技術員施淑嫻小姐、X光繞射儀技術員李秀月小姐，以及聚焦離子束技術員陳彥文學長，由於你們的幫忙使得研究可以順利的進行。另外，感謝所辦朱惠敏小姐、顏秀芳小姐、陳秀月小姐在行政事務上的協助與幫忙，還有感謝熱心的華應麒大哥在生活上以及處事態度上的幫忙與教導。

更要感謝黃幫大大小小成員們的幫忙，尤其是敬仁學長在研究上的指導與協助，子翔、育誠、志溢以及友杰學長們的熱心教導，令我由衷感激，還有鴻昇、名哲、浩然、碩陽、大豪、哲男、聖堯、顛任、逸志、柏佑、婷婷實驗上的幫忙以及生活上的關心，讓我常常感到非常窩心。同時感謝得凱學長、研究所博士班同儕海明、俊宏以及弘杰、景強、俊誠等好友們的支持、陪伴與鼓勵，使我在學期間充滿歡樂不至於孤單寂寞，並帶給我許許多多美好的回憶。我的學長、學弟妹們以及諸位摯友，真的謝謝你們，還有感謝所有關心及幫助過我的人，或許我沒辦法一一記錄到你們，但我還是由衷的感謝你們。

最後，我要感謝我的家人，謝謝我的父母親給了我衣食無缺的生活，讓我沒有後顧之憂，全心全力的求學，也謝謝奶奶、叔叔以及我兩個可愛的弟弟，這段時間來的支持與鼓勵，謝謝你們我的家人。

賴炎暉 謹誌

於中山大學材料與光電科學學系

中華民國九十八年十一月

Table of Content

Table of Content.....	i
List of Tables.....	v
List of Figures.....	vii
Abstract.....	xvi
中文摘要	xviii
Chapter 1 Introduction.....	1
1-1 Amorphous alloys.....	1
1-2 The evolution of Mg-, Zr- and Au-based amorphous alloys	2
1-3 The sample size effect on amorphous alloys	5
1-4 Motives of this research.....	7
Chapter 2 Background and Literature Review	10
2-1 The history of amorphous alloys	10
2-2 The systems of amorphous alloys.....	12
2-3 The indices for predicting glass forming ability (GFA)	13
2-4 The main empirical rules for the synthesis of amorphous alloys	16
2-5 Properties and behaviors of amorphous alloys.....	19
2-5-1 Mechanical properties	19
2-5-2 Deformation mechanisms.....	20
2-5-3 Characterization of shear bands	22
2-5-4 Deformation behavior	23
2-5-5 Deformation model	26
2-6 Introduction of microcompression tests	28
2-6-1 Microsample preparation.....	29

2-6-2	Force application and measurement	32
2-6-3	Parameters of microcompression tests	32
2-6-4	Microscale characterization of mechanical properties	35
Chapter 3	Experimental Procedures	39
3-1	Materials	39
3-2	Sample preparation	40
3-2-1	Preparation for $Mg_{65}Cu_{25}Gd_{10}$	40
3-2-2	Preparation for $Zr_{63.8}Ni_{16.2}Cu_{15}Al_5$	41
3-2-3	Preparation for $Au_{49}Ag_{5.5}Pd_{2.3}Cu_{26.9}Si_{16.3}$	43
3-3	Property measurements and analyses	44
3-3-1	XRD and SEM/EDS characterization of as-cast ingots	44
3-3-2	Thermal analysis using DSC	44
3-3-3	Microstructure analysis using TEM	45
3-4	Microcompression test	45
3-4-1	Microcompression sample fabrication using FIB	45
3-4-2	Microcompression test using nanoindentation system	46
3-4-3	Morphology of deformed pillar samples	46
3-4-4	Microstructures of deformed pillar samples	47
3-5	High temperature microcompression test	47
3-5-1	MTS Nanoindenter XP system	48
3-5-2	Hysitron Triboindenter system	48
3-6	Nanoindentation measurements	49
3-6-1	Elastic modulus and hardness	49
3-6-2	Abrasive wear	50
Chapter 4	Experimental Results	51
4-1	XRD and SEM/EDS analysis	51

4-2	DSC analysis.....	51
4-3	TEM analysis.....	52
4-4	Microcompression test.....	54
4-4-1	Results for Mg ₆₅ Cu ₂₅ Gd ₁₀	54
4-4-2	Results for Zr _{63.8} Ni _{16.2} Cu ₁₅ Al ₅	56
4-4-3	TEM analysis of the microstructure in pillar sample	58
4-5	High temperature microcompression test.....	60
4-5-1	Results for Au ₄₉ Ag _{5.5} Pd _{2.3} Cu _{26.9} Si _{16.3} using MTS Nanoindenter	60
4-4-2	Results for Au ₄₉ Ag _{5.5} Pd _{2.3} Cu _{26.9} Si _{16.3} using Hysitron Triboindenter.....	62
4-6	Nanoindentation and nanoscratch test	63
4-6-1	Elastic modulus and hardness	64
4-6-2	Abrasive wear behavior.....	64
Chapter 5	Discussions.....	66
5-1	Room temperature microcompression test	66
5-1-1	Evolution of Young's modulus	66
5-1-2	Effect of FIB damage	68
5-1-3	Weibull statistics.....	69
5-1-4	Sample size and strain rate effect.....	71
5-1-5	Strain burst phenomena.....	73
5-1-6	Strain burst speed	75
5-2	High temperature microcompression test.....	78
5-2-1	Effect of temperature on mechanical behavior.....	78
5-2-2	Homogeneous flow	80
Chapter 6	Conclusions	83
References	86
Tables	97

Figures 113

List of Tables

Table 1.1	Fundamental properties and application fields of bulk metallic glasses and nanocrystalline alloys.....	97
Table 2.1	Bulk metallic glasses and their published year	98
Table 2.2	The classification of amorphous systems.....	99
Table 2.3	Summary of $\Delta T_x (=T_x - T_g)$, $T_{rg} (=T_g/T_l)$, $\gamma (=T_x / (T_g + T_l))$, critical cooling rate R_c and critical section thickness Z_c for typical bulk metallic glasses	100
Table 3.1	The constituent contents of alloy systems in this study	101
Table 3.2	Nanoscratch testing condition	102
Table 4.1	The composition analyses of the $Mg_{65}Cu_{25}Gd_{10}$, $Zr_{63.8}Ni_{16.2}Cu_{15}Al_5$ and $Au_{49}Ag_{5.5}Pd_{2.3}Cu_{26.9}Si_{16.3}$ amorphous alloys by SEM/EDS.....	103
Table 4.2	Thermal properties of the $Mg_{65}Cu_{25}Gd_{10}$, $Zr_{63.8}Ni_{16.2}Cu_{15}Al_5$ and $Au_{49}Ag_{5.5}Pd_{2.3}Cu_{26.9}Si_{16.3}$ amorphous alloys obtained from DSC	104
Table 4.3	Summary of the compressive stress/elastic modulus of $Mg_{65}Cu_{25}Gd_{10}$ (in at%) glass at different strain rates.....	105
Table 4.4	Summary of the compressive stress/elastic modulus of $Zr_{63.8}Ni_{16.2}Cu_{15}Al_5$ (in at%) glass at different strain rates.....	106
Table 4.5	Summary of the flow stress and deformation mode of the 1 μm Au-based BMG pillar samples at different temperatures with strain rate of $1 \times 10^{-2} s^{-1}$	107
Table 4.6	Testing conditions for the different pillar samples.....	108
Table 4.7	Pillar sample height change and thermal drift in microcompression tests.....	109
Table 4.8	Summary of the data measured using MTS NanoIndenter XP system.	110
Table 5.1	Summary of data measured using microcompression tests and nanoscratch tests	111

Table 5.2	Fitted parameters in Eq. (5-1) from the results of microcompression of the 3.8 μm Au-based BMG pillar samples.....	112
-----------	--	-----

List of Figures

Figure 1.1	Schematic illustrations showing atomic structures of (a) crystalline materials and (b) amorphous alloys. The inset in the lower left corner shows a diffraction pattern.....	113
Figure 2.1	The classification of amorphous alloy system (ETM = IV ~ VI group transition metal; LTM = VII ~ VIII group transition metal).....	113
Figure 2.2	Relationship between the critical cooling rate (R_c), maximum sample thickness (t_{max}) and reduced glass transition temperature (T_g/T_m) for bulk amorphous alloy systems	114
Figure 2.3	Relationship between the critical cooling rate (R_c), maximum sample thickness (t_{max}) and supercooled liquid range $\Delta T_x (= T_x - T_g)$ for bulk amorphous alloys	114
Figure 2.4	New parameter γ for understanding GFA of metallic glasses.....	115
Figure 2.5	The correlation between the R_c and γ_m for metallic glasses. Data were taken from the study of Lu et al.	115
Figure 2.6	The mechanisms for the stabilization of supercooled liquid and the high GFA for amorphous alloys which satisfy three empirical rules.....	116
Figure 2.7	The relationship between the tensile strength, Vickers hardness and Young's modulus for various bulk metallic glasses.....	117
Figure 2.8	Two-dimensional schematics of the atomistic deformation mechanisms in the amorphous alloys, including (a) a shear transformation zone (STZ) and (b) a local atomic jump	117
Figure 2.9	SEM micrograph of the sample surface for the $Zr_{59}Cu_{20}Al_{10}Ni_8Ti_3$ amorphous alloy under (a) compressive loading and (b) tensile loading.....	118

Figure 2.10	SEM micrograph of typical shear fracture surfaces for the $Zr_{52.5}Ni_{14.6}Al_{10}Cu_{17.9}Ti_5$ amorphous alloy under tensile loading (a)-(b); under compressive loading (c)-(d).....	118
Figure 2.11	Comparison between the glass transition temperature and calculated shear band temperature at fracture strength for different BMGs.....	119
Figure 2.12	Deformation map of a typical amorphous alloy	120
Figure 2.13	Strain-rate dependence of the flow stress (σ_{flow}) and viscosity (η) for the homogeneous deformation in the $La_{55}Al_{25}Ni_{20}$ amorphous alloy	120
Figure 2.14	Strain-strain curves of a $Zr_{52.5}Al_{10}Cu_{22}Ti_{2.5}Ni_{13}$ amorphous alloy at temperature of 683 K in strain rate change and constant strain rate tests	121
Figure 2.15	Serrated flow on stress-strain curve of the $Ni_{50}Pd_{30}P_{20}$ BMG.....	121
Figure 2.16	The typical p-h curve of the $Pd_{40}Cu_{30}Ni_{10}P_{20}$ amorphous alloy	122
Figure 2.17	Deformation map of the $Pd_{40}Ni_{40}P_{20}$ and $Mg_{65}Cu_{25}Gd_{10}$ amorphous alloys...	122
Figure 2.18	A diffuse shear transformation inside a spherical volume element, Ω_f , is favored at high temperatures	123
Figure 2.19	A more intense shear transformation inside a disk shaped volume element, Ω_f , is favored at low temperatures.....	123
Figure 2.20	Annular milling patterns have been used to mill a roughly defined micropillar sample of Ni single crystal	124
Figure 2.21	The microcompression samples were fabricated into (A) a Ni_3Al alloy and (B) Ni-based superalloy by using lathe milling program. The diameter of microcompression samples are 43 μm and 2.3 μm , respectivelys	124
Figure 2.22	(a) Schematic of the microcompression test setup; (b) A SEM micrograph with a flat diamond tip of 30 μm in size.....	125
Figure 2.23	Schematic of a cylindrical pillar and its base	126
Figure 2.24	Effect of fillet radius/pillar radius ratio on numerical simulation output. The	

	inset shows an enlargement of the circled region to facilitate comparison.....	126
Figure 2.25	(a) Deformed configuration of a circular cylindrical pillar with an aspect ratio $\alpha = 5$ at a strain of 0.1. (b) Deformed configuration of the pillar at the same strain of 0.1, but now considering friction. (c) Input and output stress-strain curves for a pillar with an aspect ratios $\alpha = 2-5$, both with friction and without friction (NF)	127
Figure 2.26	Effect of taper on numerical simulation output.....	128
Figure 2.27	Effect of misalignment of the system on the error in elastic modulus	128
Figure 2.28	(a) The microcompressive engineering stress-strain curve of the $\text{Ni}_{76}\text{Al}_{24}$ alloy with 2 μm diameter. (b) SEM micrograph of a micropillar after microcompression test. Strain bursts are indicated by arrows in figure (a), and appearance of slip lines are also observed on the micropillar surface, as also indicated by arrows.....	129
Figure 2.29	Engineering stress-strain curve obtained from the microcompression test of the 12 μm $\text{Mg}_{61}\text{Cu}_{28}\text{Gd}_{11}$ BMG.....	130
Figure 2.30	Micrographs of the micropillar, (a) before and (b) and (c) after microcompression test. (d) Close-up view showing the shear bands.....	130
Figure 2.31	(a) An SEM micrograph of the pillar sample with the diameter of 20 μm after microcompression test, and the corresponding fracture surface as shown in (b). (No evidence of localized melting or river pattern is apparent in fracture surface.)	131
Figure 2.32	SEM micrographs of the pillar samples with diameters of (a) 10 μm and 8 μm after microcompression test. (Global melting is observed in micropillar samples under microcompression test.).....	131
Figure 3.1	The flow chart of the experimental procedures.....	132
Figure 3.2	Photograph of the arc melting device.....	133

Figure 3.3	Schematic diagram of the arc melting device.....	134
Figure 3.4	The relationship of fusion heat among the constituent elements in the Zr-Cu-Ni-Al alloy system (unit: kJ/mol).....	135
Figure 3.5	The simulated phase diagram for a Zr-rich isothermal section calculated under constant 5 at% Al at 1050 °C.....	136
Figure 3.6	The simulated phase diagram for the composition cut between $Zr_5Ni_{40}Zr_{55}$ and $Al_5Cu_{25}Zr_{70}$, obtained from the isopleth C-C in Figure 3.5.....	136
Figure 3.7	Schematic diagram and photographs of the standard Nano Indenter [®] XP system	137
Figure 3.8	SEM micrographs of the flat-punch tip: (a) top view and (b) side view.....	138
Figure 3.9	SEM micrograph showing the projected area of the punch tip	138
Figure 3.10	Schematic of the microcompression setup. (Black region represents the flat punch indenter tip; the lower grey area represents the micropillar.)	139
Figure 3.11	Schematic illustration of TEM sample procedure using FIB	139
Figure 3.12	The photograph of the heating stage for MTS Nanoindenter XP system.....	140
Figure 3.13	The photograph of the heating stage for Hysitron Triboindenter system.....	140
Figure 3.14	The picture of Hysitron Triboindenter system.....	141
Figure 3.15	The photographs of the heating stage set-up: (a) the heating stage covered with a sheet of alumina-silica paper and (b) test samples attached with a thermal couple	142
Figure 3.16	Schematic diagrams of the standard scratch procedure.....	143
Figure 3.17	(a) A example of the worn scratch track (cross profile direction as indicated by arrow) and (b) a typical result of the cross-sectional profile.....	144
Figure 4.1	XRD patterns taken from the cross-sectional surface of the as-cast (a) $Mg_{65}Cu_{25}Gd_{10}$, (b) $Zr_{63.8}Ni_{16.2}Cu_{15}Al_5$ and (c) $Au_{49}Ag_{5.5}Pd_{2.3}Cu_{26.9}Si_{16.3}$ amorphous alloys.....	145

Figure 4.2	DSC thermograms of the as-cast (a) $Mg_{65}Cu_{25}Gd_{10}$, (b) $Zr_{63.8}Ni_{16.2}Cu_{15}Al_5$ and (c) $Au_{49}Ag_{5.5}Pd_{2.3}Cu_{26.9}Si_{16.3}$ amorphous alloys (heating rate of 40 K/min)....	146
Figure 4.3	TEM bright field image of the as-cast $Mg_{65}Cu_{25}Gd_{10}$ amorphous alloy with an inserted diffraction pattern	147
Figure 4.4	TEM bright field images of the as-cast $Zr_{63.8}Ni_{16.2}Cu_{15}Al_5$ amorphous alloy for two different regions with their corresponding diffraction patterns: (a) phase separation region and (b) glassy matrix region	148
Figure 4.5	Microstructure of the as-cast $Zr_{63.8}Ni_{16.2}Cu_{15}Al_5$ amorphous alloy for the phase separated region: (a) A bright field TEM image, (b) the corresponding selected area diffraction patterns of the bright and dark regions, and (c) HREM image of the interface denoted by the dotted circle in (b)	149
Figure 4.6	TEM bright field image of the as-cast $Au_{49}Ag_{5.5}Pd_{2.3}Cu_{26.9}Si_{16.3}$ amorphous alloy with an inserted diffraction pattern.....	150
Figure 4.7	SEM micrographs of pillars for the Mg-based BMG before microcompression test. The pillars with diameters of (a) 3.8 μm and (b) 1 μm . The tilt angle of the sample in SEM is 55° for both images	151
Figure 4.8	SEM micrographs of pillars for the Zr-based BMG before microcompression test. The pillars with diameters of (a) 3.8 μm , (b) 1 μm and (c) 700 nm. The tilt angle of the sample in SEM is 55° for all images.....	152
Figure 4.9	Compressive load-displacement curves of the Mg-based BMG of (a) 3.8 μm and (b) 1 μm at different strain rates	153
Figure 4.10	The engineering stress-strain curves of the Mg-based BMG of (a) 3.8 μm and (b) 1 μm at different strain rates	154
Figure 4.11	The displacement-time curves of the Mg-based BMG of (a) 3.8 μm and (b) 1 μm at different strain rates.....	155
Figure 4.12	SEM micrographs showing the appearance of deformed pillars for the	

	Mg-based BMG with the size and strain rate: (a) 3.8 μm , $\sim 6 \times 10^{-4} \text{ s}^{-1}$, (b) 1 μm , $\sim 2 \times 10^{-4} \text{ s}^{-1}$, (c) 3.8 μm , $\sim 1.2 \times 10^{-3} \text{ s}^{-1}$, (d) 1 μm , $\sim 1 \times 10^{-3} \text{ s}^{-1}$, (e) 3.8 μm , $\sim 1 \times 10^{-2} \text{ s}^{-1}$, and (f) 1 μm , $\sim 1 \times 10^{-2} \text{ s}^{-1}$	156
Figure 4.13	The microcompression engineering stress-strain curves of the 3.8 μm , 1 μm and 700 nm micropillars at different strain rates of (a) $1 \times 10^{-4} \text{ s}^{-1}$, (b) $1 \times 10^{-3} \text{ s}^{-1}$, and (c) $1 \times 10^{-2} \text{ s}^{-1}$	157
Figure 4.14	SEM micrographs showing the appearance of deformed pillars for the Zr-based BMG at a strain rate of $1 \times 10^{-4} \text{ s}^{-1}$: (a) 3.8 μm , (b) 1 μm , and (c) 700 nm.....	158
Figure 4.15	SEM micrographs showing the appearance of deformed pillars for the Zr-based BMG at a strain rate of $1 \times 10^{-3} \text{ s}^{-1}$: (a) 3.8 μm , (b) 1 μm , and (c) 700 nm.....	158
Figure 4.16	SEM micrographs showing the appearance of deformed pillars for the Zr-based BMG at a strain rate of $1 \times 10^{-2} \text{ s}^{-1}$: (a) 3.8 μm , (b) 1 μm , and (c) 700 nm.....	158
Figure 4.17	TEM sample preparation procedures: (a) Zr-based BMG micropillar with 1 μm diameter before compression test, (b) carbon is deposited around the pillar, (c) an energetic Ga ion beam is used to cut the trench, and (d) TEM sample can be further thinned by using the Ga ion beam with lower voltage or current. The tilt angle of the sample in SEM is 55° for all images.....	159
Figure 4.18	(a) Bright field TEM image of a lamella prepared from the undeformed Zr-based pillar. (b) A diffraction pattern from the indicated region of the pillar in figure (a), as marked by a circle. (c) The HREM image from the indicated region of the pillar in figure (a), as marked by a square.....	160
Figure 4.19	(a) The SEM image showing the 1 μm Zr-based BMG pillar sample. (b) The corresponding bright field TEM image. (c) A diffraction pattern from the indicated region of the pillar in figure (b), as marked by a circle. (d) The HREM image from the indicated region of the pillar in figure (a), as marked by a square.....	161

Figure 4.20	(a) The SEM image showing the 1 μ m Mg-based BMG pillar sample. (b) The corresponding bright field TEM image. (c) A diffraction pattern from the indicated region of the pillar in figure (b), as marked by a circle	162
Figure 4.21	SEM micrographs of pillars for the Au-based BMG before microcompression test. The pillars with diameters of (a) 3.8 μ m and (b) 1 μ m.....	163
Figure 4.22	Compressive load-displacement curves of the 1 μ m Au-based BMG pillar samples deformed at different temperatures.....	164
Figure 4.23	The time-displacement curves of the 1 μ m Au-based BMG pillar samples deformed at different temperatures.....	164
Figure 4.24	The engineering stress-strain curves of the 1 μ m Au-based BMG pillar samples deformed at different temperatures.....	165
Figure 4.25	SEM images of the 1 μ m Au-based BMG pillar sample (a) before and after compression at (b) room temperature, (c) 343 K, (d) 373 K, (e) 383 K and (f) 393 K	166
Figure 4.26	SEM images of the 1 μ m Au-based BMG pillar sample (a) (c) before and (b) (d) after compression at 403 and 408 K.....	167
Figure 4.27	The load-displacement curves from microcompression of the Au-based BMG pillar samples at high temperatures: (a) constant strain rate and (b) strain rate change tests	168
Figure 4.28	SEM images of a typical 3.8 μ m Au-based BMG pillar sample (a) before and (b) after compression at 395.9 K with strain rates of $3 \times 10^{-3} - 8 \times 10^{-3} - 5 \times 10^{-4} \text{ s}^{-1}$	169
Figure 4.29	True stress-strain curves from microcompression of the Au-based BMG pillar samples at high temperatures: (a) constant strain rate and (b) strain rate change tests	170
Figure 4.30	The typical load-depth curves of the Mg-, Au- and Zr-based BMGs at strain	

	rate of $5 \times 10^{-2} \text{ s}^{-1}$	171
Figure 4.31	(a) Scratch depth profile versus scratch length and (b) cross-sectional profile for the Mg-, Au- and Zr-based BMGs	172
Figure 4.32	SEM images of the scratched regions in the (a) beginning, (b) middle and (c) end of the scratch made in the Mg-based BMG	173
Figure 4.33	SEM images of the scratched regions in the (a) beginning, (b) middle and (c) end of the scratch made in the Au-based BMG	174
Figure 4.34	SEM images of the scratched regions in the (a) beginning, (b) middle and (c) end of the scratch made in the Zr-based BMG	175
Figure 5.1	Schematic illustration of the deformation for a tapered pillar sample	176
Figure 5.2	AES depth profile of the FIB milled Zr-based BMG micropillar with a diameter of $3.8 \mu\text{m}$	176
Figure 5.3	The strength-sample size relationship for (a) the Mg-based BMG, and (b) the Zr-based BMG samples with different pillar diameters from 3 mm down to $1 \mu\text{m}$, and from 2 mm down to 700 nm, respectively	177
Figure 5.4	The appearance of the $3.8 \mu\text{m}$ (a) Mg-based BMG and (b) the Zr-based BMG pillar sample after FIB milling	177
Figure 5.5	Schematic illustration of the sample size effect on homogeneous deformation	178
Figure 5.6	The SEM images of the Zr-based BMG pillar sample at the four different sizes: (a) $3.8 \mu\text{m}$, (b) $1 \mu\text{m}$, (c) 700 nm and (d) 300 nm in diameter	179
Figure 5.7	The SEM images showing the appearance of the three different 300 nm pillar samples: (a) (c) (e) before and (b) (d) (f) after compression	180
Figure 5.8	The comparison of the curves for the Mg- and Zr-based bulk compression samples, and the $1 \mu\text{m}$ Mg- and Zr-based micropillars, compressed at the strain rate of 10^{-4} s^{-1}	181

Figure 5.9	SEM micrographs showing the appearance of the deformed (a) Mg- and (b) Zr-based bulk compression samples.....	181
Figure 5.10	The function of temperature versus strength and modulus for the 1 μm Au-based BMG pillar samples at strain rate of $1 \times 10^{-2} \text{ s}^{-1}$	182
Figure 5.11	Stress vs strain rate for Au-based BMG pillar samples at different temperatures with curves fitted by Eq. (5-1).....	182
Figure 5.12	Strain-rate dependence of the viscosity in the Au-based BMG.....	183

Abstract

Over the past decades, bulk metallic glasses (BMGs) have attracted extensive interests because of their unique properties such as good corrosion resistance, large elastic limit, as well as high strength and hardness. However, with the advent of micro-electro-mechanical systems (MEMS) and other microscaled devices, the fundamental properties of micrometer-sized BMGs have become increasingly more important. Thus, in this study, a methodology for performing uniaxial compression tests on BMGs having micron-sized dimensions is presented.

Micropillar with diameters of 3.8, 1 and 0.7 μm are fabricated successfully from the $\text{Mg}_{65}\text{Cu}_{25}\text{Gd}_{10}$ and $\text{Zr}_{63.8}\text{Ni}_{16.2}\text{Cu}_{15}\text{Al}_5$ BMGs using focus ion beam, and then tested in microcompression at room temperature and strain rates from 1×10^{-4} to $1 \times 10^{-2} \text{ s}^{-1}$. Microcompression tests on the Mg- and Zr-based BMG pillar samples have shown an obvious sample size effect, with the yield strength increasing with decreasing sample diameter. The strength increase can be rationalized by the Weibull statistics for brittle materials, and the Weibull moduli of the Mg- and Zr-based BMGs are estimated to be about 35 and 60, respectively. The higher Weibull modulus of the Zr-based BMG is consistent with the more ductile nature of this system.

In additions, high temperature microcompression tests are performed to investigate the deformation behavior of micron-sized $\text{Au}_{49}\text{Ag}_{5.5}\text{Pd}_{2.3}\text{Cu}_{26.9}\text{Si}_{16.3}$ BMG pillar samples from room to their glass transition temperature ($\sim 400 \text{ K}$). For the 1 μm Au-based BMG pillars, a transition from inhomogeneous flow to homogeneous flow is clearly observed at or near the glass transition temperature. Specifically, the flow transition temperature is about 393 K at

the strain rate of $1 \times 10^{-2} \text{ s}^{-1}$.

For the $3.8 \text{ }\mu\text{m}$ Au-based BMG pillars, in order to investigate the homogeneous deformation behavior, microcompression tests are performed at 395.9-401.2 K. The strength is observed to decrease with increasing temperature and decreasing strain rate. Plastic flow behavior can be described by a shear transition zone model. The activation energy and the size of the basic flow unit are deduced and compared favorably with the theory.



中文摘要

在過去的幾十年中，塊狀金屬玻璃已經引起廣泛注意，由於它具備了許多優異的特性，例如良好的抗腐蝕能力、大的彈性能、高的強度以及硬度等等。然而，由於微機電系統以及其他微米尺度元件的出現，微米尺度下金屬玻璃的基本機械性質變得越來越重要。因此，本研究論文中，才會使用單軸微米壓縮測試技術在金屬玻璃上做分析。

不同尺寸大小之 $Mg_{65}Cu_{25}Gd_{10}$ 與 $Zr_{63.8}Ni_{16.2}Cu_{15}Al_5$ 金屬玻璃微米柱已經成功地藉由聚焦離子束來製備，接著以不同應變速率在室溫下進行微米壓縮測試。其結果發現，鎂基與鋇基金屬玻璃具有明顯的尺寸效應，也就是說當材料的尺寸變小時，其強度是呈現上升。而強度的上升也可以藉由 Weibull 方程式來做說明及統計，鎂基與鋇基金屬玻璃之 Weibull modulus 分別估算為 35 與 60。在鋇基金屬玻璃中測得較高 Weibull modulus 也符合這個成分的金屬玻璃比較具有延性之特性。

此外，藉由高溫微米壓縮系統研究微米尺度下 $Au_{49}Ag_{5.5}Pd_{2.3}Cu_{26.9}Si_{16.3}$ 金屬玻璃在室溫到其玻璃轉化溫度之變型行為。對於 $1\ \mu m$ 尺寸之金基金屬玻璃微米柱而言，發現在玻璃轉化溫度附近有一個明顯的轉變，其變形機制由不均勻的變形到均勻的變形。結果發現，這個明顯的轉變大約發生在應變速率 $1 \times 10^{-2}\ s^{-1}$ 以及溫度 393 K 下。

而對於 $3.8\ \mu m$ 尺寸之金基金屬玻璃微米柱而言，進一步利用高溫微米壓縮測試來研究金基金屬玻璃在溫度 395.9-401.2 K 下的均勻變形行為。其結果發現，微米尺度下金基金屬玻璃之強度隨溫度上升而下降；隨應變速率下降而下降。而塑性變形行為可以利用金屬玻璃之變形模型來做分析。其結果發現，變形時之活化能以及尺寸大小都可利用此變形模型推算出來，且經比較發現結果符合其理論。

Chapter 1 Introduction

1-1 Amorphous alloys

Amorphous alloys are also called liquid metals, non-crystalline metals, glassy metals or metallic glasses. It is well known that amorphous alloys differ from conventional metals in that they lack the periodicity of crystal structures. The atoms in the amorphous alloys are randomly arranged, also known as structure packing with short-range order, like the case of a liquid, rather than setting on a repeatable unit cell in the crystalline materials. Two schematic illustrations of atomic structures of amorphous alloys and crystalline materials are shown in [Figure 1.1 \[1\]](#). The absence of crystalline structure means that amorphous alloys also lack crystal defects, such as dislocations and grain boundaries. With no crystal defects, amorphous alloys exhibit extraordinary properties over their crystalline counterparts.

Early amorphous alloys were typically fabricated by rapid cooling from the liquid state with critical cooling rates of 10^5 - 10^6 K/s, which severely limits the sample thickness. The resulting ribbon or wire samples are used extensively as magnetic sensors and transformer cores [\[2, 3\]](#), but the small dimensions limit the potential of amorphous alloys as structural materials. Until the advent of bulk metallic glasses (BMGs), there has been a revival of early interest for use of these fascinating materials in structural applications.

During the last two decades, BMGs have been discovered in a wide range of metallic alloys, including Pd-, Zr-, Au-, Pt-, Mg-based, and so on. Among the unique properties of bulk metallic glasses, they include very high strength, large elastic strain limit, high hardness, perfect elastic behavior, high corrosion resistance, along with unusual combinations of other

engineering properties. Table 1.1 [4] depicts some fundamental properties and application fields of bulk metallic glasses.

1-2 The evolution of Mg-, Zr- and Au-based amorphous alloys

Among a large number of amorphous alloys systems, Mg-based amorphous alloys are of special interest due to their high strength to weight ratio, relatively low cost as well as the wide application as structural materials [5]. In addition, the Mg-based amorphous alloys, such as the Mg-TM-Ln (Ln = Lanthanide metal, M = Ni, Cu or Zn) systems, were found to have a wide supercooled liquid region and a higher glass forming ability by Inoue's group in 1980s [6, 7]. From that time, great efforts have been devoted to developing the Mg-based bulk metallic glasses.

In 1991, Inoue's group [8] successfully synthesized the bulk $Mg_{65}Cu_{25}Y_{10}$ amorphous alloy with a diameter up to 4 mm by copper mold casting. It is the first time that such Mg-based amorphous alloys were prepared in the bulk form. Subsequently, Inoue's group [9] found that the $Mg_{65}Cu_{25}Y_{10}$ BMG with increasing diameter up to 7 mm can be prepared by using high-pressure die casting method. Furthermore, Xi et al. [10] further proposed that $Mg_{65}Cu_{25}Gd_{10}$ alloy owns the best glass forming ability among the $Mg_{65}Cu_{25}RE_{10}$ (RE = La, Ce, Pr, Nd, Sm, Gd, Dy, Tb, Ho, Er and Yb) ternary BMG systems. That is to say, the $Mg_{65}Cu_{25}Gd_{10}$ alloy presents higher glass forming ability than the $Mg_{65}Cu_{25}Y_{10}$ alloy. Men et al. [11] also reported that the $Mg_{65}Cu_{25}Gd_{10}$ alloy has been increased to a maximum diameter of 8 mm by simply using Gd to substitute for Y in the $Mg_{65}Cu_{25}Y_{10}$ BMG. Nevertheless, the Mg-based BMGs with high glass forming ability have a drawback of lacking ductility; they can be regarded as a representative of brittle BMGs.

From the Zr-based BMGs considerations, in the early 1990s, Inoue et al. [12], Zhang et al. [13] and Peker et al. [14] developed a series of Zr-based BMGs that have a very low critical cooling rate and a large supercooled liquid region. For example, the $Zr_{65}Al_{15}Ni_{25}$ and $Zr_{65}Al_{7.5}Ni_{10}Cu_{17.5}$ amorphous alloys exhibit large supercooled liquid region which are 77 and 127 K, respectively. In addition, Inoue's group [15] produced the $Zr_{65}Al_{7.5}Ni_{10}Cu_{17.5}$ BMGs with a critical casting thickness of 16 mm by using water quenching a melt in a quartz tube. In 1992, Peker and Johnson [14] discovered a quaternary alloy based on Zr-Ti-Cu-Ni-Be, known as $Zr_{41.2}Ti_{13.8}Cu_{12.5}Ni_{10}Be_{22.5}$ (Vit 1), and this amorphous alloy system is the first commercial BMG. They also proposed that $Zr_{41.2}Ti_{13.8}Cu_{12.5}Ni_{10}Be_{22.5}$ in the form of rods ranging up to 14 mm in diameter can be fabricated by casting in silica containers.

Among various kinds of BMG systems, the Zr-based BMGs exhibit very high glass forming ability, excellent mechanical properties, high corrosion, and wear resistance. For example, $Zr_{41.2}Ti_{13.8}Cu_{12.5}Ni_{10}Be_{22.5}$ has the critical cooling rate (R_c) of 1 K/s for the formation of amorphous alloy and has unique mechanical properties, including large elastic strain-to-failure limit ($\epsilon_{el} = 2\%$) and high tensile yield strength ($\sigma_y = 1.9$ GPa). However, the Zr-based BMGs, as similar with other metallic glasses, fail through the formation of highly localized shear band at room temperature, resulting in little overall plasticity and low ductility.

In terms of the Au-based BMGs, the binary $Au_{75}Si_{25}$ amorphous alloy was first fabricated by Klement et al. [16] in the early 1960s. It is the first time that the Au-based amorphous alloys were prepared by a classic rapid-quenching technique. However, the critical cooling rate for the formation of this $Au_{75}Si_{25}$ alloy is of the order of 10^5 - 10^6 K/s and the resulting amorphous alloys geometry is limited to thin ribbons or sheets with a casting

thickness less than 50 μm . In 1968, to improve the glass forming ability of this alloy, Chen et al. [17] report that this $\text{Au}_{75}\text{Si}_{25}$ alloy can be moderately modified by using Ge to partially substitute for Si. But the limited sample size on Au-based amorphous alloy inhibited the scientific investigation or their applicability over the past several decades.

Up until 2005, based on the Au-Cu-Si alloy system, Schroers et al. [18] successfully prepared a set of Au-based amorphous alloys by copper mold quenching technique and these amorphous alloys show low liquidus temperature, large supercooled liquid region and good processibility. Among them, the $\text{Au}_{49}\text{Ag}_{5.5}\text{Pd}_{2.3}\text{Cu}_{26.9}\text{Si}_{16.3}$ amorphous alloy shows the best glass forming ability; furthermore, the maximum casting thickness exceeds 5 mm and the Vickers hardness of this alloy is about 350 H_v , twice of conventional 18-karat crystalline gold alloys. These excellent properties make the Au-based amorphous alloys attractive for many applications including electronic, medical, dental, surface coating and jewelry. However, their superior structural properties are also accompanied by brittleness caused by highly localized shear band, which greatly limits the applications of BMGs. Consequently, attempts to improve ductility have received more and more attention in recent years.

To overcome this limited plasticity, many researchers made attempts to develop an extrinsic composite microstructure within the glassy matrix [19-24], or an intrinsic structure, such as dual-phase BMGs or in situ precipitated nano-crystals [25-28]. The basic idea is effectively to block or hinder the propagation of shears bands during deformation. For example, based on the concept of developing a composite, Hays et al. [19] enhanced plasticity of Vit 1 BMG by containing in situ ductile phase dendrite dispersions. They found that upon cooling from high temperature melt, the Vit 1 alloy undergoes partial crystallization by nucleation and subsequent dendritic growth of β phase in the remaining liquid. The in situ ductile phase/BMG matrix composite exhibits up to 5% plastic strain (tensile and

compressive). For similar study, Johnson's group [21] has investigated a composite of $Zr_{57}Nb_5Al_{10}Cu_{15.4}Ni_{12.6}$ reinforced with a ductile metal particles such as Ta, Nb and Mo. The results show that the compressive strain-to-failure of the composite increased from 2% to 24%. Recently, Jang et al. [24] also reported that the typical brittle-natured Mg-based BMGs can be reinforced by the porous ductile Mo particles with a spherical shape and a size of 20-70 μm . This composite alloy exhibits superior mechanical performance with up to 10% compressive strain and 1100 MPa stress at room temperature.

In contrast, based on increasing Poisson's ratio and developing phase-separated microstructure, Liu et al. [28] enhanced plasticity of BMGs without additional ductile metal particles or annealing steps by choosing the appreciate alloy composition. They reported that extraordinarily plastic Zr-based BMGs could be obtained by the appropriate choice of their composition with the use of the Poisson's ratio strategy. The resulting Zr-based BMGs show that the "super plastic" BMGs are composed of hard regions surrounded by soft regions, which enables the glasses to undergo a true strain of more than 160%. Consequently, this enhanced plasticity of BMGs can be regarded as a representative of ductile BMGs.

1-3 The sample size effect on amorphous alloys

In the early days, the external sample dimensions were larger than the internal microstructural features, and the important of external size effects on mechanical properties could safely be ignored. With the advent of micro-electro-mechanical system (MEMS) and other microscale devices, it has resulted in components with sizes approaching microstructural dimension, and the external sample size effects have become increasingly more important.

The development of microscale experiments is critical to measure microscale mechanical properties and the mechanical size effects associated with these small-scale samples. According to the literature, the strength of the face-centered cubic (FCC) single crystals is known to be strongly dependent on sample dimension. For example, the strength of Ni or Au microsized single crystal specimens are several times higher than that of the bulk samples, and the strength can be further increased by more than one order of magnitude in submicron pillar samples [29, 30]. This dramatic size effect was proposed to be a result of the reduced sample size which is smaller than the characteristic length for dislocation multiplication, resulting in dislocation starvation.

In contrast, the BMGs do not deform by dislocation-mitigated processes; instead, the plastic deformation in BMGs at room temperature is highly localized within shear bands or shear transformation zones (STZs) [31-33]. According to a previous study by Zheng et al. [34], the sample size effects are expected for strength and plasticity behavior of bulk metallic glasses on several different levels and for different reasons. First, in view of strength, for brittle BMGs in particular, the variability of their strength is expected based on their flaw sensitivity. Thus, the probability of finding flaw is low in a small size scale sample, such that one can measure the reliable intrinsic yield strength.

Second, in view of plasticity, bending tests of metallic glass wires and thin plates usually indicate a considerable bending ductility [35]. It is well known that the high strength of monolithic bulk metallic glasses usually were accompanied by a virtually zero plastic strain in conventional compression test since the plastic deformation in metallic glasses is in the form of highly localized shear bands. The deformation mechanisms of metallic glasses will be discussed in details in the next background and literature review section. Once the onset of cracking is suppressed in the micro-sized deforming sample, the shear offset achievable in

even one single shear band may result in large plastic strains before failure. Thus, the low ductility, the major drawback of BMGs, becomes unimportant at small scales. It would be of interest to find out the magnitude of the shear band offset that can be obtained in microscaled samples, and observe the accommodation of large plastic strains when the bulk metallic glass sample is only micrometers in size.

1-4 Motives of this research

Bulk metallic glasses are considered as the potential materials for imprinting, molding and micro-electro-mechanical system because of their high strength, hardness, large elastic strain, high corrosion resistance and processing flexibility in the supercooled liquid region [36]. However, what are the characteristics of the fundamental mechanical properties, such as yield strength and plastic strain achievable of small-sized BMGs? Precise characterization of the mechanical properties at the small size is required for proper design and structure miniaturization. Up to now, there have been only limited quantitative measurements. Thus, intense efforts have been made to study the properties of micrometer-sized BMGs. In this study, three kinds of BMGs are fabricated to investigate different deformation mechanisms, listed below:

- (1) $\text{Mg}_{65}\text{Cu}_{25}\text{Gd}_{10}$ (the Mg-based BMG),
- (2) $\text{Zr}_{63.8}\text{Ni}_{16.2}\text{Cu}_{15}\text{Al}_5$ (the Zr-based BMG),
- (3) $\text{Au}_{49}\text{Ag}_{5.5}\text{Pd}_{2.3}\text{Cu}_{26.9}\text{Si}_{16.3}$ (the Au-based BMG).

First of all, it is of interest to examine the microscale compressive properties in the typical brittle Mg-based BMG and a much more ductile phase-separated Zr-based BMG. The sample size effect, strain rate effect and deformation mechanisms of the Mg- and Zr-based metallic glasses are discussed and compared to that of bulk samples later.

In addition, another purpose of this study is to gain the intrinsic yield strength by using microcompression testing. It is well known that BMGs are often accompanied by a virtually zero plastic strain in tension and limited plasticity in compression. There is no obvious macroscopic yielding, and the failure often occurs in the elastic region. If the failure occurs in the elastic region, the fracture strength would be smaller than the true yield strength. The limited plasticity makes it impossible to determine the intrinsic yielding strength of BMGs. Therefore, the quantitative compression test on the microscale sample would be needed to investigate the intrinsic mechanical properties of BMGs. The strength and plasticity of BMGs at small sample sizes are also examined in comparison with their behavior in conventional compression tests.

Hence, in order to clarify the deformation mechanisms of the Mg- and Zr-based metallic glasses, the microcompression test and scanning electron microscopy are conducted on small-sized samples with sample sizes from 700 nm, 1 μm to 3.8 μm . The possible deformation mechanisms and shear banding behavior are discussed.

Besides the fundamental mechanical properties of micrometer-sized BMGs, it is of interest to examine the relationship between sample sizes, temperature and strain rate for the micrometer-sized BMGs. It is crucial to understand the detailed deformation mechanism of BMGs at different temperatures so that their advantages can be fully utilized and their limitations understood. Especially, the deformation mechanism of BMGs in or near the glass transition temperature remains an important subject of investigations for practical applications, such as in micro-forming of MEMS application or in the field of near-net shape fabrication of structural components.

Therefore, the objective of this study is to systematically explore deformation mechanism over a wide range of test temperatures. Here we used the micrometer-sized Au-based BMG as an example, testing them under uniaxial compression at temperatures from room to its glass transition temperature. The material behavior is subsequently analyzed in more detail using the deformation model of BMG. The Au-based BMG is chosen as model material because of its low glass transition temperature and excellent resistance to oxidation at high temperatures.

Chapter 2 Background and Literature Review

2-1 The history of amorphous alloys

Since the amorphous alloys were first fabricated in the Au-Si system by a rapid solidification technique in the early 1960s [16], a great number of scientists and engineers have paid much attentions to fabricate the new amorphous alloy systems. However, the rapid solidification technique requires high cooling rates above 10^5 - 10^6 K/s for glass formation and the resulting amorphous alloys geometry is limited to thin ribbons, foils or sheets with a thickness less than about 50 μm . In 1969, Chen and Turnbull [37] successfully prepared an amorphous alloy of the Pd-Si-X (X= Ag, Cu or Au) ternary system. Subsequently, Chen [38] synthesized the ternary Pd-Cu-Si alloy in 1974 by using the simple suction-casting methods at a significantly lower cooling rate of 10^3 K/s, and the maximum diameter of Pd-Cu-Si metallic glass was 1 mm. If one arbitrary defines the millimeter scale as bulk, the first bulk metallic glass (BMG) was the ternary Pd-Cu-Si amorphous alloy prepared in 1974.

In 1982, Drehman et al. [39] successfully prepared the well-known $\text{Pd}_{40}\text{Ni}_{40}\text{P}_{20}$ amorphous alloy with 5 mm diameter by using RF induction melting and subjecting the specimens to surface etching followed by a succession of heating and cooling cycles. A few years later, Kui et al. [40] reported that the $\text{Pd}_{40}\text{Ni}_{40}\text{P}_{20}$ amorphous alloy could be made by using boron oxide fluxing method to purify the melt and to eliminate heterogeneous nucleation. They successfully improved the critical casting thickness from 5 mm to 10 mm by processing the Pd-Ni-P melt in a boron oxide flux.

More and more amorphous alloys were fabricated by various preparation methods. In

the 1980s, a variety of solid-state amorphization techniques, which are completely different mechanisms from rapid quenching, such as mechanical alloying [41], ball milling [42], diffusion induced amorphization in multilayer [43], ion beam mixing [44], hydrogen-induced amorphization [45] and inverse melting [46] were developed.

In the late 1980s, Inoue's group [47, 48] in Tohoku University of Japan succeeded in finding many new multicomponent amorphous alloy systems consisting mainly of common metallic elements and the rare earth materials with Al and ferrous metals with lower critical cooling rates. They found extraordinary glass forming ability in La-Al-Ni and La-Al-Cu alloy systems [47]. By casting the alloy melt in water-cooling Cu molds, the cylindrical samples with diameters up to 5 mm or sheets with similar thickness were made fully glassy in the $\text{La}_{55}\text{Al}_{35}\text{Ni}_{20}$ alloy, and the later $\text{La}_{55}\text{Al}_{25}\text{Ni}_{10}\text{Cu}_{10}$ alloy was fabricated with a diameter up to 9 mm by the same method.

In 1990s, some similar alloys with rare-earth metals partially replaced by the alkali-earth metal Mg, such as Mg-Y-Cu, Mg-Y-Ni, etc., were also developed by the Inoue's group [8, 49], along with a family of multicomponent Zr-based bulk metallic glasses (e.g. Zr-Cu-Ni, Zr-Cu-Ni-Al BMGs) [15]. The Inoue's group further developed $\text{Pd}_{40}\text{Cu}_{30}\text{Ni}_{10}\text{P}_{20}$ alloy system in 1997, and the results showed that the $\text{Pd}_{40}\text{Cu}_{30}\text{Ni}_{10}\text{P}_{20}$ amorphous alloy has lower melting temperature (T_m) and higher reduced glass transition temperature (T_g/T_m) as compared with those for the $\text{Pd}_{40}\text{Ni}_{40}\text{P}_{20}$ amorphous alloy. The difference in T_m and T_g/T_m indicate the possibility that the glass forming ability is considerably larger for the new Pd-Cu-Ni-P alloy. The largest critical casting thickness could reach to 72 mm in the $\text{Pd}_{40}\text{Cu}_{30}\text{Ni}_{10}\text{P}_{20}$ alloy system [50]. In 2002, based on the Pd-Cu-Ni-P alloy, Nishiyama et al. [51] further reported that the critical cooling rate for glass formation for the $\text{Pd}_{42.5}\text{Cu}_{30}\text{Ni}_{7.5}\text{P}_{20}$ alloy can be markedly decreased to be 0.067 K/s by fluxing treatments.

But owing to the cost and heavyweight of the Pd-based alloys, the low-cost and lightweight metallic glasses with the aim of meliorating the specific strength were the developing emphasis. It is apparent that the metallic glasses were developed in the sequence beginning with the expensive metallic Pd- and Pt-based, followed by less expensive Zr-, Mg-, Ti- and Ni-based bulk metallic glasses. Furthermore, it can be seen that the much cheaper Mg- and Zr-based BMGs were recently developed and had attracted extensive interests.

2-2 The systems of amorphous alloys

According to Inoue's study [48], the system of amorphous alloy can roughly be divided into nonferrous and ferrous alloy systems as shown in Table 2.1. The nonferrous alloy systems are Mg-Ln-M (Ln = lanthanide metal, M = Ni, Cu or Zn), Ln-Al-TM (TM = VI-VIII group transition metal), Zr-Al-TM, Zr-Ti-Al-TM, Ti-Zr-TM, Zr-Ti-TM-Be, Zr-(Nb, Pd)-Al-TM, Pd-Cu-Ni-P, Pd-Fe-Ni-P, Ti-Zr-Ni-Cu-Sn and Ti-Zr-Ni-Cu-(Si, B) systems. However, the ferrous alloy systems comprise Fe-(Al, Ga)-metalloid, (Fe, Co, Ni)-(Zr, Nb, Nb)-B, Fe-Co-Ln-B, Ni-Ti-P and Ni-Nb-(Cr, Mo)-(P, B) alloys. Table 2.1 lists typical bulk amorphous alloy systems reported since 1988 up to date and the year in which they were first published. It is observed that the ferrous alloy systems have been found after the synthesis of the nonferrous alloy system.

In terms of the features of the alloy components, the alloy components are classified into five groups summarized in Table 2.2 and Figure 2.1 [48]. The first group (i) comprises ETM (or Ln), Al and LTM, such as Zr-Al-Ni and Ln-Al-Ni alloy systems. The second group (ii) consists of LTM, ETM and metalloid as exemplified for Fe-Zr-B and Co-Nb-B alloy systems. The third group (iii) is LTM (Fe)-(Al, Ga)-metalloid systems and fourth group (iv) is

indicated by Mg-Ln-LTM and ETM (Zr, Ti)-Be-LTM alloy systems. However, the fifth group (v) as Pd-Cu-Ni-P and Pd-Ni-P systems are composed only of two kinds of group element (LTM and metalloid), which are different from the combination of the three types of group elements for the alloys belonging to the four previous groups.

2-3 The indices for predicting glass forming ability (GFA)

Glass forming ability (GFA) is essential for understanding the origin of the glass formation and also important for designing and developing new bulk glassy compositions. It is generally believed that the GFA of an amorphous alloy initially determined by the critical cooling rate (R_c). The high cooling rate was used to suppress the nucleation of a crystalline phase and to obtain the fully amorphous alloy. That is to say, the smaller R_c , the higher the GFA of a system should be. However, the critical cooling rate is a parameter that is difficult to measure accurately. Moreover, R_c can only be determined once the composition of the bulk metallic glass is known. Thus, it is necessary to establish a simple and reliable parameter that correlates well with GFA.

A great of scientific effort has therefore been devoted to searching for a proper GFA measure for metallic glasses. As a result, many GFA parameters or criteria have been proposed to reflect the relative GFA among BMGs on the basis of the characteristic temperatures measured by differential thermal calorimetry (DSC) or differential thermal analysis (DTA).

One of the GFA parameters is the reduced glass transition temperature T_{rg} ($= T_g/T_m$, where T_g and T_m are the glass transition temperature and melting point, respectively) was developed by Turnbull et al. [52]. They found that there is a clear tendency for GFA to

increase with increasing T_g/T_m , as shown in Figure 2.2. However, a refined parameter taking T_g and T_l (the liquidus temperature) into account was proposed by Lu et al. [53, 54]. According to Lu's results, the reduced glass temperature T_{rg} ($= T_g/T_l$) shows a better correlation with GFA than that given by T_g/T_m for BMGs. In view of T_{rg} , T_l is dependent on composition, choosing the suitable concentration near the eutectic point so that the probability of being able to cool fast through the supercooled liquid region without any crystallization. In other words, the T_l can also be used to indicate the relative stability of stable glass-forming liquids; the lower T_l the larger stability of the liquid (i.e., the liquid can remain stable to a lower temperature with no nucleation of any crystalline phase).

Apart from T_{rg} , another important parameter is the supercooled liquid range, $\Delta T_x (= T_x - T_g)$, which is equal to the difference between the onset temperature of the first crystallization peak (T_x) and the glass transition temperature. It is well known that the supercooled liquid range ΔT_x determined upon devitrification is a quantitative measure of the stability of the supercooled range. Therefore, a large ΔT_x value may indicate that the undercooled liquid can remain stable in a wide temperature range without crystallization, and has a high resistance to the nucleation and growth of crystalline phase. Figure 2.3 reveals that the relationship between R_c , t_{max} (maximum sample thickness) and ΔT_x [48]. One can see a clear tendency that GFA increases with increasing ΔT_x .

Although both T_{rg} and ΔT_x are used as indicators for the GFA of metallic glasses, they show contrasting trends versus GFA in many alloy systems. For example, Waniuk et al. [55] showed that T_{rg} correlated well with GFA in Zr-Ti-Cu-Ni-Be alloy system whereas ΔT_x had no relationship with GFA. Another example occurs in Cu-Zr-Ti and Cu-Hf-Ti ternary systems reported by Inoue et al. [56]. On the contrary, it was found that the T_{rg} was not reliable enough to infer relative GFA in $Pd_{40}Ni_{40-x}Fe_xP_{20}$ ($x = 0 \sim 20$) [57], Fe-(Co, Cr, Mo, Ga,

Sb)-P-B-C [58] and Mg₆₅Cu₁₅M₁₀Y₁₀ (M = Ni, Al, Zn and Mn) [59] amorphous alloy systems. Thus, further investigation is necessary to obtain a better and more precise parameter to reflect the GFA of bulk metallic glasses.

In 2002, a new parameter γ , defined as $T_x / (T_g + T_l)$, was proposed by Lu and Liu [60], and the definition of γ is shown in Figure 2.4 [61]. They found that the parameter γ showed better coherence for judging the GFA than T_{rg} among metallic glasses. Table 2.3 presents the summary of ΔT_x , T_{rg} and γ calculated for some typical conventional metallic glasses [60]. In addition, the relationship between γ , the critical cooling rate R_c (K/s) and section thickness Z_c (mm) can be expressed as follows:

$$R_c = 5.1 \times 10^{21} \exp(-117.19\gamma), \quad (2-1)$$

$$Z_c = 2.80 \times 10^{-7} \exp(41.70\gamma). \quad (2-2)$$

These two equations can be used to estimate R_c and Z_c when γ is measured readily from DSC/DTA measurements. Furthermore, the γ parameter has been successfully applied to glass formation in the bulk Fe-Nd-P amorphous alloy.

In 2007, a modified γ parameter, defined as $\gamma_m = (2T_x - T_g) / T_l$, has been established by Du et al. [62]. Based on a report by Du et al., the overall liquid phase stability is positively related to the quantity of $(T_x - T_g) / T_l$, where the parameter T_x is proportional to the crystallization resistance. The γ_m parameter also reflects the effects of T_x , T_g and T_l which are basically measured upon devitrification of amorphous materials, the same as the previous γ parameter. An excellent linear relation of R_c is clearly observed, as shown in Figure 2.5. In order to compare the efficiency of the different GFA parameters, the statistical correlation factor, R^2 , has been evaluated by using the data reported by Lu and Liu. Therefore, γ_m parameter reveals an excellent correlation with the GFA of metallic glasses, with the

statistical correlation factor of $R^2=0.931$. From the results obtained so far, the γ_m parameter seems to be promising for determining the GFA of an alloy.

2-4 The main empirical rules for the synthesis of amorphous alloys

Ever since the discovery of metallic glasses by Klement and coworkers [16], various methods developed to fabricate bulk metallic glasses were mostly empirical in nature, but researchers gradually began to understand that the proper choices of elemental constituents would lead to metallic glasses exhibiting critical cooling rate as slow as 1~100 K/s. It is well known that the three empirical rules for forming bulk metallic glasses were proposed by Inoue. According to Inoue's research [49, 63-65], the three empirical rules comprise: (1) multicomponent systems consisting of more than three elements; (2) significant difference in atomic sizes with the size ratios above about 12% among the three elements; and (3) negative heats of mixing among the three main constituent elements. Inoue claimed that the metallic glasses satisfying the three empirical rules have special atomic configurations in the liquid state which are significantly different from those of the corresponding crystalline phases. In addition, the three empirical rules can also be clarified by the thermodynamics, kinetics and structure aspects, and these factors will be discussed below.

Firstly, in terms of thermodynamics, bulk metallic glasses usually exhibit a lower ΔG (Gibbs free-energy) than their corresponding crystalline states. It has generally been found that high GFA is favored by small values of ΔG . From general thermodynamic equation, ΔG can be expressed as $\Delta G = \Delta H_f - T\Delta S_f$, where ΔH_f and ΔS_f are the enthalpy and entropy of fusion, respectively. One can tell that a low ΔG implies a small enthalpy of fusion ΔH_f and large entropy of fusion ΔS_f . The large ΔS_f is expected to associate with multicomponent alloys because ΔS_f is proportional to the number of component. Besides, the low ΔH_f

signifies that the negative heats of mixing among the three main constituent elements. From the thermodynamics considerations, the negative heat of mixing is referred to the fact that the distinct atoms tend to bond together.

Secondly, in terms of kinetics, the parameter such as nucleation rate of crystalline phase has a significant influence on the GFA in the supercooled region. In 1969, Turnbull [66] suggested that the homogeneous of nucleation (I) and growth (U) of a crystalline phase with a spherical shape from the supercooled liquid can be written as

$$I = \frac{10^{27}}{\eta} \exp\left[\frac{-b\alpha^3\beta}{T_r^3(\Delta T_r)^2}\right] [\text{mm}^{-3}\text{s}^{-1}], \quad (2-3)$$

$$U = \frac{10^3 f}{\eta} \left[1 - \exp\left(\frac{-\beta T_r}{T_r}\right)\right] [\text{mm s}^{-1}], \quad (2-4)$$

where η is viscosity, b is a constant determined by the nucleus shape, T_r is the reduced temperature ($=T/T_m$), ΔT_r is equal to $1-T_r$ and f is the fraction of nucleus sites at the growth interface. Besides, α and β are dimensionless parameters related to liquid/solid interfacial energy (σ); these parameters can be defined as:

$$\alpha = \frac{(N_0 V^2)^{1/3} \sigma}{\Delta H}, \quad (2-5)$$

$$\beta = \frac{\Delta S}{R}. \quad (2-6)$$

Here, N_0 , V and R are the Avogadro's number, the atomic volume and the gas constant, respectively. In these relationships, the important parameters are η , α and β . The increase of these three parameters will decrease the I and U values, and further leads to an increase of GFA. In addition, the increase of α and β indicates the increase in σ and ΔS and decrease in ΔH . The results are consistent with the interpretation of achieving high GFA derived from the thermodynamics considerations. Another notable parameter is $\alpha\beta^{1/3}$, one can see that the

supercooled liquid with $\alpha\beta^{1/3} > 0.9$ would practically not crystallize at any undercooling. In contrast, it should be practically impossible to suppress the crystallization of supercooled liquid for which is small, e.g. $\alpha\beta^{1/3} < 0.25$.

Thirdly, in terms of structure, the atomic configuration of bulk metallic glasses also plays an important role for the designing new amorphous alloy systems. From the Hume-Rothery rule [67], an extensive solid solubility of one metal in another only occurs if the sizes of the metals differ by less than 15%. On the other hand, the difference in atomic size ratios above 15% will lead to a complex structure which makes crystallization less easily. In addition, the GFA of amorphous alloys tends to increase as more components are added to the amorphous alloys. That is also called the confusion principle which implies that a larger number of components in an amorphous alloy system destabilize competing crystalline phases which may form during cooling. The most straightforward evidence can be observed that the difference in the densities between BMG and fully crystallized state from the density measurements. Such small difference in values indicates that the bulk metallic glasses have higher dense randomly packed atomic configurations.

By the way, the amorphous alloys with the three empirical rules always have very deep eutectic valleys with low melting temperatures, leading to the appearance of high T_g/T_m and large ΔT_x . Therefore, a high thermal stability of undercooled liquid for amorphous alloys which satisfies the three empirical rules is observed. Therefore, one can regard the alloy compositions with the deep eutectics as the fourth empirical rule.

According to the above discussions, the BMGs were found to have new type of supercooled liquid with high solid/liquid interfacial energy (i.e., the liquid can suppress the nucleation of a crystalline phase). This new type of supercooled liquid also has the difficulty

of atomic rearrangement, leading to a decrease of atomic diffusivity and an increase of viscosity. Accordingly, the liquid can have high T_g . The supercooled liquid also has the necessity for atomic rearrangements on a long-range scale for crystallization, which causes the suppression of growth of a crystalline phase. These mechanisms for the stabilization of supercooled liquid and the formation of bulk metallic glasses are summarized in [Figure 2.6](#) [48].

2-5 Properties and behaviors of amorphous alloys

In addition to the importance of fundamental sciences of BMGs, it is important to clarify the properties and behaviors of BMGs. It is well known that BMGs exhibit unique properties such as high yield strength, excellent wear and corrosion resistance, high fracture toughness and outstanding castability [49, 68-70]. Among all of the unique properties, mechanical properties are the most important subject in applications as engineering materials. The mechanical properties, deformation and fracture mechanisms of BMGs as well as the characterization of shear bands will be discussed in the following section.

2-5-1 Mechanical properties

Since the high degree of dense randomly packed atomic configuration, when the stress is applied, the amorphous alloys allow small atomic displacement to resist deformation. Due to the absence of crystal-slip mechanisms for plastic deformation, the amorphous alloys always show very high strength values. For example, [Figure 2.7](#) shows the relationship between the tensile strength, Vickers hardness and Young's modulus for various bulk metallic glasses together with the data on conventional crystalline alloys [48]. According to these diagrams, the amorphous alloys have high tensile strength of 840-2100 MPa and Young's modulus of

47-102 GPa which depends on the alloy compositions. Hence, it can be summarized that amorphous alloys have much higher tensile strength and much lower Young's modulus. The significant difference in the mechanical properties is believed to be a reflection of the difference in the deformation and fracture mechanisms between BMGs and conventional crystalline alloys.

2-5-2 Deformation mechanisms

Unlike the conventional crystalline alloys, the amorphous alloys do not exhibit long-range order structures; therefore, the local rearrangement of atoms in amorphous alloys is relatively high-energy or high-stress process than those for the crystalline alloys. Two schematic illustrations of local rearrangement are depicted in [Figure 2.8 \[33\]](#). The first deformation mechanism for amorphous alloys is originally proposed by Argon et al. [\[71\]](#) on the basis of an atomic-analog bubble-raft model. According to [Figure 2.8\(a\)](#), a shear displacement occurs to accommodate an applied shear stress τ , with the darker atoms moving with respect to the lower atoms. This deformation mechanism is also called flow defect, τ defect [\[72\]](#), local inelastic transition [\[73\]](#) and shear transformation zone (STZ) [\[74-78\]](#).

Over the past decades, a considerable number of studies have been made on the development of an STZ theory of plastic deformation in amorphous alloys [\[74-78\]](#). The STZ is essentially a small cluster of randomly close-packed atoms that spontaneously and cooperatively rearrange under the action of an applied shear stress. The size of an STZ is predicted to comprise a few to perhaps ~ 100 atoms from the results of simulation and a variety of indirect experimental measurement. For example, on the basis of classical molecular dynamics (MD) computer simulation, the size of an STZ is about 120 atoms in the Cu-Ti glass system under pure shearing [\[79\]](#). Besides, it is worth noting that an STZ is not a

structural defect in the amorphous alloys in the way that a lattice dislocation is a crystal defect. That is to say, an STZ is an event defined in a local volume, not a feature of the glass structure.

Another deformation mechanism for amorphous alloys is the classical free-volume model, as shown schematically in [Figure 2.8\(b\)](#) [33]. This model was proposed by Turnbull and co-workers [80, 81] and applied to the case of amorphous alloy deformation by Spaepen [31]. This model regards deformation as a series of discrete atomic jumps in the amorphous alloy; these jumps are obviously favored near sites of high free volume which can more readily accommodate them. Based on the diffusion-like character of the process, the activation energy for diffusion is usually on the order of $\sim 15-25 kT_g$ which k and T_g are the Boltzmann constant and glass transition temperature, respectively [81]. If the deformation in amorphous alloys were driven by local diffusive-like jumps, then one can expect a bias from gradients in pressure or normal stress, such as driven diffusional flow in polycrystalline materials. Although it is not clear why local diffusive jumps would be biased by shear stresses, the free-volume model introduces a simple model to allow constitutive laws to be developed on the basis of competing free volume creation and annihilation.

Despite the differences in the STZ-type and the diffusive-jump-type model, these atomic-scale mechanisms share the following common features [33]: (1) They show characteristics of a two-state system; forward jumps or STZ operations compete with backward ones, and these can occur at the same spatial position in sequence. (2) They are thermally activated, and exhibit similar energy scales. (3) They are dilatational; not only is transient dilatation required at the saddle point configuration, but a semi-permanent free-volume increase is presumed to accumulate locally after the operation of either mechanism.

2-5-3 Characterization of shear bands

As the stress increases, local diffusive jumps or STZ operations become active and connect to form shear bands in which the plastic strain is localized. The example of the morphology of the shear bands is shown in [Figure 2.9 \[82\]](#). Although shear bands are found in other materials, such as polycrystalline alloys [\[83\]](#), they are particularly important in amorphous alloys. The shear-band-evolution process is critical for understanding the failure mechanisms, determining the ductility and improving the mechanical properties of BMGs. According to the TEM results [\[84-89\]](#), the shear bands in amorphous alloys are only 10-100 nm thick, which is quite small in comparison with shear bands in crystalline metals, 10-100 μm thick [\[90\]](#). In addition, the deformation in amorphous alloy is always accompanied by a substantial increase in temperature and a corresponding drop in viscosity within the shear bands.

So far as viscosity concerned, the viscosity drop may result in forming the vein pattern and even liquid-like droplets on fracture surface. For example, one interesting feature can be seen on the fracture surfaces, as shown in [Figure 2.10 \[82\]](#). Although the mechanism for this viscosity drop is still under debate, it is important to understand the mechanism of the shear bands for the improvement of mechanical properties.

Besides, it is well known that the shear bands are thin, moving fast and short-lived. Thus it is not easy to measure this temperature rise directly. According to the infrared measurements, the temperature rise in shear bands is clearly observed by Yang et al. [\[91\]](#). However, the spatial and temporal resolution of this technique is too low to allow accurate determination of the evolution in shear bands. Thus Lewandowski et al. [\[92\]](#) invented a

clever and simple way to improve the resolution. They coated the amorphous alloy sample with a thin layer of fusible tin, and observed that after deformation, the tin near the shear bands had beaded up because it had melted. This fusible-coating method allows the measurement of local heating in shear bands, with spatial and temporal resolution far exceeding the infrared measurements. Based on their results, they also found that the width of the hot zone is at least 100 nm.

Another interesting issue, based on the calculation of heat conduction theory and STZ modeling, is that Yang et al. [93] proposed that the temperature of shear bands after deformation is apparently similar to their glass transition temperature (T_g) for a number of amorphous alloy systems. These results provide a new criterion to determine the strength of BMGs from their T_g , and reveal the fact that catastrophic failure of BMGs is caused by the sudden drop in viscosity inside the shear band when the temperature approaches T_g . The calculated shear-band temperature at the fracture strength for different BMGs is shown in Figure 2.11 [93].

2-5-4 Deformation behavior

The plastic deformation of amorphous alloys is essentially a biased accumulation of local strains incurred through the operation of STZ and the redistribution of free volume. Generally speaking, the plastic deformation of amorphous alloys can be divided into two different modes [31]:

- (1) Homogeneous deformation,
- (2) Inhomogeneous deformation.

A deformation mechanism map, constructed firstly by Spaepen in 1977, of a typical

amorphous alloy in stress-temperature axes is shown in [Figure 2.12 \[31\]](#). Homogeneous deformation of amorphous alloys occurs at low stresses and at temperatures near or above the glass transition temperature ($T > 0.7 T_g$) at which temperature amorphous alloys may be thought of as the viscous flow. That is, amorphous alloys are homogeneously deformed in both space and time. This property, easy forming abilities in a viscous state at elevated temperatures around the glass transition temperature, promises applications in the field of near-net shape fabrication of structural components [\[94-99\]](#).

In addition, the region of homogeneous deformation can be further classified into three parts depending on the viscosity of the material [\[31\]](#). First, as T is above T_i , the viscosity of material is about $10^{-3} \text{ Nm}^{-2}\text{s}$ and this material can be regarded as the “fluid” matter. Since the viscosity changes only slowly with temperature, the strain rate contours of [Figure 2.12](#) in this region are almost horizontal. Secondly, as T is close to T_g , the viscosity of material is in the range of 10^{15} - $10^{10} \text{ Nm}^{-2}\text{s}$ and this material can be called as the “viscous” matter. In this region, the viscosity falls very steeply with increasing temperature and the strain rate contours of [Figure 2.12](#) are almost vertical. Thirdly, as T is lower than T_g , the viscosity of material is higher than $10^{15} \text{ Nm}^{-2}\text{s}$ and this material is called as the “solid” matter.

In homogeneous deformation mode, their mechanical behavior has two characteristic features. The first is the smooth transition from the Newtonian (i.e., viscosity independent of strain rate) to non-Newtonian flow (i.e., viscosity decreases with increasing strain rate) [\[100-102\]](#). In the other words, homogeneous flow is an ideal Newtonian flow and strain rate sensitivity m value equals to 1, except at high strain rates. For example, [Figure 2.13](#) exemplifies the strain-rate dependence of the flow stress and viscosity for the homogeneous deformation in the $\text{La}_{55}\text{Al}_{25}\text{Ni}_{20}$ amorphous alloy at various temperatures [\[101\]](#). According to [Figure 2.13\(a\)](#), the flow stress increased with increasing strain rate and curves shifted towards

higher strain rates with increasing temperature. Furthermore, as seen in [Figure 2.13\(b\)](#), the higher strain rates led to a decrease in the viscosity, showing the smooth transition from the Newtonian to non-Newtonian flow. The second is the possible existence of stress overshoots or undershoots during the compression or tension tests [\[103-107\]](#). A typical example of the stress-strain behavior is shown in [Figure 2.14](#) [\[107\]](#). As shown in [Figure 2.14](#), stress overshoots or undershoots are detected after the strain rate increases or decreases, respectively. Generally speaking, stress overshoots are often observed in amorphous alloys deformed at high strain rates as a result of the creation of excessive free volume during deformation.

In contrast to the homogeneous deformation, inhomogeneous deformation usually takes place at low temperatures ($T \ll T_g$). In this region, the stress is very strain rate insensitive, so that this flow has a horizontal strain rate contours in [Figure 2.12](#). The inhomogeneous deformation is characterized by the formation of localized shear bands with a thickness of ~ 10 nm [\[89\]](#), followed by unstable fracture. The activation and propagation of individual shear bands will give rise to serrated flow in the stress-strain curve during uniaxial compression testing. A typical example of serrated flow is shown in [Figure 2.15](#) [\[108\]](#). The serrated flow phenomenon was firstly reported by Chen et al. [\[109\]](#) in 1973. From that time, the serrated flow during the inhomogeneous deformation in amorphous alloys was widely investigated. In 2001, Wright et al. [\[110\]](#) assumed that the formation of each shear band is manifested in a single serration, and performed the detailed analysis of shear band by using linear variable differential transformers (LVDTs) to study the time duration of displacement burst. Similar, more and more scientists adopt nanoindentation measurements to analyze the inhomogeneous deformation [\[111-117\]](#). Golovin et al. [\[111\]](#) found some discontinuous pop-in displacement bursts in the load-depth (P-h) curve by using the nanoindentation test, as shown in [Figure 2.16](#). They suggested that pop-in displacement bursts were associated with the formation of

highly localized shear bands.

However, in 2004, Schuh et al. [118] performed nanoindentation measurements on the Pd₄₀Ni₄₀P₂₀ and Mg₆₅Cu₂₅Gd₁₀ amorphous alloys and proposed a new “homogeneous II” regime in the deformation map of an amorphous alloy, where the deformation rate exceeds the characteristic rate of shear band nucleation. In other words, they suggested the existence of a transition in the plastic flow from inhomogeneous deformation flow at lower strain rates to homogeneous deformation flow (marked by homogeneous II) at high strain rates at low temperatures. Therefore, the simultaneous operation of multiple shear bands leads to macroscopically more homogeneous flow (i.e. disappearance of pop-in events). The homogeneity of the homogeneous deformation II is in time rather than in space. Based on this, Schuh et al. further constituted a deformation map for amorphous alloys as shown in Figure 2.17 [118].

2-5-5 Deformation model

For the aforementioned, homogeneous deformation of amorphous alloys usually take place at high temperatures and their thermomechanical behavior has various characteristic features. Up to now, homogeneous deformation of amorphous alloys can be described in various ways or different equations [31, 32, 100, 101, 119, 120]. Among these approaches, Spaepen’s free volume model [31] and Argon’s shear transformation zones (STZ) model [32, 119] seem to be widely accepted and successively used in homogeneous deformation of amorphous alloys. Based on these two models, the strain rate during homogeneous deformation of BMG can be described by

$$\dot{\varepsilon} = \alpha \varepsilon_0 \nu_G \exp\left(-\frac{\Delta F}{kT}\right) \sinh\left(\frac{\sigma V}{2\sqrt{3}kT}\right), \quad (2-7)$$

where α is the steady state fraction of matter capable of undergoing shear transformations, ν_G is the normal mode frequency of the flow unit along the activation path, $\alpha\varepsilon_0\nu_G \sim 10^{11} \text{ s}^{-1}$ [119], kT has its usual meaning, and V is the activation volume ($V=\nu_0\varepsilon_0$, in which ν_0 is the volume of a flow unit or STZ which undergoes a strain ε_0 (~ 0.125 [31, 119]) during deformation). And, Eq. (2-7) can also be written as

$$\dot{\varepsilon} = \dot{\varepsilon}_T \sinh\left(\frac{\sigma V}{2\sqrt{3}kT}\right), \quad (2-8)$$

here $\dot{\varepsilon}_T = \alpha\varepsilon_0\nu_G \exp(-\Delta F/kT)$ is a temperature-dependent rate constant. Thus, based on stress versus strain rate data, the various parameters of deformation model, such as the activation volume, energy and STZ volume, can be determined from fitting Eq. (2-8).

In respect of the activation energy ΔF (or the Helmholtz free energy barrier), the relationship between activation energy and elastic constants can be expressed as

$$\Delta F = \left[\left(\frac{7-5\nu}{30(1-\nu)} + \frac{2(1+\nu)}{9(1-\nu)} \right) \varepsilon_0 + \frac{1}{2} \frac{\tilde{\tau}}{\mu} \right] \mu V, \quad (2-9)$$

where ν is the Poisson's ratio, $\tilde{\tau}$ is the ideal shear resistance, μ is the shear modulus, and $\tilde{\tau}/\mu \sim 0.03$ [119]. Thus, the activation energy can be theoretically estimated from Eq. (2-9).

Recently, the activation volume, energy and STZ volume have been examined by using various deformation conditions, such as compression [105, 107, 121-125], tension [103, 126], indentation [127], creep [128, 129], thermomechanical analysis (TMA) [130], and so on. From these studies, the general tendency is that the activation volume is nearly temperature independent near the glass transition temperature; moreover, the larger activation energy is always accompanied by the larger activation volume (or STZ volume). To take a simple

example, Bletry et al. [107] demonstrated that the activation volume of the $Zr_{52.5}Cu_{22}Ni_{13}Al_{10}Ti_{2.5}$ amorphous alloys are measured to be 193-206 \AA^3 at the different elevated temperatures near the glass transition temperature. For similar study, Lee et al. [130] reported that the activation volume of the $Cu_{47.5}Zr_{47.5}Al_5$ amorphous alloys is observed to decrease slightly from 167 to 162 with increasing temperature from 703 K (near the glass transition temperature) to 733 K. That is to say, from these two examples, the activation volume is nearly independent of temperature. Furthermore, Lee et al. [130] and Fu et al. [125] suggested that the larger value of the measured activation energy value is directly correlated with a larger activation volume.

In addition, Argon et al. [119] pointed out that STZ is in a spherical shape during homogeneous deformation, as illustrated in Figure 2.18. On the other hand, during inhomogeneous deformation, the STZ is in a disk shape not a spherical shape, as shown in Figure 2.19. Thus, based on this concept, one can further estimate the radius of STZ volume during the homogeneous deformation.

2-6 Introduction of microcompression tests

Microcompression tests, developed by Uchic et al. in 2004 [29], were first applied to examine the mechanical properties of micrometer sized sample of single crystal of Ni, intermetallic alloy of $Ni_3Al-1\%Ta$ and Ni superalloy single crystal. It is the detailed study of the sample size effects on mechanical properties, published in the highly prestigious journal, Science, and known as “sample dimensions influence strength and crystal plasticity”. By this technique, focused ion beam (FIB) and nanoindentation system are two important instruments for fabricating the micrometer sized compression samples and for examining the mechanical properties. Compared with common microscale tests, microcompression tests have following

advantages: (1) the microcompression samples remain attached to the substrate and easy to handle; (2) the microcompression samples are loaded with the commercial nanoindentation system; (3) the fabrication of microcompression samples by the FIB can be scripted and automated. Therefore, this technique has been used for the investigation of sample size effects on the mechanical properties of single crystals of metals and alloys. These methodologies are discussed in the following section.

2-6-1 Microsample preparation

It is well known that the FIB systems are popular in the material science applications, such as advanced circuit editing, transmission electron microscopy (TEM) sample preparation and pattern machining. A finely focused beam of Ga ions operated at 30 keV is generally used for site-specific milling. In terms of micropillar, FIB is uniquely suited to fabricate micrometer sized compression samples at the surface of a bulk material, and the FIB milling can be classified into two main types based on recent literatures as below:

- (a) Annular-milling method,
- (b) Lathe-milling program method.

According to the approach developed by Uchic et al. [131], the microscale compression sample preparation process usually consists of two steps. In the first step, rough etching with a high beam current of Ga ions is used to mill the outer crater and outline a pillar. In this step, it is important to fabricate a large crater to make sure that the flat punch indenter will contact the pillar of interest. Additionally, this step is usually performed by using high current (5~20 nA) of the FIB, since the goal is to quickly remove the material around the sample of interest. In the second step of the milling process, a series of concentric annular milling pattern by a finer beam current are made to reach the final desired diameter. For example, the microscale

sample of Ni single crystal was roughly fabricated by the present method, as shown in [Figure 2.20 \[131\]](#).

In [Figure 2.20](#), one can see that micropillar samples are tapered due to the convergence angle of the Ga ion beam. It is possible to minimize such taper by adjusting the annular milling patterns and decreasing the beam current, but it is nearly impossible to produce perfect micropillar samples that have both a uniform cross-section and well-defined gage length by using this method alone. Thus, Uchic et al. [\[131\]](#) further modified this FIB milling fabrication process, as described below.

In order to eliminate the taper of the microcompression sample, which is resulted from the annular milling pattern process, the sample fabrication process needs to be involved in tilting the sample so that the angle between the pillar and the plane of the sample surface is as small as possible. Once the sample is tilted, the FIB can be employed to mill the side of the microcompression sample with a fine beam current (0.1-3 nA). Therefore, one can imagine that this approach can be repeated to lathe off the taper through a 360° trimming with rotating the sample in a small angular increments (5-10°) and keeping the sample in a fixed tilt angle (2-5°). However, this approach is tedious and monotonous, so Uchic et al. [\[131\]](#) further developed the software program to lathe off the sample. The program has the built-in image-recognition functions to perform this task without user supervision.

By this approach, the lathe-milling program is usually set to perform at least two complete steps around the sample. First, relatively higher beam currents (1-7 nA) are used to mill the sample to the approximate shape for the first step, and then finer beam currents (0.05-1 nA) are used for subsequent step. To take a simple example, microcompression samples of Ni₃Al alloy and Ni-based superalloy that have been fabricated by using this

fabrication methodology are shown in [Figure 2.21 \[131\]](#). One can clearly observe the circular pattern on the top surface of the microcompression sample, and it is a fiducial mark used as a reference point to reorient the specimen during the incremental milling and unit rotation process. And that this fiducial mark is half to the size of the expected sample diameter. Generally speaking, the lathe-milling program method was used to fabricate samples with the diameter of larger than 2 μm . Microcompression samples smaller than 2 μm in diameter are not prepared by the lathe milling program due to the difficulty in milling well-defined circular fiducial markers with the diameter of smaller than 0.5 μm . Thus, the very small microcompression samples are fabricated by using only the annular milling pattern method. To date, these two methods have commonly been used to prepare microcompression samples in a variety of materials and intermetallic alloys such as Ni or Au single crystal, Ni nanocrystalline Ni_3Al -1%Ta intermetallic alloy, Ni-based superalloy, Ni_3Al alloy and Mg- or Pd-based metallic glasses. Although the FIB milling can be operated with extreme accuracy, the rate of milling must be considered in fabricating microscale pillars as well. Generally speaking, the milling rates are typically about 1000 $\mu\text{m}^3\text{min}^{-1}$ [\[132\]](#) so microscale sample preparation requires a judicious use of the FIB milling technique.

Besides, there are other micro-machining methods such as micro-electrodischarge machining (micro-EDM), femto-second laser ablation, micro-electron-chemical milling and photolithography methods [\[133, 134\]](#). Those are used at slightly larger length scale relative to the previous mentions of two FIB milling methods. In terms of micro-electrodischarge machining, it is a critical technology to fabricate high-aspect-ratio 3D microscale samples. However, the surfaces of microscale samples fabricated by micro-electrodischarge machining will exhibit micro-cracks, resulting in stress concentration and reduction of fatigue strength. For the micropillar preparation, the FIB milling technique seems to be the best choice at present.

2-6-2 Force application and measurement

Once the micropillars are fabricated, the samples are then tested in uniaxial compression by using a flat punch tip in a commercially available nanoindentation system (MTS Nano indenter XP or Hysitron Triboindenter). Due to the conventional nanoindenter system with subnanometer displacement resolution and load resolution of 1 nN, it makes the technique popular in many applications such as the measurement of mechanical properties of thin films and tribological measurements of coatings. In particular, modified nanoindentation plays an important role in performing the microcompression test because the use of a flat punch tip enables the diamond indenter to act as a compression platen. The flat punch tip is also truncated by using FIB, and the schematic description of microcompression test is shown in [Figure 2.22 \[135\]](#).

2-6-3 Parameters of microcompression tests

According to the two-dimensional and three-dimensional finite element modeling, Zhang et al. [\[136\]](#) have made recommendations regarding allowable fillet radius to pillar radius ratio and aspect ratios, as well as the effect of pillar taper and misalignment of the system. Examples of these issues are described below.

The first point to be discussed is the geometric factors, such as the fillet radius r_c (or the curvature at the bottom of the pillar connecting to the base), the pillar aspect ratio α (defined as the height/diameter ratio) and the pillar taper. And the schematic of a cylindrical pillar and its base are shown in [Figure 2.23 \[136\]](#). First, a series of experiments is conducted to investigate the fillet radius/pillar radius ratio on the output stress-strain curve. An aspect ratio

of 2 is set in all of the simulations with fillet radius. The input stress-strain curve and the output stress-strain curves from the simulations with different fillet radiuses ($r_c = 0.1r$, $0.2r$, $0.5r$, and r) are shown in Figure 2.24 [136]. From the diagram, one can see that all the simulated output curves are above the input curve, and there is a greater error in the larger fillet radius. For example, based on the largest fillet radius/pillar radius ratio, i.e., $r_c/r = 1$, the error in flow stress from microcompression test is about 6% as compared with the input data. This result indicates the overestimate of the flow stress of the material in the plastic region, and the flow stress depends on the fillet radius/pillar radius ratio.

There is another issue, however, that needs to be addressed that the distribution of the von Mises stresses in the pillar and the base for various fillet radius/pillar radius ratios (r_c/r). The results show that with increased r_c/r , the stress concentration at the fillet is alleviated. For example, there is no obvious stress concentration at the fillet in the case of $r_c/r > 0.5$. It is well known that the stress concentrations may result in localized sample failure prior to yielding. Thus, the choice of r_c/r needs to be considered in two issues. One needs a small r_c/r to accurately obtain material behavior in the plastic region, and the other requires large r_c/r to avoid localized failure at the pillar root. In the 2D simulations, the value of r_c/r in the range of 0.2-0.5 is the optimum condition for microcompression test. Therefore, this suggests that if the r_c/r is well controlled, the microcompression test can still be used to probe the mechanical properties of materials.

The second important geometric factor is the pillar aspect ratio α . According to the 2D simulation [136], the aspect ratio of the pillars has a relatively small effect on the output flow stress curves when the aspect ratio is larger than 2. But if the aspect ratio is smaller than 2, the output strain hardening of the pillar deviates from the input value. The reason is that the constraint will result from the pillar base during the microcompression test. However, from

the 3D microcompression simulations, the friction between the indenter and the pillar top is considered. Figure 2.25(a) [136] shows a numerical image of a circular cylindrical Al pillar with an aspect ratio of 5 at a strain of 0.1 s^{-1} . Severe buckling is observed, which affects the corresponding stress-strain curve of the pillar. In contrast, Figure 2.25(b) [136] shows an image of the same pillar as shown in Figure 2.25(a) [136] at the identical strain rate of 0.1 s^{-1} , but with friction included in the simulation. No buckling is observed. In the microcompression test, it is usually performed without applying lubrication to the interface between the indenter tip and the pillar top. Figure 2.25(c) [136] displays the input and output stress-strain curves for pillar aspect ratio $\alpha = 2-5$. Due to the plastic buckling one can see that the stress-strain curve exhibits leveling off or stress drop. The results indicate that the plastic buckling is suppressed by the friction when the aspect ratio is less than 5. Hence, for both 2D and 3D simulation results, Zhang et al. [136] recommended the aspect ratio of pillars being around 2-3.

The third important geometric factor is the taper of the pillar. The angle of taper is defined by the tangent of the pillar wall to the pillar axis, and often the top surface of the pillar is smaller than the bottom of the pillar. The input curve and the output curves with four conditions (aspect ratio of 2 with and without taper; aspect ratio of 5 with and without taper) are shown in Figure 2.26 [136]. From the diagram, one can see that the output curve is very close to the input data when $\alpha = 2$ without taper. However, the measured elastic modulus is obviously larger than the input data by 10-60% if the pillar is tapered with a value of 20:1, corresponding to the taper angle of $\sim 2.86^\circ$. Therefore, the effects of taper result in overestimated elastic modulus and thus should be minimized by well control of FIB or micromachining conditions.

Finally, another important factor that may affect the accuracy of microcompression tests

is the effect of misalignment of the system. This misalignment means the angle between the end-surface normal of the flat punch indenter tip and the pillar axis. It is believed that the misalignment effect is manifested primarily in the deviation of the elastic region of stress-strain curve, giving rise to an underestimate of the elastic modulus of the material. From the 3D simulation, the effect of misalignment on measured elastic modulus is shown in [Figure 2.27 \[136\]](#). The results indicate that the measured elastic modulus decreases with increasing misalignment. It is noteworthy that the lower elastic modulus even for perfect alignment ($\theta = 0^\circ$) is due to the compliance of the pillar base. Therefore, the effect of misalignment significantly affects the test accuracy by underestimating the elastic modulus, and excessive misalignment may result in buckling of the pillar.

2-6-4 Microscale characterization of mechanical properties

Uchic et al. [\[29\]](#) have developed a unique test method to explore sample size effects on single crystal of Ni, intermetallic alloy of Ni₃Al-1%Ta and Ni superalloy single crystal. Samples with diameters from 0.5 to 40 μm and aspect ratios from 2:1 to 4:1 are tested in microcompression, using a nanoindentation with a flat punch tip and strain rates from 10^{-3} to 10^{-4} s^{-1} . The results showed that the Ni microcompression samples having diameters ranging from 20 to 40 μm were similar to those for bulk samples, but smaller samples (5 μm) displayed large strain bursts and considerably higher flow strengths. Sample size effects were even more dramatic in the experiments conducted on the Ni₃Al-1%Ta alloy, whose strength increased from 250 MPa for a 20- μm -diameter sample to 2 GPa for a 0.5- μm -diameter sample. By comparison, in the case of Ni superalloy single crystal, a 10- μm -diameter sample displayed the same behavior with the bulk tension test. The Ni superalloy contains very fine precipitates that provide the strong internal hardening mechanisms and preempt the influence of the external dimensions. Since then, a large number of researches on the sample size

effects have received considerable attentions. Following studies are presented in chronological order.

In 2005, Greer et al. [137] reported the significant increase in strength of microscale Au samples was observed, and the strength increased more than one order of magnitude in submicron pillar samples. They explained these high strengths in microcompression to be an indication of dislocation starvation. In their results, the dislocations were believed to pass through the sample free surface and out of the crystal before they had an opportunity to interact and multiply. Another notable result was that Greer et al. [137] developed an alternative fabrication technique based on lithographic patterning and electroplating. Their results on microspecimen fabricated by both FIB milling and lithographic patterning and electroplating indicate that the strength increase is not an artifact during the sample preparation process. In the similar study Volkert et al. [30] had also examined sample size effects in submicron pillar sample and attributed their results to source-limited behavior in small volumes.

In 2006, Uchic and co-workers [138] demonstrated the microscale compressive behavior of the $\text{Ni}_{76}\text{Al}_{24}$ alloys by means of microcompression tests. They found that the events of strain burst are observed in the stress-strain curves of microscale samples. The strain burst means that the strain (or displacement) takes place almost instantly. An example of strain bursts occurred during microcompression test is shown in Figure 2.28. SEM micrograph analysis indicates that the number of observable slip bands is approximately the same as the number of slip events.

In 2006, the microscale compressive properties of electrodeposited nanocrystalline Ni were examined by Schuster et al. [139]. They showed that the maximum yield strength was

1498 MPa for the 20 μm diameter sample. The similar study of the Mo-10Al-4-Ni alloy was reported by Bei and co-workers [140] in 2007. The results showed that the micropillars all yielded, regardless of the size, at a critical resolved shear stress of $G/26$, where G is the shear modulus. It is interesting to note that $G/26$ is in the range expected for the theoretical strength, from $G/30$ to $G/10$.

To date, the microcompression tests on single-phase metals have generally shown distinct size effects, the yield and flow strengths increase with decreasing pillar diameter. These dramatic effects are attributed to dislocation starvation because the size of the sample is smaller than the characteristic length scale of dislocation multiplication.

In contrast, plastic deformation in bulk metallic glass is not controlled by dislocation motion. The plastic deformation of BMGs at room temperature proceeds in the form of highly localized shear bands. Yielding is induced by shear band nucleation and propagation. The first study of the sample size effect in metallic glasses was by Zheng et al. [34], who examined mechanical properties in $\text{Mg}_{61}\text{Cu}_{28}\text{Gd}_{11}$ amorphous alloy system. The result revealed that the strength of Mg-based BMGs was sensitive to the sample size. Specifically, the strength is higher with a smaller size sample. The stress-strain curve from the microcompression tests is plotted in Figure 2.29. It is notable that the catastrophic fracture does not occur for the microscale sample with the overall plastic strain exceeding 3.2%, as shown in Figure 2.30.

Subsequently, Schuster et al. [141] demonstrated that the size effects of the $\text{Pd}_{40}\text{Ni}_{40}\text{P}_{20}$ BMGs were moderate increases of $\sim 9\%$ in the 0.2% offset yield stress of the microscale samples in comparison to those observed for bulk counterparts. The results were not the same with those observed for Ni or Au single crystal. Schuster et al. [141] interpreted that this

moderate increase in strength was attributed to the decreases in the defect population in the microscale samples, but not caused by the sample size effect. An additional surprising observation in the fracture morphology showed that the fracture surface of small samples was planer, facet free, no vein pattern and droplets, as shown in [Figure 2.31](#). It is not similar to the fracture morphology exhibiting a characteristic “vein” or “river” pattern in typical BMGs. Schuster et al. [\[141\]](#) explained that this phenomenon may imply that these microscale samples were not able to develop fully shear bands.

Recently, Cheng et al. [\[142\]](#) employed microcompression tests on the $Zr_{57}Ti_5Ni_8Cu_{20}Al_{10}$ BMGs and found that the melting of microscale samples was observed under a higher strain rate ($\sim 10^{-3} \text{ s}^{-1}$), as shown in [Figure 2.32](#). And it was not the same to the results discovered by Schuster’s group. Besides, the yield stress observed was higher than that measured in conventional compression testing of the same amorphous alloy sample, consistent with the recently reported microcompression results on crystalline materials [\[139\]](#).

Chapter 3 Experimental Procedures

The multicomponent alloys with the designed compositions of $\text{Mg}_{65}\text{Cu}_{25}\text{Gd}_{10}$, $\text{Zr}_{63.8}\text{Ni}_{16.2}\text{Cu}_{15}\text{Al}_5$ and $\text{Au}_{49}\text{Ag}_{5.5}\text{Pd}_{2.3}\text{Cu}_{26.9}\text{Si}_{16.3}$ are examined in this study. The $\text{Mg}_{65}\text{Cu}_{25}\text{Gd}_{10}$ bulk metallic glasses are fabricated by the arc melting plus injection casting method. The $\text{Zr}_{63.8}\text{Ni}_{16.2}\text{Cu}_{15}\text{Al}_5$ and $\text{Au}_{49}\text{Ag}_{5.5}\text{Pd}_{2.3}\text{Cu}_{26.9}\text{Si}_{16.3}$ are fabricated by the arc melting plus suction casting method. The composition of the $\text{Mg}_{65}\text{Cu}_{25}\text{Gd}_{10}$, $\text{Zr}_{63.8}\text{Ni}_{16.2}\text{Cu}_{15}\text{Al}_5$ and $\text{Au}_{49}\text{Ag}_{5.5}\text{Pd}_{2.3}\text{Cu}_{26.9}\text{Si}_{16.3}$ alloys are analyzed by scanning electron microscopy (SEM) equipped with energy dispersive X-ray spectrometry (EDS). The microstructure and glassy nature of samples are identified by X-ray diffraction (XRD) and transmission electron microscopy (TEM). The thermal stability of the samples is examined by differential scanning calorimetry (DSC) with heating rates of 40 K/min. Furthermore, room temperature compression tests are conducted on the bulk rod samples to characterize the mechanical properties by an Instron 5582 universal testing machine. With regard to microscale mechanical properties, the microscale samples are subjected to microcompression tests. The deformed sample appearances after the compression tests are investigated by SEM. The flow chart of experimental procedures is shown in [Figure 3.1](#).

3-1 Materials

The elements used in this study were purchased from Well Being Enterprise Co., Ltd, Taipei, Taiwan. The purities of the elements are of concern; that magnesium is as pure as 99.9%, copper is as pure as 99.99%, gadolinium is as pure as 99.9%, zirconium is as pure as 99.99%, nickel is as pure as 99.9%, aluminum is as pure as 99.99%, gold is as pure as 99.99%, silver is as pure as 99.99%, palladium is as pure as 99.99% and silicon is as pure as

99.99%. The constituent contents of the alloys in atomic and weight percentages (at% and wt%) prepared in this study are shown in [Table 3.1](#).

3-2 Sample preparation

3-2-1 Preparation for $\text{Mg}_{65}\text{Cu}_{25}\text{Gd}_{10}$

To synthesize the multicomponent alloy, three main methods are applied in this study. One is arc melting, another is induction melting, and the other is injection casting. First of all, a Cu-Gd master alloy is initially prepared by arc melting of pure Cu and Gd (99.99% for Cu and 99.9% for Gd) under an argon atmosphere. The applied device is the Centorr Series 5 Bell Jar Single Arc Furnace, as shown in [Figure 3.2](#). The operating current is about 200-300 A and the maximum temperature is 3500 °C (3773 K). The schematic diagram for arc melting furnace is illustrated in [Figure 3.3](#).

Before the starting of arc melting, in order to avoid the occurrence of crystallization due to the oxygen impurities, the argon needs to be continuously purged into the furnace to flush the oxygen and to ensure a low oxygen vapor pressure environment inside the furnace. Besides, cold water also needs to pour into and to flow through the bottom of the copper mold to increase the heat exchange rate. Finally, the chosen component placed on the bottom of the copper mold will be melted by the high voltage arc under a titanium getter argon atmosphere. It should be repeated for more than four times to confirm the homogeneous mixing of composition.

The Cu-Gd master alloy is then melted with Mg (99.9%) in an iron crucible by using induction melting. The crucible needs to be sprayed a thin boron nitride layer to avoid the

interaction between alloy and crucible at high temperatures. Then the argon atmosphere is maintained to 1 atm in order to suppress the generation of Mg vapor and the loss of the constituent accuracy. After complete melting, the alloys are poured into a water-cooled copper mold under an argon atmosphere. The process of beforehand casting could ensure complete mixing between elemental components and is favorable to fabricate the BMGs by the injection casting method since master alloys prepared by first casting could decrease the melt temperature during injection casting.

Finally, test samples are fabricated by placing an appropriate amount of the Mg-Cu-Gd master alloy in a quartz tube and remelted under an argon atmosphere, followed by injection melting into a water-cooled copper mold with an internal cylindrical-shaped cavity of 3 mm in diameter. In the same way, the quartz tube needs to be sprayed a thin boron nitride layer to avoid the interaction between alloy and quartz tube at high temperature, and the argon atmosphere is also added to 1 atm in order to suppress the generation of magnesium vapor.

3-2-2 Preparation for $Zr_{63.8}Ni_{16.2}Cu_{15}Al_5$

Prior to describing the experimental procedure of $Zr_{63.8}Ni_{16.2}Cu_{15}Al_5$, it is necessary to understand how to predict exactly the optimum composition of an alloy with two micro-scaled glassy phases. The detailed approaches are presented below. Furthermore, the relationship of heat of fusion among the constituent elements in the Zr-Cu-Ni-Al alloy system is shown in [Figure 3.4 \[143\]](#).

According to the literatures, Yan et al. [\[144\]](#) have successfully used a computational-thermodynamics approach to predict the potential compositions of Zr-Ti-Ni-Cu alloys with low-lying-liquidus surface which favors glass formation. These

calculated compositions of Zr-Ti-Ni-Cu alloys are noted to be in good agreement with those determined experimentally by Lin and Johnson [145]. Hence, this approach, building on information from the lower order constituent binaries and ternaries, can be used as a valuable tool for predicting the compositions of multicomponent alloys which exhibit a great tendency for BMG formation. The similar study for Nb-Hf-Si ternary system was also presented by Yan et al. in 2003 [146].

However, before applying the method on the Zr-Cu-Ni-Al system, we need to employ a “thermodynamic description” concept on the basis of the description of a multicomponent system obtained by the Calphad approach [147-150]. The term “thermodynamic description” means that the parameters of the thermodynamic models for all phases in a system in question are available. Consequently, the thermodynamic description of the higher order multicomponent systems can be predicted from the lower order constituent systems, i.e. binaries and ternaries.

According to the study of Du et al. [151], for the quaternary Zr-Cu-Ni-Al system, there are use six constituent binaries and four constituent ternaries. Thus, the thermodynamic description for the quaternary Zr-Cu-Ni-Al system can be obtained by extrapolation based on the descriptions of the lower order systems. Using this description and the commercial software Pandat [152], we can calculate the isotherms and isopleths.

For the quaternary system, the calculated isotherm is a tetragonal volume under a constant pressure, and a two-dimensional section can be obtained from cutting with constant Al content. This will provide the information for the selection of alloy compositions. In this study, the selected “X” alloy ($Zr_{63.8}Ni_{16.2}Cu_{15}Al_5$) within the two immiscible liquid phase region (L1 and L2) is shown in Figure 3.5, and it is the isothermal section in the Zr rich

corner under a constant 5 % Al content at 1050 °C (1323 K). The isopleth C-C cut in [Figure 3.5](#) is calculated between $\text{Al}_5\text{Ni}_{40}\text{Zr}_{55}$ and $\text{Al}_5\text{Cu}_{25}\text{Zr}_{70}$ composition regions, as shown in [Figure 3.6](#). According to the diagram, the “X” alloy is located in the two-liquid-phase region, and the compositions of the two calculated liquid phase are Ni-rich $\text{Zr}_{68.4}\text{Ni}_{23.9}\text{Cu}_{6.6}\text{Al}_{1.1}$ and Cu-rich $\text{Zr}_{61.7}\text{Ni}_{12.8}\text{Cu}_{18.8}\text{Al}_{6.7}$, respectively.

For experimental procedures, the alloy with the optimum composition of $\text{Zr}_{63.8}\text{Ni}_{16.2}\text{Cu}_{15}\text{Al}_5$ is prepared by arc melting of the high purity elements under a purified argon atmosphere, followed by in situ suction casting of the alloy into a copper mold to process BMG rods (2 mm in diameter).

3-2-3 Preparation for $\text{Au}_{49}\text{Ag}_{5.5}\text{Pd}_{2.3}\text{Cu}_{26.9}\text{Si}_{16.3}$

According to the results, reported by Schroers et al. [\[18\]](#), one known that the $\text{Au}_{49}\text{Ag}_{5.5}\text{Pd}_{2.3}\text{Cu}_{26.9}\text{Si}_{16.3}$ amorphous alloys show the best glass forming ability and excellent mechanical properties. Thus, in this study, we choose this composition to investigate the properties of micrometer-sized BMGs at room and elevated temperatures. For the $\text{Au}_{49}\text{Ag}_{5.5}\text{Pd}_{2.3}\text{Cu}_{26.9}\text{Si}_{16.3}$ alloy, the preparation procedure is similar to the fabrication of the $\text{Zr}_{63.8}\text{Ni}_{16.2}\text{Cu}_{15}\text{Al}_5$ alloy. Firstly, the alloys with the compositions of $\text{Au}_{49}\text{Ag}_{5.5}\text{Pd}_{2.3}\text{Cu}_{26.9}\text{Si}_{16.3}$ are fabricated by arc melting preparing the ingots (99.99% for Au, 99.99% for Ag, 99.99% for Pd, 99.99% for Cu, and 99.99% for Si) in an arc furnace under an argon atmosphere. To obtain the homogeneous mixing of composition, the arc melting method should be repeated for more than four times. After the ingots are melted homogeneously by arc melting, the melt is immediately sucked into a water-cooled copper mold with an internal cylindrical-shaped cavity of 3 mm in diameter.

3-3 Property measurements and analyses

3-3-1 XRD and SEM/EDS characterization of as-cast ingots

The glassy nature of the cross-sectional surface of the as-cast rods can be first ascertained by X-ray diffraction (XRD). The SIEMENS D5000 X-ray Diffractometer with Cu K_{α} radiation ($\lambda = 1.5406 \text{ \AA}$) at 40 kV and 30 mA, equipped with 0.02 mm graphite monochromator, is used. Scans are taken over a 2θ range of 20° to 80° using a scanning rate of 0.1° per four seconds. Note that the samples cut from the as-cast rods need to be ground by silicon carbide abrasive papers to remove the possible oxidized outer surface.

Furthermore, the scanning electron microscopy (SEM) equipped with energy dispersive X-ray spectrometry (EDS) is used for the qualitative and quantitative constituent analysis in this study. The sliced samples from the bulk metallic glass rods are selected to identify the constituent component and confirm the composition percentage of the bulk metallic glasses.

3-3-2 Thermal analysis using DSC

Thermal properties of the amorphous alloy rods are characterized by using PerkinElmer Pyris Diamond Differential Scanning Calorimetry (DSC) with a heating rate of 40 K/min under a flowing argon atmosphere. In DSC analysis, it can examine the thermal stability and determine the values of the glass transition temperature (T_g), the crystallization temperature (T_x), the solidus (T_m) and liquidus (T_l) temperatures, and the supercooled liquid region ($\Delta T_x = T_x - T_g$) by the heating process. According to the DSC results, the glass forming ability (GFA) parameters can also be obtained. Furthermore, in order to prevent oxidation and vaporization at high temperatures, samples are placed in copper crucibles and tightly sealed with a nickel

ring. The pre-presence air in the chamber is flushed by pure nitrogen gas and the positive nitrogen pressure is maintained while heating.

3-3-3 Microstructure analysis using TEM

The detailed microstructure of $\text{Mg}_{65}\text{Cu}_{25}\text{Gd}_{10}$, $\text{Zr}_{63.8}\text{Ni}_{16.2}\text{Cu}_{15}\text{Al}_5$ and $\text{Au}_{49}\text{Ag}_{5.5}\text{Pd}_{2.3}\text{Cu}_{26.9}\text{Si}_{16.3}$ amorphous alloys are examined by using the JOEL 3010 analytical scanning transmission electron microscope (AEM) at 200 or 300 kV. The TEM samples are first ground with SiC paper from #1200 to #4000. Then, the TEM samples are thinned by using an ion miller (GATAN PIPS-691 Ion-Miller) to produce the high quality TEM samples. In this step, in order to avoid the radiation induced crystallization or heating, the ion-beam energy is about 3 kV and milling angle about 9° , as reported by Sun et al. [153].

3-4 Microcompression test

3-4-1 Microcompression sample fabrication using FIB

The $\text{Mg}_{65}\text{Cu}_{25}\text{Gd}_{10}$, $\text{Zr}_{63.8}\text{Ni}_{16.2}\text{Cu}_{15}\text{Al}_5$ and $\text{Au}_{49}\text{Ag}_{5.5}\text{Pd}_{2.3}\text{Cu}_{26.9}\text{Si}_{16.3}$ alloy rods are sliced to a disk of 1.5 mm in height by using a diamond cutter. Then the disks are ground with the SiC paper from #1200 to #4000. The surface of these disks is polished to a mirror finish with a diamond polishing paste, from 1 μm grit to 0.25 μm , prior to the focus ion beam (FIB) machining.

The microcompression samples are prepared using the dual focus ion beam system (FIB) of Seiko, SMI3050 SE, following the method developed by Uchic et al. [29]. A Ga beam operated at 30 keV and 7-12 nA is initially directed perpendicular to the surface of the BMG

disk to mill a crater with a much bigger size (around five times of the corresponding pillar) island located in the center. The bigger crater is necessary to leave sufficient space for the flat punch tip in the microcompression tests. Then, the same voltage and smaller currents of 0.7 to 0.09 nA are used to refine the preserved island in the center to a desired diameter and height of the pillar. A series of concentric-circle patterns are utilized to machine the pillars. The diameter, d , of a pillar, e.g., 3.8, 1 and 0.7 μm in this study, is defined as the diameter at the half-height position.

3-4-2 Microcompression test using nanoindentation system

Once the microcompression samples are fabricated, the samples are tested in uniaxial compression by using a commercially available nanoindentation system (MTS Nanoindenter XP), as shown in [Figure 3.7](#). Nanoindentation systems are nominally designed for performing low-load depth-sensing indentation experiments using a sharp diamond tip. One modification is made for this system in order to perform the microcompression tests, which is to replace the sharp tip with a flat punch indenter tip, as shown in [Figure 3.8](#). In this study, the flat punch tip is custom machined out of a standard Berkovich indenter by etching off the diamond tip in the FIB, resulting in the projected area of the flat punch tip is an equilateral triangle of 13.5 μm , as shown in [Figure 3.9](#). The microcompression setup is schematically shown in [Figure 3.10](#). All pillars are deformed in a displacement control under the continuous stiffness measurement (CSM) mode at room temperature. The corresponding strain rates vary from 1×10^{-4} to $1 \times 10^{-2} \text{ s}^{-1}$.

3-4-3 Morphology of deformed pillar samples

The outer surfaces of the pillar samples before and after microcompression are examined

by scanning electron microscope (SEM, JEOL ISM-6330 TF). The shear band distribution on the outer surface of the pillars will be observed in order to study the deformation mechanism for bulk metallic glasses.

3-4-4 Microstructures of deformed pillar samples

In order to observe the detailed microstructure of pillar samples before and after deformation, the TEM samples of the pillars are prepared in the dual focus ion beam of Seiko, SMI3050 SE, using a trenching and liftout technique [154-156]. This schematic illustration of this technique is shown in Figure 3.11 [156]. First, in order to provide a support and to protect the pillar, the carbon is deposited around the pillar using electron beam induced deposition followed by ion beam induced deposition. Then, the slope-etching is employed to cut trenches around the pillar with an energetic Ga ion beam. Next, the TEM samples could be further thinned by using the Ga ion beam with lower voltages and currents. Finally, the TEM samples are moved on a carbon-coated Cu grid. After the TEM sample preparation, the TEM samples are also examined by using the JOEL 3010 analytical scanning transmission electron microscope (AEM) operated at 200 or 300 kV.

3-5 High temperature microcompression test

In the same way, the $\text{Au}_{49}\text{Ag}_{5.5}\text{Pd}_{2.3}\text{Cu}_{26.9}\text{Si}_{16.3}$ amorphous alloy pillar samples with a diameter of 3.8 and 1 μm are fabricated by using FIB to investigate deformation mechanism over a wide range of test temperatures. For high temperature microcompression testing, two kinds of indentation system, MTS Nanoindenter XP and Hysitron Triboindenter, are included in this study. The detailed experimental procedures are described in the corresponding section below.

3-5-1 MTS Nanoindenter XP system

By combining the capabilities of the MTS Nanoindenter system with the heating stage option, this system can be used for mechanical characterization of materials at elevated temperatures. Thus, if the sharp tip is replaced with a flat punch tip, microcompression tests can be performed at elevated temperatures. The appearance of the heating stage is shown in [Figure 3.12](#). The temperature controller is used to control the temperature of the heating stage. This temperature reading is taken from the heater block of the hot stage. There is approximately a 10-11% drop in temperature from the heater block to the sample after the system has reached its steady state. For example, we set 150 °C in the heating controller, but the real temperature measured on sample is only about 135 °C. However, for the convenience of discussion, these real temperatures will be used in the following section. The heating time is 7-8 min from the ambient to elevated temperature, and the time for stabilizing temperature fluctuation is 5-7 min. The temperature fluctuation could be controlled within the variation of < 1 °C during microcompression testing. When testing samples at elevated temperatures, it is crucial to test fast. Due to the temperature difference between the sample and the surrounding environment, the sample will experience thermal expansion and contraction. Therefore, we should conduct loading, unloading, and holding segments in a very short manner. For this reason, for high temperature microcompression testing, all pillar samples are deformed in a displacement control mode with an initial strain rate of $1 \times 10^{-2} \text{ s}^{-1}$.

3-5-2 Hysitron Triboindenter system

High temperature microcompression tests are also performed with a Hysitron Triboindenter system under the displacement control mode using a flat punch which is

machined out of a standard Berkovich indenter with MACOR holder. The projected area of the tip of the punch is an equilateral triangle of 12 μm . The appearances of the heating stage and Hysitron Triboindenter system are shown in Figures 3.13 and 3.14, respectively. To measure the temperature as precisely as possible, test samples attached with a thermal couple are glued on a thin atomic force microscope (AFM) specimen disc using a high temperature glue, and the disc assembly is further clamped onto the heating stage. Meanwhile, the heating stage is covered with a sheet of alumina-silica paper to minimize the convection as shown in Figure 3.15. After stabilizing at a prescribed temperature for at least 15 min, the indenter tip is moved onto the sample surface in the AFM imaging mode, so that the tip could also be heated and reached a steady-state temperature distribution. A temperature variation of < 0.1 $^{\circ}\text{C}$ within 15 min is achieved and the thermal drift rate is also monitored before every experiment. Instead of using an optical microscope, the position of the test pillar is precisely located by AFM imaging in Hysitron Triboindenter using the same flat punch tip at high temperatures. A low set point force of 2 μN and slow scan frequency of 0.4 Hz are used during the AFM image. Once the test is ready, the flat punch began to compress without losing contact with the sample surface. This continuous contact between sample and punch results in a negligible temperature variation (< 0.1 $^{\circ}\text{C}$) and low thermal drift rate (< 1 nm/s) [157]. Constant displacement rate and displacement rate change tests are both performed at the nominal strain rates ranging from 10^{-3} to 10^{-2} s^{-1} . Each compression test took less than 100 s for an acceptable error from thermal drift ($< 10\%$ for 1 μm total displacement).

3-6 Nanoindentation measurements

3-6-1 Elastic modulus and hardness

The nano-mechanical properties of the Mg-, Zr- and Au-based BMGs are tested by the

MTS Nanoindenter XP equipped with a Berkovich indenter under the continuous stiffness measurement mode. The continuous stiffness measurement mode offers a direct measure of dynamic contact stiffness during the loading part of the indentation testing. That is to say, this technique allows the continuous measurement of mechanical properties of materials at any point along the loading curve. In this study, the tested samples are indented to a depth of 1000 nm at a strain rate of $5 \times 10^{-2} \text{ s}^{-1}$. Prior to nanoindentation measurements, the surface of these disks is ground with the SiC paper and then polished to a mirror finish with a diamond polishing paste.

3-6-2 Abrasive wear

All three BMGs are also subject to nanoscratch testing using the MTS Nanoindenter XP equipped with the Berkovich indenter. A typical nanoscratch experiments are performed in three stages; an original profile, a scratch segment and a residual profile. In the first stage, the surface morphology is obtained by pre-profiling the surface under a very small load (100 μN) at a location where the scratch is to be performed. Then, the indenter tip is slid onto the sample surface under ramping loads and the scratch depth is continuously monitored during the scratch testing. Finally, in the same way, a final profile helps establish the residual scratch depth. The schematic of typical nanoscratch experiment is illustrated in [Figure 3.16](#). The tip is slid onto the tested samples at a scratch velocity of 10 $\mu\text{m/s}$ over a length of 500 μm under ramping loads from 0 to 30 mN. The detailed testing condition is shown in [Table 3.2](#). After the nanoscratch testing, the worn scratch tracks are characterized by scanning electron microscopy (SEM, JEOL-6330), and the cross-section profiles are measured by the MTS nanoindentation system. In addition, the residual scratch depth, width and pile-up height can be determined by profiling across the scratch, as shown in [Figure 3.17](#).

Chapter 4 Experimental Results

4-1 XRD and SEM/EDS analysis

The glassy nature of the as-cast $\text{Mg}_{65}\text{Cu}_{25}\text{Gd}_{10}$, $\text{Zr}_{63.8}\text{Ni}_{16.2}\text{Cu}_{15}\text{Al}_5$ and $\text{Au}_{49}\text{Ag}_{5.5}\text{Pd}_{2.3}\text{Cu}_{26.9}\text{Si}_{16.3}$ alloy rods are identified by XRD, as shown in [Figures 4.1\(a\) to \(c\)](#), where no apparent crystalline peak can be detected. In [Figure 4.1\(a\)](#), the XRD pattern of the injection cast Mg-based BMG rod shows a broad peak ranging from 30° to 40° , implying the rod is amorphous. Similarly, the XRD pattern of the suction cast Zr- and Au-BMG rods are shown in [Figures 4.1\(b\) and \(c\)](#), respectively. The broad diffused amorphous humps are also observed in the suction cast Zr- and Au-BMG rods.

Furthermore, the qualitative and quantitative constituent analysis of the as-cast Mg-, Zr- and Au-based BMG rods is identified by SEM/EDS. The results are summarized in [Table 4.1](#). On the basis of EDS results, the composition of the Mg-, Zr- and Au-based BMG rods are close to the designed compositions.

4-2 DSC analysis

To understand the thermal properties of the as-cast $\text{Mg}_{65}\text{Cu}_{25}\text{Gd}_{10}$, $\text{Zr}_{63.8}\text{Ni}_{16.2}\text{Cu}_{15}\text{Al}_5$ and $\text{Au}_{49}\text{Ag}_{5.5}\text{Pd}_{2.3}\text{Cu}_{26.9}\text{Si}_{16.3}$ alloys, differential scanning calorimetry (DSC) is applied. [Figure 4.2](#) shows the typical DSC traces of these three as-cast alloys, scanned at a heating rate of 40 K/min (0.66 K/s). All alloys show a distinct transition onset at T_g , sharp crystallization onset at T_x and large supercooled liquid region, $\Delta T_x = T_g - T_x$, further confirming the amorphous structure of the alloys. The value of T_g , T_x , the solidus temperature

(T_m) and the liquidus temperature (T_l) of the as-cast Mg-, Zr- and Au-based BMGs are listed in [Table 4.2](#) and marked by arrows in the DSC traces.

In addition, according to the DSC results, the reduced glass transition temperature T_{rg} ($= T_g / T_l$), which is a critical parameter in determining the glass forming ability (GFA) of an alloy, is 0.570, 0.549 and 0.619 for the as-cast Mg-, Zr- and Au-based BMGs, respectively. Other GFA parameters such as $\gamma = T_x / (T_g + T_l)$ and $\gamma_m = (2T_x - T_g) / T_l$ are 0.423 and 0.757 for the Mg-based BMG, respectively. The γ and γ_m values for the Zr-based BMG are 0.408 and 0.716; and for the Au-based BMG are 0.430 and 0.774. All of these results suggest that the Mg-, Zr- and Au-based BMGs have good glass forming ability, and these results are also summarized in [Table 4.2](#).

Among the three different BMGs, the Au-based BMG shows a higher glass forming index ($\gamma = 0.430$ and $\gamma_m = 0.774$) and better amorphous thermal property. It is indicated that the composition of $\text{Au}_{49}\text{Ag}_{5.5}\text{Pd}_{2.3}\text{Cu}_{26.9}\text{Si}_{16.3}$ appears to be the optimum composition for glass forming ability or superplastic formability.

4-3 TEM analysis

TEM micrographs are taken to understand the local structure of the as-cast $\text{Mg}_{65}\text{Cu}_{25}\text{Gd}_{10}$, $\text{Zr}_{63.8}\text{Ni}_{16.2}\text{Cu}_{15}\text{Al}_5$ and $\text{Au}_{49}\text{Ag}_{5.5}\text{Pd}_{2.3}\text{Cu}_{26.9}\text{Si}_{16.3}$ amorphous alloys. A bright field image of the Mg-based BMG is shown in [Figure 4.3](#). The selected area diffraction pattern taken from the same region exhibits a halo pattern, as inserted in [Figure 4.3](#). It is well known that the diffuse halo is characteristic of an amorphous material. Thus, according to this TEM result, the Mg-based BMG reveals the fully amorphous structure and no visible nanocrystals.

For the Zr-based BMG, the two different regions can be observed by TEM. One is phase separation region, as shown in [Figure 4.4\(a\)](#); the other is glassy matrix region, as shown in [Figure 4.4\(b\)](#). Their corresponding diffraction patterns are inserted in [Figures 4.4\(a\)](#) and [\(b\)](#), respectively. The microstructure of the phase separation region is further characterized by TEM, as shown in [Figure 4.5](#). From this diagram, the phase separation is visible in some regions, one with dark contrast and the other with bright contrast. The selected area diffraction pattern taken from the dark and bright domains shows the diffuse halo nature, as inserted in [Figure 4.5\(b\)](#). [Figure 4.5\(c\)](#) displays the high resolution electron-microscopy (HREM) image taken from the interface of the two glassy phases denoted by dotted circle in [Figure 4.5\(b\)](#). This result further indicates that the two glassy phases combine perfectly due to no sharp lattice-fringe boundary.

From the TEM observations, all of these results suggest that the Zr-based BMG exhibits two-glassy-phase separation. However, it is worth noting that the phase separation seems to happen only in partial regions, not everywhere. There are still some glassy matrix shows no phase separation exhibiting a single bright contrast and diffuse halo pattern, as shown in [Figure 4.4\(b\)](#). Furthermore, based on the computational-thermodynamics approach, these separated liquid phases can be frozen successfully into the separated glassy phases by using the copper mold suction casting with the rapid cooling rate.

For the Au-based BMG, the bright field image and selected area diffraction pattern are shown in [Figure 4.6](#). The TEM evidence demonstrates the Au-based BMG is an amorphous structure and no obvious crystalline structure, in reasonable agreement with the previous XRD results.

4-4 Microcompression test

The appearances of FIB machined pillars before microcompression test are shown in [Figure 4.7](#) and [Figure 4.8](#) for the Mg- and Zr-based BMGs, respectively. The microcompression pillar samples have an approximate aspect ratio (height/diameter) of 2-3, following the recommendation provided by finite element modeling [136]. Due to the convergence angle of the ion beam, these pillars are slightly tapered, and the taper angle from the top to the bottom is $\sim 2.5^\circ$.

4-4-1 Results for $\text{Mg}_{65}\text{Cu}_{25}\text{Gd}_{10}$

Two kinds of pillars with diameters of 3.8 and 1 μm are prepared by using the FIB milling, and the microscale mechanical properties of the Mg-based BMG are conducted with microcompression test at strain rates ranging from 1×10^{-4} to $1 \times 10^{-2} \text{ s}^{-1}$. The load-displacement curves are shown in [Figure 4.9](#). It should be pointed out that the load-displacement data can readily convert into the stress-strain curve under the assumption that the sample is uniformly deformed. However, in this study, the Mg-BMG pillar samples are inhomogeneously deformed by localized shear bands. Thus, we choose to show the load-displacement curves for the discussion.

According to [Figure 4.9](#), yield strength is determined from the departure of the linearity of the early portion of the load-displacement curve. Since the sample is tapered, yielding will start from the top of the sample which is the location with the minimum cross section. Then, the yield strength can be obtained from the departure load divided by the top area. These data are summarized in [Table 4.3](#).

The yield strengths of the 3.8 and 1 μm Mg-based BMG pillars range from 1342 to 1580 MPa, which are much higher than that of the bulk $\text{Mg}_{65}\text{Cu}_{25}\text{Gd}_{10}$ samples, which is about 800 MPa [158]. The result of improved strength caused by a decrease in sample size is consistent with a previous study on millimeter-scaled BMG [34]. Also noted in Table 4.3 is the fact that the average strength of the 1 μm pillar (~ 1490 MPa) is higher than that of the 3.8 μm pillar (~ 1363 MPa). This demonstrates that the sample size effect can extend from the millimeter to micrometer range. The improved strength is a natural consequence of decreasing defect population which reduces the probability of shear band initiation in smaller samples. The improvement of strength from millimeter-scaled sample to micrometer-scaled pillar is increased about 60~100%, which is quite remarkable. However, this increment of strength in metallic glass alloys is still not as remarkable as that in polycrystalline metals. For example, a 1 μm -diameter Ni_3Al sample exhibits yield strength of 1750 MPa, whereas a bulk Ni_3Al sample yields at about 200 MPa [29]. Similar trend can be found in gold samples as well [137]. This remarkable sample size effect in polycrystalline metals is a result of dislocation starvation in the micro-sized sample.

As shown in Figure 4.9, after yielding, the load remains essentially constant at different strain rates. The corresponding engineering stress-strain curves have a similar shape, as shown in Figure 4.10. This particular shape of stress-strain curve usually, according to the conventional wisdom, leads to a conclusion that bulk metallic glass behaves like a perfectly plastic material. However, the raw displacement-time data, as given in Figure 4.11, seem to reveal a different message. Specifically, data in Figure 4.11 indicate the displacement (or strain) takes place almost instantly. In other words, strain does not occur in a gradual fashion but in the form of burst, even though the tests are conducted under strain rate control conditions. The every strain burst event, regardless of the strain rate, proceeds within about one second, suggesting the strain rate during these bursts was at least 10^{-1} s^{-1} . Thus, this

phenomenon is called “strain burst”. There is also a notable trend that, for both pillar samples, a faster compression rate results in a larger strain burst. The instant strain burst is peculiar but is usually indicative of a sudden propagation of a localized shear band.

From the morphology of deformed pillar samples considerations, as shown in [Figure 4.12](#), it is worthy to note that these pillars did not appear the catastrophic fracture after straining. Generally, bulk Mg-based BMGs often fracture into pieces immediately upon the stress approaching the yield point. Since the Mg-based BMGs possess a low Poisson’s ratio ~ 0.32 , the sample would easily dilate near the crack tip, resulting in the brittle properties [\[159\]](#). However, for pillar deforming body, the pillars usually exhibit the plastic strain of 10~15% without fracture because the shear offset achievable in even one single shear band may already result in large strains before failure.

According to the SEM observation, shear band is anticipated to initiate from the corner of contact between sample and compression punch. This is where the sample experiences the maximum stress, not only because it is the minimum cross section as a result of sample taper, but also due to the large constraint caused by the friction between the test sample and punch tip. Indeed, it is clearly shown in [Figure 4.12](#), in which all pillars are observed to deform by the shear mode after yielding. Furthermore, it is also noted that there are very limited numbers of shear bands in these micropillar samples, especially in the 1 μm pillar sample. In fact, at the slowest strain rate of $1 \times 10^{-4} \text{ s}^{-1}$, only one shear band is present. This can be presumed that 1 μm is close to the scale limit of shear band spacing.

4-4-2 Results for $\text{Zr}_{63.8}\text{Ni}_{16.2}\text{Cu}_{15}\text{Al}_5$

In the above-mentioned study on the brittle Mg-based BMG micropillars, they exhibit

very few shear bands. Especially in the 1 μm pillar sample, only one single shear band is present at a low strain rate. However, for the much more ductile phase-separated Zr-based BMG micropillars, there are more than one single shear bands in the 1 μm pillar sample. Thus, the smaller pillar samples (700 nm) need to be investigated further the shear banding behavior of much more ductile phase-separated Zr-based BMG pillar samples.

In this study, three kinds of pillars with diameters of 3.8 μm , 1 μm and 700 nm are prepared by using the FIB milling, and the microscale mechanical properties of the Zr-based BMG are conducted with microcompression test at strain rates ranging from 1×10^{-4} to $1 \times 10^{-2} \text{ s}^{-1}$. Besides, in order to exhibit sample size effect, we choose to show the engineering stress-strain curve for the discussion, as shown in [Figure 4.13](#).

Despite the fact that the Zr-based BMG micropillars are also inhomogeneously deformed by localized shear bands, it is evident that the strength of these micropillars is a function of sample size. If we take the first strain burst as the onset of plasticity and assign it as the yield strength of the micropillar, the trend of increasing strength with decreasing sample size becomes apparent. For example, at the intermediate strain rate of $1 \times 10^{-4} \text{ s}^{-1}$, the yield strengths of the 3.8 , 1 , and 0.7 μm pillars are 2088, 2496, and 2972 MPa, respectively. These values are all higher than the 1600 ± 50 MPa for the 2 mm $\text{Zr}_{63.8}\text{Ni}_{16.2}\text{Cu}_{15}\text{Al}_5$ bulk compression samples [\[151\]](#). These data are listed in [Table 4.4](#). The highest yield strength recorded for the Zr-based micropillar is about 3000 MPa, which is more than 1.8 times of the bulk form.

It is worthy to note that strain bursts in the ductile Zr-based BMG micropillars are multiple and appear to proceed in a progressive fashion, in contrast to that in the brittle Mg-based BMG micropillars which usually exhibit only single strain burst. The increment of

the load or the transformed engineering stress in each step varies from 100 to 500 MPa, which cannot be negligible. It seems to be a blocking resistance for the propagating shear band, and to induce the initiation of the next shear band operative at a higher load or stress.

The morphologies of representative micropillars after the compression are shown in [Figures 4.14-4.16](#). The deformation mode of these micropillars is invariably the localized shear banding, independent of the sample size. The first shear band is initiated from the corner of the contact surface between the sample and compression indenter punch, where the sample has the least cross-sectional area and thus experiences the maximum stress. With increasing straining, more shear bands are triggered continually. From [Figures 4.14-4.16](#), we can observe that sample shear-off does not occur immediately. This phenomenon is also reflected in the engineering stress-strain curves presented in [Figures 4.13](#).

A close examination of [Figures 4.14-4.16](#) shows that the number of shear bands in the ductile Zr-based BMG micropillars (mostly 3 to 6) is much higher than that previously observed in the brittle Mg-based BMG micropillars (mostly 1 to 3). There appears to be a one-to-one correspondence between the number of shear bands ([Figures 4.14-4.16](#)) and the number of stress jumps ([Figure 4.13](#)), suggesting each stress jump is a result of the emission of a new shear band. Note also that the number of shear bands ([Figures 4.14-4.16](#)), as well as the number of strain bursts ([Figure 4.13](#)), appears to reduce with decreasing pillar size and decreasing strain rate. In fact, for the smallest 700 nm Zr-based BMG pillars deformed at the strain rate of $1 \times 10^{-4} \text{ s}^{-1}$, there is only one displacement burst, resembling the observation in a brittle Mg-based BMG micropillar.

4-4-3 TEM analysis of the microstructure in pillar sample

In order to be able to observe the microstructure of micropillar, the TEM samples need to be fabricated by FIB with a trenching and liftout technique [154-156]. The TEM sample preparation procedure is shown in Figure 4.17. Figure 4.17(a) shows the 1 μm pillar sample of the Zr-based BMG before microcompression test. First, in order to provide a support and to protect the pillar sample, carbon is deposited around the pillar using electron beam induced deposition followed by ion beam induced deposition, as shown in Figure 4.17(b). Next, in Figure 4.17(c), an energetic Ga ion beam is used to cut the trenches on the sample surface. Then, the TEM sample can be further thinned by using the Ga ion beam with lower voltage and current, as shown in Figure 4.17(d).

The bright field TEM image of a lamella prepared from the undeformed micropillar is shown in Figure 4.18(a). The selected area diffraction pattern and the high resolution electron-microscopy image are also shown in Figures 4.18(b) and (c). In this study, no crystalline structure is visible in the TEM image, and the corresponding diffraction pattern always show a typical halo for an amorphous structure, in good agreement with the XRD results. The HREM image also displays that alloy is an amorphous structure and no obvious crystalline structure.

On the other hand, the TEM sample of the deformed pillar can also be prepared by FIB. The results of the deformed 1 μm Zr-based BMG pillar are shown in Figure 4.19. Figure 4.19(a) demonstrates the appearance of 1 μm Zr-based BMG pillar after the compression. The bright field TEM image, diffraction pattern and HREM image of the deformed pillar are shown in Figures 4.19(b)-(d), respectively. From the TEM observations, the deformed Zr-based BMG pillar is also an amorphous structure and crystallization is never induced even after deformation.

Besides, according to [Figure 4.19\(b\)](#), it is particularly noted that the shear fracture angle between the shear band plan and loading axis of the pillar sample is about 42° in the current study. This angle is similar to that reported in the literature for compression of a various BMG systems [[82](#), [160-162](#)]. The results suggest that the fracture behavior is very similar in the BMG bulk and pillar samples.

For Mg-based BMG, a bright field TEM image and diffraction pattern of the deformed pillar are shown in [Figure 4.20\(b\)](#) and [\(c\)](#), respectively. For clarity, the SEM image of the deformed Mg-based BMG pillar is shown in [Figure 4.20\(a\)](#). According to TEM observations, the deformed Mg-based BMG pillar is an amorphous structure and no obvious crystalline structure. In addition, the shear fracture angle of the deformed Mg-based BMG pillar is close to 43° , as demonstrated in [Figure 4.20\(b\)](#). All results are similar to those observed in the deformed Zr-based BMG pillar.

4-5 High temperature microcompression test

Two kinds of pillars of the Au-based BMG with diameters of 3.8 and 1 μm are prepared by using the FIB milling. The morphologies of typical pillar samples before high temperature microcompression test are shown in [Figure 4.21](#). The aspect ratio of Au-based BMG pillar sample is about 2-3; the taper angle from the top to the bottom is about 2.5° . The Au-based BMG is chosen as model material because of its low glass transition temperature and excellent resistance to oxidation at high temperatures. In addition, two kinds of indentation system, MTS Nanoindenter XP and Hysitron Triboindenter, are used to analyze the mechanical behavior of the Au-based BMG pillar samples.

4-5-1 Results for $\text{Au}_{49}\text{Ag}_{5.5}\text{Pd}_{2.3}\text{Cu}_{26.9}\text{Si}_{16.3}$ using MTS Nanoindenter

To measure the relationship between sample size, temperature and strain rate for micron-sized amorphous alloys, high temperature microcompression tests are conducted by means of MTS nanoindenter XP system equipped with a heating stage. In this section, the 1 μm Au-based BMG pillar samples are tested at different temperatures (room temperature, 343, 373, 383, 393, 403 and 408 K) with a nominal strain rate of $1 \times 10^{-2} \text{ s}^{-1}$. Note the glass transition temperature of this BMG is about 400 K.

The load-displacement and time-displacement curves for these tests at different temperatures are shown in [Figure 4.22](#) and [Figure 4.23](#). The engineering stress-strain curves, converted from the load-displacement data under the assumption of homogeneous-deformation, are also plotted in [Figure 4.24](#). [Table 4.4](#) summarizes the entire measured flow stress and deformation mode of the 1 μm Au-based BMG pillar samples at different temperatures.

It is noted that, from room temperature to 393 K, the deformation behavior of the 1 μm Au-based BMG pillar samples is manifested as the strain burst, as shown in [Figure 4.22](#) and [4.23](#). The strain burst phenomenon is believed to be caused by a localized shear band emission, which is further confirmed by the SEM image in [Figure 4.25](#). From the photographs of the deformed samples, the pillar samples revealed the major shear bands in upper region of the pillars, as shown in [Figure 4.25](#). That is to say, from room temperature to 393 K, the localized shear banding is the dominant deformation mode.

However, the deformation behavior of the Au-based BMG pillar samples at 403 and 408 K is a continuous and steady flow stress in contrast to those strain burst events, indicating that a change of the dominant deformation mode. The morphologies of the Au-based BMG

pillar samples after the compression at 403 and 408 K are shown in [Figure 4.26](#). It is evident in the figure that they are compressed evenly, exhibiting the homogeneous deformation. In addition, the flow stress of the pillar samples compressed at 403 and 408 K significantly reduces to 0.5-0.6 GPa as compared with compression at room temperature, as shown [Figure 4.24](#) and [Table 4.5](#).

4-4-2 Results for $\text{Au}_{49}\text{Ag}_{5.5}\text{Pd}_{2.3}\text{Cu}_{26.9}\text{Si}_{16.3}$ using Hysitron Triboindenter

According to the aforementioned results, one can know that the inhomogeneous-to-homogeneous transition of the Au-based BMG will take place near the glass transition temperature ($T_g \sim 400$ K). In the following section, in order to analyze further the homogeneous deformation behavior, high temperature microcompression tests are performed on the 3.8 μm Au-based BMG pillar samples with a Hysitron Triboindenter system.

Microcompression tests are performed on four pillar samples at two temperatures and different strain rates, as listed in [Table 4.6](#). The load-displacement curves for constant strain rate and strain rate change tests are plotted in [Figure 4.27 \(a\)](#) and [\(b\)](#), respectively. The SEM images of a typical Au based BMG pillar sample before and after high temperature microcompression test are shown in [Figure 4.28](#). The deformation is homogeneous without any localized shear bands as shown in [Figure 4.28](#). The top surface of the compressed pillar is smooth, which means the flat punch is in good shape and the AFM mode located the pillar sample very well.

For easy discussion of mechanical analysis, the compressive displacement (ΔL) recorded from load-displacement curves, as well as the time duration (t) and measured drift rate are all

listed in Table 4.7. The sample heights before (H_1) and after (H_2) each test are also measured from scanning electron microscopy (SEM) images and listed in Table 4.7 for a direct comparison. It is noted in the table that $\Delta H (=H_1-H_2)$ is close to ΔL in all pillar samples, indicating that the strain contribution from the base of the pillar is insignificant. This is in contrast to the deformation of a pillar at room temperature which often shows significant strain contribution from the pillar base [163]. The difference is caused by the fact that metallic glasses have a high strain rate sensitivity value (m) at temperatures near the supercooled region. Thus, the pillar sample is preferentially deformed. It is also noted in Table 4.7 that the difference in the length change measured from SEM image and load-displacement curve [i.e., $(\Delta H-\Delta L)$] is comparable to the displacement error cause by thermal drift. This suggests that the strain measurement obtained directly from Hysitron Triboindenter is reliable.

Since the pillar sample is homogeneously deformed, the load-displacement data are readily converted into true stress-strain curves in Figure 4.29. As shown in the figure, the strength of the pillars is noted to increase with strain rate and decrease with temperature, and it is consistent with the results previously reported for high temperature nanoindentation on the same alloy [127]. However, in contrast to the stress overshoot often observed in millimeter-size metallic glass samples deformed in the supercooled liquid region at high strain rates [103-107], stress overshoot is absent in the compression of the current microscale Au-based BMG pillars. The absence of stress overshoot may be associated with the fact that strain rate is too low, thus free volume annihilation occurs too fast, or the response of the indenter is too slow to capture the strain rate change. There is also a possibility of the sample size, thus shear band length, effect.

4-6 Nanoindentation and nanoscratch test

4-6-1 Elastic modulus and hardness

The nanoindentation test is now commonly used for the study of mechanical properties of materials on the nanoscale. To assess the nano-mechanical properties of amorphous alloys, we selected the brittle-natured $\text{Mg}_{65}\text{Cu}_{25}\text{Gd}_{10}$, moderate brittle $\text{Au}_{49}\text{Ag}_{5.5}\text{Pd}_{2.3}\text{Cu}_{26.9}\text{Si}_{16.3}$ and ductile phase-separated $\text{Zr}_{63.8}\text{Ni}_{16.2}\text{Cu}_{15}\text{Al}_5$ amorphous alloys. The typical load-depth (P-h) curves of the Mg-, Au- and Zr-based BMGs under a strain rate of $5 \times 10^{-2} \text{ s}^{-1}$ are plotted in [Figure 4.30](#). The load-depth curves at room temperature are characterized by a series of discontinuous pop-in displacement bursts, which are similar to what are observed previously in other BMGs [\[111-117\]](#). It is evident that the Zr-based BMG is harder than the Mg- and Au-based BMG, as revealed by the fact that a higher load is required to indent the Zr-based BMG to the same depth. The measured elastic modulus and hardness of the three different BMGs are listed in [Table 4.8](#). These values are slightly higher than those obtained by the conventional measurement because of the size effect in measurement area [\[164, 165\]](#).

4-6-2 Abrasive wear behavior

It is well known that wear is an important failure mode in various applications. Wear characteristic, such as wear resistance, is often an important second property. Therefore, it is necessary to clarify the wear behavior in BMGs. In this study, the Mg-, Au- and Zr-based BMGs are investigated in detail using nanoscratch testing.

The typical scratch depth profiles of the three different BMGs are shown in [Figure 4.31\(a\)](#). The scratch depths for the Mg-, Au- and Zr-based BMGs are about 367, 316 and 250 nm, respectively. The cross-sectional profiles for the three BMGs are measured by a surface

scan under a very small load (100 μN) at the halfway point of scratch distance, as shown in [Figure 4.31\(b\)](#). Plane-view morphologies of the worn scratch tracks for the Mg-, Au- and Zr-based BMGs are shown in [Figures 4.32 to 4.34](#), respectively. The total volume of material removed during the scratch test can be qualitatively measured by the scratch depth and cross-section profile because of the fixed Berkovich indenter geometry. Then, according to the Archard wear equation [\[166\]](#) and the modified Archard wear equation [\[167, 168\]](#), the wear coefficient K and wear resistance R_w of the three different BMGs can be calculated. The Archard wear equation can be expressed as

$$V_w = K \frac{SN}{H}, \quad (4-1)$$

where V_w is the total volume of material removed by the wear, K is the wear coefficient, S is the total sliding distance, N is the normal load, and H is the material hardness. The wear coefficient K is also one of the wear properties. For the ease of engineering applications, the Archard wear equation can be modified as

$$R_w = \frac{SN}{V_w}, \quad (4-2)$$

where R_w is the wear resistance and it has the unit of Pa. Thus, in the current nanoscratch test, inserting proper value for each variable into [Eq. \(4-1\)](#) and [Eq. \(4-2\)](#), the average wear resistances of the three BMGs are calculated to be 0.97×10^{11} , 2.17×10^{11} and 4.17×10^{11} Pa, respectively, as included in [Table 4.8](#).

Chapter 5 Discussions

5-1 Room temperature microcompression test

As described in the previous section, microcompression tests on the Mg- and Zr-based BMG pillar samples have shown an obvious sample size effect, with the yield strength increasing with decreasing sample diameter. However, some scientists argued or considered that sample size effect may be attributed to several possible reasons [140, 169, 170], such as the effect of pillar taper and instrumental or methodological artifact. Thus, firstly, we need to check the accuracy of the results obtained from the microcompression test. The effects of pillar taper and FIB damage will be discussed in the following section. In addition, the Weibull statistics has been used to support the observation that the compressive stress increases with decreasing sample size. Subsequently, strain burst phenomena and speeds are also discussed in the following section.

5-1-1 Evolution of Young's modulus

According to the literature [136], one can know that Young's modulus, E , is quite sensitive to the sample misalignment. Thus, any measured property that correlates with E is likely to be influenced by misalignment. In our study, one could imagine that misalignment will cause bending that would affect the initiation of the shear band. In order to check the accuracy of the yield strength, it is very important to evaluate the Young's modulus.

In this study, the effect of the pillar taper and the base compliance need to be considered for evaluation of the Young's modulus. First, since the test sample is uniformly tapered pillar,

as illustrated in [Figure 5.1](#), the total measured displacement, Δh , is

$$\Delta h = \frac{1}{h_o} \int_0^{h_o} \Delta u(x) dx, \quad (5-1)$$

where h_o is the height of the pillar, $\Delta u(x)$ is the local displacement. In the elastic range, with $\sigma = E\varepsilon$, $\sigma(x) = P/A(x)$ and $\varepsilon(x) = \Delta h(x)/h_o$, where P and A are instantaneous load and sample cross section area, respectively, the [Eq. \(5-1\)](#) is deduced to

$$\Delta h = \int_0^{h_o} \varepsilon_x dx = \int_0^{h_o} \frac{P}{\pi(d_o + x \sin \theta)^2 E} dx, \quad (5-2)$$

where d_o is the radius of the pillar, and $\theta = 2.5^\circ$ is the taper angle. As $\sin \theta \approx \theta$, the equation leads to

$$\Delta h = \left(\frac{P}{\pi E d_o^2} \right) \left(\frac{d_o}{2\theta} \right) \ln \left(1 + \frac{2\theta h_o}{d_o} \right). \quad (5-3)$$

Therefore,

$$E = \left(\frac{P}{\Delta h} \right) \left(\frac{\ln \left(1 + \frac{2\theta h_o}{d_o} \right)}{\pi d_o 2\theta} \right). \quad (5-4)$$

Substitute $d_o = 0.5 \mu\text{m}$ and $h_o = 2.5 \mu\text{m}$ (for the $1 \mu\text{m}$ pillar sample), one has

$$E = 2.64 \times 10^{12} \left(\frac{P}{\Delta h} \right), \quad (5-5)$$

where P and Δh are in the units of Newton and meter, respectively. Thus, for the $1 \mu\text{m}$ $\text{Mg}_{65}\text{Cu}_{25}\text{Gd}_{10}$ pillars, the elastic modulus is the slope of load-displacement curve multiplied by a constant of 2.64×10^{12} , which is about 41 GPa.

In our study, the effect of the base compliance also needs to be considered in the Mg-BMG. According to a finite element analysis of micro-compression [\[136\]](#), the actual Young's modulus should be corrected by a factor of about 1.25. After correcting, the value of

Young's modulus is 51.3 GPa, which is in excellent agreement with the literature value of 50.6 GPa measured from the bulk Mg-BMG sample [10].

In the same way, the Young's modulus of $Zr_{63.8}Ni_{16.2}Cu_{15}Al_5$ micropillars varies around 78 ± 6 GPa, which is same as the data reported in literature for Zr-Ni-Cu-Al BMGs (~ 80 GPa) [28]. Therefore, the corrected results of the Young's modulus indirectly indicate that the misalignment artifact on the yield strength measurement is minimized in this study.

5-1-2 Effect of FIB damage

The significant increase in the strength of the pillar samples might arise debate on the origins. There have been discussions on the possible causes for the observed stress increment [30, 137]. One of them is the taper shape, and the other is the strengthening artifact caused by the FIB damaged layers. The former cause has been discussed and ruled out in the previous section. Here, we examine the effect of FIB damage, in particular the lateral thickness of the damage layers on the micropillar samples caused by FIB machining.

Bei et al. [169] have examined the hardening of the FIB-milled Mo single crystal caused by using various FIB beam voltage (5-30 kV), current (1.4-7 nA) and time (7.8-39 min). The acceleration voltage determines the depth of Ga ion penetration and the current and time determine the degree of damage in the damage zone. From the results of Bei et al., as long as the beam energy, or voltage times current, is lower than 30 kV•nA, the hardness increment is less than 25%. In the current study, a FIB beam voltage of 30 kV is used, but coupled with a lower beam current, from the initial current 12 nA for rough beam milling for make the outer crater, progressively lowered to 0.7 nA for milling the pillar, and finally to 0.09 nA in the

final trimming step. For the later critical stage, the beam energy is limited within 3 kV•nA, well below the threshold value. Also noted is the fact that FIB used for the later stage trimming of our samples is directed parallel to the pillar side wall. Therefore, the FIB ion dose damage is expected to be even lower than the case of when the beam is bombarded perpendicular to the sample flat surface.

To evaluate the FIB damage, Auger electron spectroscopy (AES, JEOL, JAMP-9500F) is employed for estimating the thickness of the FIB damaged layer in the Zr-based BMG micropillar with a diameter of 3.8 μm. The Auger depth profile is shown in [Figure 5.2](#). Ga signal levels off (the baseline intensity) at a depth of approximately 4 nm, indicating the thickness of FIB damaged layer is about 3-4 nm. This value is much lower than the damage thickness of 10 to 50 nm reported in crystalline Si [\[171, 172\]](#). Based on the current result, the contribution of the damage layer to the strength of a 700 nm-diameter micropillar is estimated to be only 3%, which is considered to be insignificant.

5-1-3 Weibull statistics

It is well known that, for brittle materials, the variability of strength is expected based on their flaw sensitivity and could be analyzed using the Weibull Statistics [\[173\]](#). The Weibull equation describes the fracture probability P_f for a given uniaxial stress σ ,

$$P_f = 1 - \exp \left[-V \left(\frac{\sigma - \sigma_u}{\sigma_o} \right)^m \right], \quad (5-5)$$

where σ_o is a scaling parameter (or characteristic strength), m is the Weibull modulus, and V is the volume of the tested sample. Besides, σ_o is often taken to be approximately the mean strength. The parameter σ_u is the stress below which the probability of failure is zero. If we

assume that any stress will cause failure in a brittle material, then we can take σ_u to be zero.

The Weibull modulus is a measure of the variability of the strength of the material; a higher m value denotes a narrow distribution of fracture stresses and higher reliability. The Weibull modulus can theoretically range from 0 to ∞ . In general, the Weibull moduli for ductile crystalline metals and for brittle engineering ceramic materials are typically on the order of ~ 100 and ~ 5 [174], respectively.

In this study, in order to simplify the Weibull equation, we assume that the millimeter and micron samples have a constant fracture probability. Then, at a fixed fracture probability, i.e., $P_f = \text{constant}$, the above equation could be reduced to

$$V \left(\frac{\sigma}{\sigma_0} \right)^m = \text{constant}. \quad (5-6)$$

Since $V \propto d^3$, where d is the diameter of the compression sample, it can be obtained

$$d^3 \sigma^m = \text{constant}. \quad (5-7)$$

Using data listed in Table 4.3 and 4.4, the relationship between strength and sample size is plotted in Figure 5.3. The Weibull modulus is calculated to be around 35 and 60 for $\text{Mg}_{65}\text{Cu}_{25}\text{Gd}_{10}$ and $\text{Zr}_{63.8}\text{Ni}_{16.2}\text{Cu}_{15}\text{Al}_5$, respectively. It is also within the range of the m values recently reported for the malleable $\text{Zr}_{48}\text{Cu}_{45}\text{Al}_7$ ($m=73.4$) and brittle $(\text{Zr}_{48}\text{Cu}_{45}\text{Al}_7)_{98}\text{Y}_2$ ($m=25.5$) [175] and for $\text{Mg}_{66}\text{Zn}_{30}\text{Ca}_4$ ($m=41$) and $\text{Mg}_{71}\text{Zn}_{25}\text{Ca}_4$ ($m=26$) [176]. Therefore, an increase in strength with decreasing sample size appears to be a result of reducing the population of critical flaw in test samples.

Finally, it is noteworthy that the difference of m -value between the nominally ductile Zr-based BMG and brittle Mg-based BMG. In this study, the m -value of the phase-separated

ductile Zr-based BMG is higher than the brittle Mg-based ones, which is also consistent with the general trend for the Weibull modulus.

5-1-4 Sample size and strain rate effect

Based on [Table 4.3](#) and [4.4](#), it is noted that the Mg- and Zr-based BMGs show a pronounced sample size effect on strength. For Mg-based BMG, the yield strength of the micropillars shows a 60-100% increase as compared to those of their bulk sample; for Zr-based BMG, the yield strength of the micropillars shows a 25-86% increase over that of the bulk samples. It is worthy to mention that the yield strength of the Mg-based BMG pillars almost approaches $G/12$, where G is the shear modulus of 19.3 GPa. The similar trend is also observed in the Zr-based BMG pillars. Although there is no existing theory to predict the theoretical strength of amorphous alloys, it is of interest to note that $G/(10-12)$ is also coincident with the predicted value for polycrystalline metals [[177](#), [178](#)].

Another interesting point is that the different degree of increase of yield strength can be found in the Mg- and Zr-based BMGs. To take a simple example, for 3.8 μm pillar sample, the yield strength of the Mg- and Zr-based BMGs exhibits 73% and 30% increase when compared with bulk counterparts. Presumably, the degree of increase of yield strength is relative to the quality of cast sample. Thus, the BMG sample surface is examined afterward in order to determine the quality of cast sample.

First of all, after polishing, the Mg- and Zr-based BMGs both exhibit a perfect mirror surface. That is, no hole or pore can be observed on the Mg- and Zr-based BMG sample surfaces. However, after FIB milling, the Mg-based BMG sample surface has more holes than the Zr-based BMG, as shown in [Figure 5.4](#). The observed hole diameter of the Mg-based

BMG sample surface is about 1-10 μm . It is believed to result from the different Ga etching rate since Ga etching rate is significantly affected with the different composition distribution or exhibiting narrow pore.

Thus, the different degree of increase of yield strength on BMGs is likely to be responsible for the quality of cast sample. That is to say, different qualities of BMGs may possess a different degree of increase in yield strength. For the $\text{Pd}_{40}\text{Ni}_{40}\text{P}_{20}$ BMG, Schuster et al. [141] demonstrated only 9% increase in the yield strength as the size is reduced from the bulk samples to the 2 μm pillar samples. This might support that their Pd-based BMG has much less cast defects or holes, thus the stress increment of micro-sized pillars would be much smaller.

In addition, it is particularly noted that there are very limited number of shear bands in the 1 μm Mg-based BMG pillar samples, as shown in Figure 4.12. The results indicate that 1 μm is close to a critical spacing of a shear band for the Mg-based BMG. However, there are one or two shear bands observed in the 700 nm Zr-based BMG pillar samples, Figures 4.14-4.16. That is to say, the different shear band spacing might be present in the Mg- and Zr-based BMG pillar samples. The current results suggest that different BMG compositions might have different critical spacings for the formation of shear band.

Furthermore, if the sample size is further decreased, we believe there is another sample size effect on deformation mechanism of BMG, as illustrated in Figure 5.5. When the shear band spacing is greater than the dimension of the test sample, homogeneous deformation would dominate. Thus, the Zr-based BMG pillar samples with diameter ranging from 3.8 μm to 300 nm are fabricated to investigate the transition from the expected shear band to homogeneous deformation, as shown in Figure 5.6. Based on Figure 5.7, the average taper

angle are evaluated to be 6-8° for the 300 nm pillar samples. However, due to the large taper angle, it is difficult to compress the 300 nm Zr-based BMG pillar samples. It is because that a flat punch tip is not good contact with the small pillars, resulting in severe buckling. The evidence of buckling can be observed clearly in [Figure 5.7\(b\)](#) and [\(d\)](#). But, the local melting can be found in the 300 nm deformed pillar, as show in [Figure 5.7\(f\)](#). The results indicate that the pillar sample releases the energy by generation of heat not by emission of shear bands. Thus, for the Zr-based BMG pillar, we infer that the transition from inhomogeneous deformation (i.e. formation of shear band) to homogeneous deformation will take place when the diameter is reduced down to about 300 nm.

For the strain rate effect, this effect on yield strength of the Mg- and Zr-based BMG pillar samples is inconclusive. However, one can see that there is a general tendency of having more shear bands in pillars deformed at a higher strain rate. This is clearly demonstrated in [Figures 4.12](#) and [4.14-4.16](#), although the strain rate differs by only two orders of magnitude in the current study. According to the literature, Gao et al. [\[179\]](#) also reported the similar results, a finer shear band spacing at a faster strain rate.

5-1-5 Strain burst phenomena

In the current study, the deformation of the Mg- and Zr-based BMG micropillars is dominated by emission of shear bands in a manner of “strain burst” to release the energy, similar to that in crystalline solids [\[29\]](#). However, in contrast to that in the case of Mg-based BMG micropillar which exhibits only one single strain burst, strain bursts in the more ductile Zr-based BMG micropillars are multiple and they appear to proceed in a progressive fashion. For clarity, the comparison of the microcompression engineering stress-strain curves for the Mg- and Zr-based bulk compression samples (2 mm), and the 1 μm Mg- and Zr-based pillar

samples are plotted in [Figure 5.8](#).

The SEM observations for the deformed Mg- and Zr-based bulk samples are shown in [Figure 5.9](#). For the Mg-based bulk compression samples, the bulk Mg-based BMGs generally fracture into fragments at the onset of yielding. Nevertheless, for the Zr-based bulk samples, multiple shear bands along various orientations is overwhelming and the engineering stress-strain curve shows extended ductility, which is compared in [Figure 5.8](#). The deformed 1 μm Mg- and Zr-based pillar samples are shown in [Figures 4.12](#) and [4.14](#), respectively.

For pillar samples, based on the SEM observation and compression test results, it is noted that the number of strain bursts (or shear bands) of the Zr-based BMG micropillars is much higher than those observed in the Mg-based BMG micropillars. Since all micropillars have a similar geometry, i.e. similar aspect ratio and taper angle, the increase in the number of strain bursts (or shear bands) is indicative of intrinsic plasticity in the Zr-based BMG. The current finding from the micropillars is consistent with that observed from the bulk samples, namely, the Zr-based BMG is more ductile than the Mg-based BMG.

In addition, additional remarks must be made from the examination of [Figures 4.12](#) and [4.14-4.16](#). First, the recorded displacement (or strain burst) comes from a sudden macroscopic sliding which is triggered by microscopic shear band propagation in the pillar sample, not from a uniform plastic deformation. It is, in fact, equivalent to the situation of rigid-body sliding or bicrystal sliding [[180](#), [181](#)]. The measured strain should not be interpreted as general plasticity, at least in the conventional sense, since neither the two “crystals” deform. Furthermore, the constancy of load (or engineering stress) is not indicative of a perfectly plastic material, or has anything to do with work hardening or softening. Rather, it is a measure of friction of sliding between two rigid bodies. In the current study, it

represents the self frictional force of the Mg- and Zr-based BMGs.

5-1-6 Strain burst speed

It is well known that flow serration in the millimeter-sized BMG samples is a result of shear band propagation and when a shear band propagates there is an accompanied displacement burst. Recently, Song et al. [182] and Chen et al. [183] performed uniaxial compression tests on the Zr-, Mg- and Pd-based BMGs using high-sensitivity strain gauges directly attached to test sample and analyzed flow serration during inhomogeneous deformation. They demonstrated that shear-band propagating speed can be determined from the displacement-time profile.

The above-mentioned studies inspire us to carry out the microcompression tests to study the displacement burst rate of the micrometer-sized BMG pillar samples. Furthermore, in compressed micrometer-sized BMGs, localized shear is always revealed as the dominant deformation mode, and strain burst phenomena are observed in all microcompression tests. Based on the previous sections, the strain burst phenomenon is usually indicative of a sudden propagation of a localized shear band. Thus, it is of interest to examine the relationship between shear band and strain burst, especially for the estimation of the strain burst speed in pillar samples.

For microcompression tests of micropillars, the representative load-displacement and displacement-time curves of the Mg-based BMG are shown in Figures 4.10 and 4.11, respectively. Independent of the metallic glass system (Mg- or Zr-based BMG), micropillar diameter (1 or 3.8 μm) and compression strain rate (1×10^{-4} to $1 \times 10^{-2} \text{ s}^{-1}$), sudden strain bursts are always seen, as the example demonstrated in Figure 4.11. Note that the more

brittle-natured Mg-based BMG micropillars (with about 0% plastic strain for Mg based bulk rod compression specimens [158]) usually exhibit one strain bursts over the microcompression process, while the much more ductile phase-separation Zr based BMG micropillars (with about 13% plastic strain for their bulk rod compression samples [151]) show multiple strain bursts and the bursts proceed in a progressive fashion. The recorded displacement-time information and the extracted strain burst speed data allow a detailed analysis of the strain burst characteristics during compression. Table 5.1 summarizes all of the calculated strain burst speeds of the Mg- and Zr-based 1 and 3.8 μm pillars at different strain rates.

By close examination of the strain burst speed data in Table 5.1, there are clear trends showing the BMG alloy systems and the micropillar size dependences. For the 1 μm pillar samples, the strain burst speeds are scattered in the range of 747-1,551 and 110-469 nm/s for the Mg- and Zr-based BMG micropillars, respectively. The more brittle nature of the BMG is, the higher strain burst speed becomes. The difference can be 3-7 times. For the larger 3.8 μm pillar samples, the strain burst speeds are appreciably higher, being 9,178-10,619 and 818-4,000 nm/s for the Mg- and Zr-based BMG micropillars, respectively. The speed trend is the same as the 1 μm pillars, and the difference can be over one order of magnitude.

While there are apparent alloy systems and the pillar size dependences, the loading strain rate effect seems to be minor. From the Table 5.1, the strain burst speeds at a high strain rate are only slightly higher than those at a lower strain rate. For the ductile Zr based pillars, there is hardly any clear strain rate dependence. Note that the applied loading velocity of the machine system for these micropillars is in the range of 0.25-95 nm/s, which are much lower than the burst speeds.

For comparison of the strain burst speed, it is noted that the more ductile BMG seems to possess the lower strain burst speed, or the lower shear band propagation speed. It is thought that the above strain burst speed might be related to the metallic glass friction coefficient. Imagining the bicrystal sliding, the slide resistance is directly linked to the friction coefficient between the two crystals. It is the best way to measure the “intrinsic” friction coefficient of a BMG if we use a BMG tip to slide over the same BMG surface. Nevertheless, measuring the coefficient using a diamond tip can provide useful relative information and the basic trend. To demonstrate this, the nanoscratch tests are conducted on the Mg- and Zr-based BMGs. The nanoscratch results are also included in [Table 5.1](#).

From [Table 5.1](#), we note that the wear characteristics of BMG exhibit a direct relationship with the strain burst speed for the two BMGs. That is, based upon bicrystal sliding model, the higher wear resistance is usually accompanied by the lower strain burst speed. Thus, the trend obtained from microcompression tests can be rationalized by nanoscratch tests. Furthermore, the current finding from micropillars is consistent with the general trend that the more ductile BMG will show the slower shear band propagation, which was also demonstrated in millimeter-scaled compression samples [\[183\]](#).

However, the strain burst speed of micropillars is much lower than those obtained from compression of millimeter-scaled BMG [\[183\]](#). Presumably, the flat punch tip might have lost contact with pillar sample with a certain load when the shear band propagates. As a result of that, the strain burst speed (or shear band speed) is only a lower limit value. To characterize the strain burst speed, a more accurate testing machine or higher data acquisition rate is needed. The information obtained from the current study can only be qualitative, but the quantitatively measurement of strain burst speed needs further investigation in the future.

5-2 High temperature microcompression test

In addition to the strong sample size dependence of the mechanical properties of BMG micropillars, the temperature dependence of the deformation of BMG micropillars is also investigated. Two kinds of indenter systems, MTS Nanoindenter XP and Hysitron Triboindenter, are chosen for high temperature microcompression tests to investigate the mechanical behavior of Au-based BMG over a wide range of test temperatures. In the following section, the effect of temperature on elastic modulus and apparent yield strength of the Au-based BMG pillar samples are discussed. In addition, the homogeneous flow is subsequently analyzed using the deformation model of BMG.

5-2-1 Effect of temperature on mechanical behavior

For the 1 μm Au-based BMG pillar samples, high temperature microcompression tests are conducted at temperatures of 343, 373, 383, 393, 403 and 408 K with an initial strain rate of $1 \times 10^{-2} \text{ s}^{-1}$. Based on the experimental data, the transition from inhomogeneous to homogeneous flow is clearly observed near the glass transition temperature, as shown in [Figure 4.22](#). The term “inhomogeneous flow” as used here means the shear failure triggered by major shear band propagation. Conversely, the term “homogeneous flow” means uniform deformation of the pillar sample, i.e., size and shape of the cross-section of the deformed micropillar change simultaneously everywhere along the loading axis and no shear localization is observed.

Subsequently, in order to analyze the temperature effect on elastic modulus and yield strength, the elastic modulus of the Au-based BMG pillar samples are evaluated using the same method of room temperature microcompression described in section 5-1-1. The values

of elastic modulus and apparent yield strength are plotted in [Figure 5.10](#) with respect to temperature. It is noted that the elastic modulus and apparent yield strength of the 1 μm Au-based pillar samples appear the severe transition at 383 K ($0.95 T_g$), and we call this temperature as “softening temperature” at $1 \times 10^{-2} \text{ s}^{-1}$. As demonstrated in [Figure 4.22](#), the deformation of micropillars below 383 K is the same with the behavior of micropillars at room temperature, which is the emission of shear band in the manner of strain burst. Therefore, the deformation temperature below softening temperature, 383 K, is referred to as the inhomogeneous deformation. The slope of yield strength and modulus versus temperature of micropillars remain essentially unchanged or changed very little at temperature below $0.95 T_g$; however, the strength and modulus of micropillars appear the steep soft at 383-403 K ($0.95 - 1.0 T_g$).

Generally speaking, it is thought that the deformation temperature above softening temperature will be a homogeneous deformation at a constant strain rate; however, the morphology of deformed pillars at 393 K is still observed existence of the shear bands, as shown in [Figure 4.25\(f\)](#), similar with the pillars below 383 K. As the temperature above 403 K, which is called “homogeneous temperature”, the deformed pillars are homogeneous deformation without shear bands, as shown in [Figure 4.26](#), and the time-displacement curve is stable slope of 20 nm/s even if yielding, as shown in [Figure 4.23](#). Therefore, it appeared a transitional region between softening temperature and homogeneous temperature, the shear bands still propagating throughout the entire pillar even if the flow stress had already shown the softening phenomenon. As the temperature above this transitional region, this 1 μm pillar at $1 \times 10^{-2} \text{ s}^{-1}$ could fully homogeneous deformation with flow stress of 500-600 MPa without shear bands. It is suggested that the working temperature should be raised above 400 K if this Au-based BMG would be applied the micro-forming.

5-2-2 Homogeneous flow

For the 3.8 μm Au-based BMG pillar samples, high temperature microcompression tests are performed at temperatures of 395.9 and 401.2 K with an nominal strain rates ranging from 10^{-3} to 10^{-2} s^{-1} . The true stress-strain curves of the Au-based BMG pillar samples are shown in Figure 4.29. As shown in Figure 4.29, the existence of a steady state in stress-strain curves is usually regarded as a dynamic equilibrium between strain induced structure disorder (e.g., free volume creation) and structural relaxation (e.g., free volume annihilation) [103, 106, 129]. Based on experimental data, the steady-state flow stress against strain rate is plotted in Figure 5.11 to elucidate the deformation mechanism in the current Au-based BMG at high temperatures. At low strain rates, the strain rate sensitivity (m) is about 0.87, which is close to that for a Newtonian flow ($m=1$) but gradually changes to non-Newtonian at high strain rates. This Newtonian to non-Newtonian transition is also observed previously in several other BMG systems [100, 102]. In addition, this transition from Newtonian to non-Newtonian flow is also observed in the curves of strain rate dependence of the viscosity, as shown in Figure 5.12. The viscosity is calculated from the flow stress by $\eta = \sigma_{flow} / 3\dot{\epsilon}$ in which σ_{flow} is the flow stress and $\dot{\epsilon}$ is strain rate.

Based upon the free volume and STZ model, the strain rate during homogeneous deformation of BMG can be described by [31, 119]

$$\dot{\epsilon} = \alpha \varepsilon_0 \nu_G \exp\left(-\frac{\Delta F}{kT}\right) \sinh\left(\frac{\sigma V}{2\sqrt{3}kT}\right) = \dot{\epsilon}_T \sinh\left(\frac{\sigma V}{2\sqrt{3}kT}\right), \quad (5-1)$$

where $\dot{\epsilon}_T = \alpha \varepsilon_0 \nu_G \exp(-\Delta F/kT)$ is a temperature-dependent rate constant, α is the steady state fraction of matter capable of undergoing shear transformations, ν_G is the normal mode frequency of the flow unit along the activation path, $\alpha \varepsilon_0 \nu_G \sim 10^{11}$ s^{-1} [119], kT has its usual

meaning, and V is the activation volume ($V=v_0\varepsilon_0$, in which v_0 is the volume of a flow unit or STZ which undergoes a strain ε_0 (~ 0.125 during deformation [31, 119]). The stress versus strain rate data in Figure 5.11 can be fitted by Eq. (5-1) and plotted as solid lines at the two given temperatures. The fitting parameters, $\dot{\varepsilon}_T$, V , and v_0 , are listed in Table 5.2.

The activation volume V is about $55\text{--}62 \text{ \AA}^3$, which has a similar magnitude as reported in other BMGs (60 \AA^3 for a Zr-BMG [105], 105 \AA^3 for a Pd-BMG [119]). The volume of the basic flow unit (STZ) v_0 in this Au-BMG is then estimated to be $440\text{--}496 \text{ \AA}^3$. Since the present Au-BMG has a density of 13.72 g/cm^3 and an atomic weight of 126.5 g/mol , the average atomic volume equals 15.3 \AA^3 . Therefore, a STZ in the current Au-based BMG contains about $N=29\text{--}32$ atoms. This value is similar to that calculated in a Pd-BMG [119]. Argon pointed out that STZ is in a disk shape during inhomogeneous deformation but is more reasonably in spherical shape during homogeneous deformation [119]. Assuming a spherical shape, the radius of the sphere would be about 5 \AA which is particularly noted to be similar to the radius where the second peak occurs in the pair distribution functions (PDF) or radial distribution functions (RDF) in an amorphous Au-Si alloy ($\sim 5 \text{ \AA}$) and that in other BMGs ($4\text{--}6 \text{ \AA}$) [184]. Since the peaks in PDF indicate the density fluctuation, or multi-range order in glass, with the first one being the distance between two neighbor atoms, and the second peak being the smallest range order (e.g., STZ), the present result is consistent with the PDF measurements.

According to Argon's model, the Helmholtz free energy barrier or the activation energy, ΔF , in Eq. (5-1) can be calculated by

$$\Delta F = \left[\left(\frac{7-5\nu}{30(1-\nu)} + \frac{2(1+\nu)}{9(1-\nu)} \right) \varepsilon_0 + \frac{1}{2} \frac{\tilde{\tau}}{\mu} \right] \mu V, \quad (5-2)$$

where $\nu=0.406$ is the Poisson's ratio for Au-BMG [18], $\tilde{\tau}$ is the ideal shear resistance, μ is the shear modulus (26.45 GPa for Au-based BMG [18]), and $\tilde{\tau} / \mu \approx 0.03$ [119]. Thus, the activation energy is theoretically estimated from Eq. (5-2) to be 99-120 kJ/mol. Using the fitted data in Table 5.2, we can also experimentally estimate the Helmholtz free energy barrier for viscous flow from the pre-hyperbolic sine term $\dot{\epsilon}_T = \alpha \epsilon_0 \nu_G \exp(-\Delta F / kT)$. It is about 103-104 kJ/mol, which agrees remarkably with the theoretical prediction.

Chapter 6 Conclusions

Microcompression tests are conducted on a typical of brittle Mg-based BMG and a ductile phase-separated Zr-based BMG. In addition, the stress-strain behavior of an Au-based BMG is investigated experimentally over a wide range of temperatures. The following conclusions are drawn from this study.

- (1) Micropillar with diameters of 3.8, 1 and 0.7 μm are fabricated successfully from the Mg- and Zr-based BMGs using focus ion beam, and then tested in microcompression at room temperature and strain rates from 1×10^{-4} to $1 \times 10^{-2} \text{ s}^{-1}$.
- (2) For the Mg-based BMGs, the strength of the micropillars is 1342 to 1580 MPa, an increase of 60-100% as compared to ~ 800 MPa for the bulk sample; for Zr-based BMGs, the apparent yield strength of the micropillars is 1992 to 2972 MPa, which shows a 25-86% increase over that of the bulk samples (~ 1600 MPa).
- (3) For the Mg- and Zr-based BMGs, at all sizes, the plastic flow is localized in shear bands and manifested as strain bursts to release the energy. According to the morphology of deformed pillars, there are more shear bands in the Zr-based BMGs as compared to that in Mg-based BMGs, consistent with the fact that the Zr-based BMGs are more ductile than the Mg-based BMGs.
- (4) The strength increase can be rationalized by the Weibull statistics for brittle materials, and the Weibull moduli of the Mg- and Zr- based BMGs are estimated to be about 35 and 60, respectively. The higher Weibull modulus of the Zr-based BMG

is consistent with the more ductile nature of this system.

- (5) According to the TEM results of pillar, all of these results demonstrate that alloy is an amorphous structure and no obvious crystalline structure before and after compression.
- (6) Strain burst phenomena are observed in all microcompression tests as indications of localized shearing. The strain burst speed of micropillars can be measured using the raw displacement-time data. The results indicated that the strain burst speed of the metallic glass increases with increasing sample size, decreasing wear resistance, and decreasing ductility.
- (7) High temperature microcompression tests are performed, for the first time, to investigate the deformation behavior of micron-sized Au-based BMG pillar samples from room to its glass transition temperature (~ 400 K).
- (8) A transition from inhomogeneous flow to homogeneous flow is clearly observed at or near the glass transition temperature. Specifically, for $1 \mu\text{m}$ Au-based BMG pillars, the flow transition temperature is about 393 K at strain rate of $1 \times 10^{-2} \text{ s}^{-1}$.
- (9) For $3.8 \mu\text{m}$ Au-based BMG pillar samples, homogeneous deformation of the Au-based BMG pillar sample is observed and no stress overshoot is detected at $395.9\text{-}401.2$ K. The strain rate sensitivity was about 0.87 at a strain rate of 10^{-3} s^{-1} .
- (10) Based on the STZ model, the volume of the basic flow unit (STZ) was calculated to be $440\text{-}496 \text{ \AA}^3$, equivalent to about 30 atoms. The Helmholtz free energy barrier was

also estimated to be 99-120 kJ/mol, compared favorably with the theoretical prediction.

References

- [1] A. C. Lund and C. A. Schuh, *Journal of Applied Physics*, 2004, 95, 4815-4822.
- [2] K. Mohri, *Ieee Transactions on Magnetics*, 1984, 20, 942-947.
- [3] E. Hristoforou and R. E. Reilly, *Ieee Transactions on Magnetics*, 1994, 30, 2728-2733.
- [4] A. Inoue, *Materials Science and Engineering A*, 2001, 304-306, 1-10.
- [5] N. H. Pryds, *Materials Science and Engineering A*, 2004, 375-377, 186-193.
- [6] A. Inoue, K. Ohtera, K. Kita and T. Masumoto, *Japanese Journal of Applied Physics* 1988, 27, L2248-L2251.
- [7] S. G. Kim, A. Inoue and T. Masumoto, *Materials Transactions, JIM*, 1990, 31, 929-934.
- [8] A. Inoue, A. Kato, T. Zhang, S. G. Kim and T. Masumoto, *Materials Transactions, JIM*, 1991, 32, 609-616.
- [9] A. Inoue, T. Nakamura, N. Nishiyama and T. Masumoto, *Materials Transactions, JIM*, 1992, 33, 937-945.
- [10] X. K. Xi, R. J. Wang, D. Q. Zhao, M. X. Pan and W. H. Wang, *Journal of Non-Crystalline Solids*, 2004, 344, 105-109.
- [11] H. Men, W. T. Kim and D. H. Kim, *Journal of Non-Crystalline Solids*, 2004, 337, 29-35.
- [12] A. Inoue, T. Zhang and T. Masumoto, *Materials Transactions, JIM*, 1990, 31, 177-183.
- [13] T. Zhang, A. Inoue and T. Masumoto, *Materials Transactions, JIM*, 1991, 32, 1005-1010.
- [14] A. Peker and W. L. Johnson, *Applied Physics Letters*, 1993, 63, 2342-2344.
- [15] A. Inoue, T. Zhang, N. Nishiyama, K. Ohba and T. Masumoto, *Materials Transactions, JIM*, 1993, 34, 1234-1237.

- [16] W. Klement, R. H. Willens and P. Duwez, *Nature*, 1960, 187, 869-870.
- [17] H. S. Chen and D. Turnbull, *Journal of Chemical Physics*, 1968, 48, 2560-2571.
- [18] J. Schroers, B. Lohwongwatana, W. L. Johnson and A. Peker, *Applied Physics Letters*, 2005, 87, 061912.
- [19] C. C. Hays, C. P. Kim and W. L. Johnson, *Physical Review Letters*, 2000, 84, 2901-2904.
- [20] L. Q. Xing, Y. Li, K. T. Ramesh, J. Li and T. C. Hufnagel, *Physical Review B*, 2001, 64, 180201.
- [21] H. Choi-Yim, R. D. Conner, F. Szuecs and W. L. Johnson, *Acta Materialia*, 2002, 50, 2737-2745.
- [22] A. Inoue, W. Zhang, T. Tsurui, A. R. Yavari and A. L. Greer, *Philosophical Magazine Letters*, 2005, 85, 221-229.
- [23] Y. K. Xu, H. Ma, J. Xu and E. Ma, *Acta Materialia*, 2005, 53, 1857-1866.
- [24] J. S. C. Jang, J. Y. Ciou, T. H. Hung, J. C. Huang and X. H. Du, *Applied Physics Letters*, 2008, 92, 011930.
- [25] A. Inoue, T. Zhang and Y. H. Kim, *Materials Transactions, JIM*, 1997, 38, 749-755.
- [26] E. S. Park and D. H. Kim, *Acta Materialia*, 2006, 54, 2597-2604.
- [27] K. F. Yao, F. Ruan, Y. Q. Yang and N. Chen, *Applied Physics Letters*, 2006, 88, 122016.
- [28] Y. H. Liu, G. Wang, R. J. Wang, D. Q. Zhao, M. X. Pan and W. H. Wang, *Science*, 2007, 315, 1385-1388.
- [29] M. D. Uchic, D. M. Dimiduk, J. N. Florando and W. D. Nix, *Science*, 2004, 305, 986-989.
- [30] C. A. Volkert and E. T. Lilleodden, *Philosophical Magazine*, 2006, 86, 5567-5579.
- [31] F. Spaepen, *Acta Metallurgica*, 1977, 25, 407-415.
- [32] A. S. Argon, *Acta Metallurgica*, 1979, 27, 47-58.

- [33] C. A. Schuh, T. C. Hufnagel and U. Ramamurty, *Acta Materialia*, 2007, 55, 4067-4109.
- [34] Q. Zheng, S. Cheng, J. H. Strader, E. Ma and J. Xu, *Scripta Materialia*, 2007, 56, 161-164.
- [35] R. D. Conner, Y. Li, W. D. Nix and W. L. Johnson, *Acta Materialia*, 2004, 52, 2429-2434.
- [36] M. F. Ashby and A. L. Greer, *Scripta Materialia*, 2006, 54, 321-326.
- [37] H. S. Chen and D. Turnbull, *Acta Metallurgica*, 1969, 17, 1021-1031.
- [38] H. S. Chen, *Acta Metallurgica*, 1974, 22, 1505-1511.
- [39] A. J. Drehman, A. L. Greer and D. Turnbull, *Applied Physics Letters*, 1982, 41, 716-717.
- [40] H. W. Kui, A. L. Greer and D. Turnbull, *Applied Physics Letters*, 1984, 45, 615-616.
- [41] C. C. Koch, O. B. Cavin, C. G. McKamey and J. O. Scarbrough, *Applied Physics Letters*, 1983, 43, 1017-1019.
- [42] A. W. Weeber and H. Bakker, *Physica B*, 1988, 153, 93-135.
- [43] R. B. Schwarz and W. L. Johnson, *Physical Review Letters*, 1983, 51, 415-418.
- [44] P. Ziemann, *Materials Science and Engineering*, 1985, 69, 95-103.
- [45] X. L. Yeh, K. Samwer and W. L. Johnson, *Applied Physics Letters*, 1983, 42, 242-244.
- [46] Z. H. Yan, T. Klassen, C. Michaelsen, M. Oehring and R. Bormann, *Physical Review B*, 1993, 47, 8520-8527.
- [47] A. Inoue, T. Zhang and T. Masumoto, *Materials Transactions, JIM*, 1989, 30, 965-972.
- [48] A. Inoue, *Acta Materialia*, 2000, 48, 279-306.
- [49] A. Inoue, *Materials Transactions, JIM*, 1995, 36, 866-875.
- [50] A. Inoue, N. Nishiyama and H. Kimura, *Materials Transactions, JIM*, 1997, 38, 179-183.

- [51] N. Nishiyama and A. Inoue, *Applied Physics Letters*, 2002, 80, 568-570.
- [52] D. Turnbull and J. C. Fisher, *Journal of Chemical Physics*, 1949, 17, 71-73.
- [53] Z. P. Lu, Y. Li and S. C. Ng, *Journal of Non-Crystalline Solids*, 2000, 270, 103-114.
- [54] Z. P. Lu, H. Tan, Y. Li and S. C. Ng, *Scripta Materialia*, 2000, 42, 667-673.
- [55] T. A. Waniuk, J. Schroers and W. L. Johnson, *Applied Physics Letters*, 2001, 78, 1213-1215.
- [56] A. Inoue, W. Zhang, T. Zhang and K. Kurosaka, *Acta Materialia*, 2001, 49, 2645-2652.
- [57] T. D. Shen, Y. He and R. B. Schwarz, *Journal of Materials Research*, 1999, 14, 2107-2115.
- [58] T. D. Shen and R. B. Schwarz, *Applied Physics Letters*, 1999, 75, 49-51.
- [59] B. S. Murty and K. Hono, *Materials Transactions, JIM*, 2000, 41, 1538-1544.
- [60] Z. P. Lu and C. T. Liu, *Acta Materialia*, 2002, 50, 3501-3512.
- [61] Z. P. Lu and C. T. Liu, *Intermetallics*, 2004, 12, 1035-1043.
- [62] X. H. Du, J. C. Huang, C. T. Liu and Z. P. Lu, *Journal of Applied Physics*, 2007, 101, 086108.
- [63] A. Inoue, *Materials Science and Engineering*, 1997, A226-228, 357-363.
- [64] A. Inoue, A. Takeuchi and T. Zhang, *Metallurgical and Materials Transaction*, 1998, A29, 1779-1793.
- [65] A. Inoue, T. Zhang and A. Takeuchi, *Materials Science Forum*, 1998, 269-272, 855-864.
- [66] D. Turnbull, *Contemporary Physics*, 1969, 10, 473-488.
- [67] R. E. Reed-Hill, *Physical Metallurgy Principles*, PWS, Boston, USA, 1994.
- [68] A. L. Greer, *Science*, 1995, 267, 1947-1953.
- [69] C. T. Liu, L. Heatherly, D. S. Easton, C. A. Carmichael, J. H. Schneibel, C. H. Chen, J. L. Wright, M. H. Yoo, J. A. Horton and A. Inoue, *Metallurgical and Materials*

- Transaction, 1998, A29, 1811-1820.
- [70] W. L. Johnson, *Mrs Bulletin*, 1999, 24, 42-56.
- [71] A. S. Argon and H. Y. Kuo, *Materials Science and Engineering*, 1979, 39, 101-109.
- [72] M. L. Falk, *Physical Review B*, 1999, 60, 7062-7070.
- [73] V. V. Bulatov and A. S. Argon, *Modelling and Simulation in Materials Science and Engineering*, 1994, 2, 185-202.
- [74] M. L. Falk and J. S. Langer, *Physical Review E*, 1998, 57, 7192-7205.
- [75] J. S. Langer and L. Pechenik, *Physical Review E*, 2003, 68, 061507.
- [76] J. S. Langer, *Physical Review E*, 2004, 70, 041502.
- [77] E. Bouchbinder, J. S. Langer and I. Procaccia, *Physical Review E*, 2007, 75, 036107.
- [78] J. S. Langer, *Physical Review E*, 2008, 77, 021502.
- [79] M. Zink, K. Samwer, W. L. Johnson and S. G. Mayr, *Physical Review B*, 2006, 73, 3.
- [80] M. H. Cohen and D. Turnbull, *Journal of Chemical Physics*, 1959, 31, 1164-1169.
- [81] D. E. Polk and D. Turnbull, *Acta Metallurgica*, 1972, 20, 493-498.
- [82] Z. F. Zhang, F. F. Wu, G. He and J. Eckert, *Journal of Materials Science & Technology*, 2007, 23, 747-767.
- [83] Q. Xue, M. A. Meyers and V. F. Nesterenko, *Acta Materialia*, 2002, 50, 575-596.
- [84] P. E. Donovan and W. M. Stobbs, *Acta Metallurgica*, 1981, 29, 1419-1436.
- [85] E. Pekarskaya, C. P. Kim and W. L. Johnson, *Journal of Materials Research*, 2001, 16, 2513-2518.
- [86] J. Li, F. Spaepen and T. C. Hufnagel, *Philosophical Magazine A*, 2002, 82, 2623-2630.
- [87] W. H. Jiang and M. Atzmon, *Acta Materialia*, 2003, 51, 4095-4105.
- [88] W. H. Jiang and M. Atzmon, *Scripta Materialia*, 2006, 54, 333-336.
- [89] Y. Zhang and A. L. Greer, *Applied Physics Letters*, 2006, 89, 071907.
- [90] T. W. Wright. *The Physics and Mathematics of Adiabatic Shear Bands*. Cambridge:

Cambridge University Press, 2002.

- [91] B. Yang, M. L. Morrison, P. K. Liaw, R. A. Buchanan, G. Y. Wang, C. T. Liu and M. Denda, *Applied Physics Letters*, 2005, 86, 141904.
- [92] J. J. Lewandowski and A. L. Greer, *Nature Materials*, 2006, 5, 15-18.
- [93] B. Yang, C. T. Liu, T. G. Nieh, M. L. Morrison, P. K. Liaw and R. A. Buchanan, *Journal of Materials Research*, 2006, 21, 915-922.
- [94] Y. Kawamura, T. Shibata, A. Inoue and T. Masumoto, *Acta Materialia*, 1997, 46, 253-263.
- [95] M. D. Demetriou and W. L. Johnson, *Journal of Applied Physics*, 2004, 95, 2857-2865.
- [96] M. D. Demetriou and W. L. Johnson, *Acta Materialia*, 2004, 52, 3403-3412.
- [97] M. D. Demetriou and W. L. Johnson, *Materials Science and Engineering A*, 2004, 375, 270-275.
- [98] G. Wang, J. Shen, J. F. Sun, Y. J. Huang, J. Zou, Z. P. Lu, Z. H. Stachurski and B. D. Zhou, *Journal of Non-Crystalline Solids*, 2005, 351, 209-217.
- [99] J. Schroers and N. Paton, *Advanced Materials & Processes*, 2006, 164, 61-63.
- [100] H. Kato, Y. Kawamura, A. Inoue and H. S. Chen, *Applied Physics Letters*, 1998, 73, 3665-3667.
- [101] Y. Kawamura, T. Nakamura, H. Kato, H. Mano and A. Inoue, *Materials Science and Engineering A*, 2001, 304-306, 674-678.
- [102] T. G. Nieh and J. Wadsworth, *Scripta Materialia*, 2006, 54, 387-392.
- [103] P. De Hey, J. Sietsma and A. Van den Beukel, *Acta Materialia*, 1998, 46, 5873-5882.
- [104] Y. Kawamura, T. Shibata, A. Inoue and T. Masumoto, *Materials Transactions, JIM*, 1999, 40, 335-342.
- [105] A. Reger-Leonhard, M. Heilmaier and J. Eckert, *Scripta Materialia*, 2000, 43, 459-464.

- [106] H. S. Chen, H. Kato and A. Inoue, *Materials Transactions, JIM*, 2001, 42, 597-605.
- [107] M. Bletry, P. Guyot, J. J. Blandin and J. L. Soubeyroux, *Acta Materialia*, 2006, 54, 1257-1263.
- [108] K. Wang, T. Fujita, Y. Q. Zeng, N. Nishiyama, A. Inoue and M. W. Chen, *Acta Materialia*, 2008, 56, 2834-2842.
- [109] H. S. Chen, *Scripta Metallurgica*, 1973, 7, 931-935.
- [110] W. J. Wright, R. B. Schwarz and W. D. Nix, *Materials Science and Engineering A*, 2001, 319-321, 229-232.
- [111] Y. I. Golovin, V. I. Ivolgin, V. A. Khonik, K. Kitagawa and A. I. Tyurin, *Scripta Materialia*, 2001, 45, 947-952.
- [112] W. J. Wright, R. Saha and W. D. Nix, *Materials Transactions, JIM*, 2001, 42, 642-649.
- [113] B. Moser, J. Kuebler, H. Meinhard, W. Muster and J. Michler, *Advanced Engineering Materials*, 2005, 7, 388-392.
- [114] P. Murah and U. Ramamurty, *Acta Materialia*, 2005, 53, 1467-1478.
- [115] G. P. Zhang, W. Wang, B. Zhang, J. Tan and C. S. Liu, *Scripta Materialia*, 2005, 52, 1147-1151.
- [116] H. W. Zhang, X. N. Jing, G. Subhash, L. J. Kecskes and R. J. Dowding, *Acta Materialia*, 2005, 53, 3849-3859.
- [117] B. Moser, J. F. Loffler and J. Michler, *Philosophical Magazine*, 2006, 86, 5715-5728.
- [118] C. A. Schuh, A. C. Lund and T. G. Nieh, *Acta Materialia*, 2004, 52, 5879-5891.
- [119] A. S. Argon and L. T. Shi, *Acta Metallurgica*, 1983, 31, 499-507.
- [120] J. M. Pelletier, B. Van de Moortele and I. R. Lu, *Materials Science and Engineering A*, 2002, 336, 190-195.
- [121] M. Bletry, P. Guyot, Y. Brechet, J. J. Blandin and J. L. Soubeyroux, *Materials Science and Engineering A*, 2004, 387-389, 1005-1011.
- [122] M. Heilmaier and J. Eckert, *Advanced Engineering Materials*, 2005, 7, 833-841.

- [123] Q. Wang, J. M. Pelletier, J. J. Blandin and M. Suery, *Journal of Non-Crystalline Solids*, 2005, 351, 2224-2231.
- [124] M. Bletry, P. Guyot, Y. Brechet, J. J. Blandin and J. L. Soubeyroux, *Acta Materialia*, 2007, 55, 6331-6337.
- [125] X. L. Fu, Y. Li and C. A. Schuh, *Acta Materialia*, 2007, 55, 3059-3071.
- [126] S. F. Guo, K. C. Chan, Q. Chen, J. J. Li and L. Liu, *Scripta Materialia*, 2009, 60, 369-372.
- [127] B. Yang, J. Wadsworth and T. G. Nieh, *Applied Physics Letters*, 2007, 90, 061911.
- [128] M. Heggen, F. Spaepen and M. Feuerbacher, *Journal of Applied Physics*, 2005, 97, 8.
- [129] F. Spaepen, *Scripta Materialia*, 2006, 54, 363-367.
- [130] K. S. Lee, H. J. Jun, S. Pauly, B. Bartusch, Y. W. Chang and J. Eckert, *Intermetallics*, 2009, 17, 65-71.
- [131] M. D. Uchic and D. M. Dimiduk, *Materials Science and Engineering A*, 2005, 400-401, 268-278.
- [132] K. J. Hemker and W. N. Sharpe, *Annual Review of Materials Research*, 2007, 37, 93-126.
- [133] Q. Feng, Y. N. Picard, H. Liu, S. M. Yalisove, G. Mourou and T. M. Pollock, *Scripta Materialia*, 2005, 53, 511-516.
- [134] B. H. Kim, S. H. Ryu, D. K. Choi and C. N. Chu, *Journal of Micromechanics and Microengineering*, 2005, 15, 124-129.
- [135] D. M. Dimiduk, M. D. Uchic and T. A. Parthasarathy, *Acta Materialia*, 2005, 53, 4065-4077.
- [136] H. Zhang, B. E. Schuster, Q. Wei and K. T. Ramesh, *Scripta Materialia*, 2006, 54, 181-186.
- [137] J. R. Greer, W. C. Oliver and W. D. Nix, *Acta Materialia*, 2005, 53, 1821-1830.
- [138] M. D. Uchic, D. M. Dimiduk, R. Wheeler, P. A. Shade and H. L. Fraser, *Scripta*

- Materialia, 2006, 54, 759-764.
- [139] B. E. Schuster, Q. Wei, H. Zhang and K. T. Ramesh, Applied Physics Letters, 2006, 88, 103112.
- [140] H. Bei, S. Shim, E. P. George, M. K. Miller, E. G. Herbert and G. M. Pharr, Scripta Materialia, 2007, 57, 397-400.
- [141] B. E. Schuster, Q. Wei, M. H. Ervin, S. O. Hruszkewycz, M. K. Miller, T. C. Hufnagel and K. T. Ramesh, Scripta Materialia, 2007, 57, 517-520.
- [142] S. Cheng, X. L. Wang, H. Choo and P. K. Liaw, Applied Physics Letters, 2007, 91, 201917.
- [143] A. Takeuchi and A. Inoue, Materials Transactions, JIM, 2000, 41, 1372-1378.
- [144] X. Y. Yan, Y. A. Chang, Y. Yang, F. Y. Xie, S. L. Chen, F. Zhang, S. Daniel and M. H. He, Intermetallics, 2001, 9, 535-538.
- [145] X. H. Lin and W. L. Johnson, Journal of Applied Physics, 1995, 78, 6514-6519.
- [146] Y. Yang, Y. A. Chang, J. C. Zhao and B. P. Bewlay, Intermetallics, 2003, 11, 407-415.
- [147] N. Sanders and A. P. Miodownik. CALPHAD, Calculation of Phase Diagrams: A Comprehensive Guide. Elsevier Science. Oxford, UK. 1998.
- [148] L. Kaufman and H. Bernstein. Computer Calculation of Phase Diagrams. Academic. New York and London. 1970.
- [149] Y. A. Chang, S. L. Chen, F. Zhang, X. Y. Yan, F. Y. Xie, R. Schmid-Fetzer and W. A. Oates, Progress in Materials Science, 2004, 49, 313-345.
- [150] Y. A. Chang, Metallurgical and Materials Transactions a-Physical Metallurgy and Materials Science, 2006, 37A, 273-305.
- [151] X. H. Du, J. C. Huang, K. C. Hsieh, Y. H. Lai, H. M. Chen, J. S. C. Jang and P. K. Liaw, Applied Physics Letters, 2007, 91, 131901.
- [152] PANDAT. 6.0-Phase Diagram Calculation Software for Multicomponent Systems, CompuTherm LLC, 437 S. Yellowstone Dr., Suite 217. Madison, WI 53719. USA.

- [153] B. B. Sun, Y. B. Wang, J. Wen, H. Yang, M. L. Sui, J. Q. Wang and E. Ma, *Scripta Materialia*, 2005, 53, 805-809.
- [154] E. C. G. Kirk, D. A. Williams and H. Ahmed, *Institute of Physics Conference Series*, 1989, 501-506.
- [155] M. H. F. Overwijk, F. C. Vandenheuvell and C. W. T. Bulleliuwma, *Journal of Vacuum Science & Technology B*, 1993, 11, 2021-2024.
- [156] R. M. Langford and A. K. Petford-Long, *Journal of Vacuum Science & Technology* 2001, 19, 2186-2193.
- [157] C. A. Schuh, C. E. Packard and A. C. Lund, *Journal of Materials Research*, 2006, 21, 725-736.
- [158] H. M. Chen, Y. C. Chang, T. H. Hung, X. H. Du, J. C. Huang, J. S. C. Jang and P. K. Liaw, *Materials Transactions, JIM*, 2007, 48, 1802-1805.
- [159] J. J. Lewandowski, W. H. Wang and A. L. Greer, *Philosophical Magazine Letters*, 2005, 85, 77-87.
- [160] Z. F. Zhang, J. Eckert and L. Schultz, *Acta Materialia*, 2003, 51, 1167-1179.
- [161] Z. F. Zhang, G. He, J. Eckert and L. Schultz, *Physical Review Letters*, 2003, 91, 045505.
- [162] Z. F. Zhang and J. Eckert, *Physical Review Letters*, 2005, 94, 094301.
- [163] Y. S. Choi, M. D. Uchic, T. A. Parthasarathy and D. M. Dimiduk, *Scripta Materialia*, 2007, 57, 849-852.
- [164] W. D. Nix and H. J. Gao, *Journal of the Mechanics and Physics of Solids*, 1998, 46, 411-425.
- [165] J. G. Swadener, E. P. George and G. M. Pharr, *Journal of the Mechanics and Physics of Solids*, 2002, 50, 681-694.
- [166] J. F. Archard, *Journal of Applied Physics*, 1953, 24, 981-988.
- [167] J. G. Wang, B. W. Choi, T. G. Nieh and C. T. Liu, *Journal of Materials Research*, 2000,

- 15, 913-922.
- [168] A. M. Hodge and T. G. Nieh, *Intermetallics*, 2004, 12, 741-748.
- [169] H. Bei and S. Shim, *Applied Physics Letters*, 2007, 91, 111915.
- [170] B. E. Schuster, Q. Wei, T. C. Hufnagel and K. T. Ramesh, *Acta Materialia*, 2008, 56, 5091-5100.
- [171] M. Fukuda, S. Tomimatsu, K. Nakamura, M. Koguchi, H. Shichi and K. Umemura, *Journal of Electron Microscopy*, 2004, 53, 479-483.
- [172] K. Thompson, D. Lawrence, D. J. Larson, J. D. Olson, T. F. Kelly and B. Gorman, *Ultramicroscopy*, 2007, 107, 131-139.
- [173] W. Weibull, *Journal of Applied Mechanics*, 1951, 18, 293-297.
- [174] D. R. Askeland, *Science and Engineering of Materials*, PWS Publishing, Boston, MA, 1994.
- [175] W. F. Wu, Y. Li and C. A. Schuh, *Philosophical Magazine*, 2008, 88, 71-89.
- [176] Y. Y. Zhao, E. Ma and J. Xu, *Scripta Materialia*, 2008, 58, 496-499.
- [177] G. E. Dieter, *Mechanical Metallurgy*, McGraw-Hill Book Company, New York, 1986.
- [178] S. S. Brenner, *Journal of Applied Physics*, 1956, 27, 1848-1956.
- [179] Y. F. Gao, B. Yang and T. G. Nieh, *Acta Materialia*, 2007, 55, 2319-2327.
- [180] T. Watanabe, M. Yamada, S. Shima and S. Karashima, *Philosophical Magazine A*, 1979, 40, 667-683.
- [181] S. Miura, K. Hamashima and K. T. Aust, *Acta Metallurgica*, 1980, 28, 1591-1602.
- [182] S. X. Song and T. G. Nieh, *Intermetallics*, 2009, 17, 762-767.
- [183] H. M. Chen, J. C. Huang, S. X. Song, T. G. Nieh and J. S. C. Jang, *Applied Physics Letters*, 2009, 94, 141914.
- [184] G. S. Cargill, *Journal of Applied Physics*, 1970, 41, 12-29.

Table 1.1 Fundamental properties and application fields of bulk metallic glasses and nanocrystalline alloys [4].

Fundamental characteristic	Application field
High strength	Machinery structural materials
High hardness	Optical precision materials
High fracture toughness	Die materials
High impact fracture energy	Tool materials
High fatigue strength	Cutting materials
High elastic energy	Electrode materials
High corrosion resistance	Corrosion resistant materials
High wear resistance	Hydrogen storage materials
High viscous flowability	Ornamental materials
High reflection ratio	Composite materials
Good soft magnetism	Writing appliance materials
High frequency permeability	Sporting goods materials
High magnetostriction	Bonding materials
Efficient electrode (chlorine gas)	Soft magnetic materials
High hydrogen storage	High magnetostrictive materials

Table 2.1 Bulk metallic glasses and their published year [48].

	Years
I. Nonferrous metal base	
Mg–Ln–M (Ln = Lanthanide metal, M = Ni, Cu or Zn)	1988
Ln–Al–TM (TM = VI~VIII group transition metal)	1989
Ln–Ga–TM	1989
Zr–Al–TM	1990
Zr–Ti–Al–TM	1990
Ti–Zr–TM	1993
Zr–Ti–TM–Be	1993
Zr–(Nb,Pd)–Al–TM	1995
Pd–Cu–Ni–P	1996
Pd–Ni–Fe–P	1996
Pd–Cu–B–Si	1997
Ti–Ni–Cu–Sn	1998
II. Ferrous group metal base	
Fe–(Al,Ga)–(P,C,B,Si,Ge)	1995
Fe–(Nb,Mo)–(Al,Ga)–(P,B,Si)	1995
Co–(Al,Ga)–(P,B,Si)	1996
Fe–(Zr,Hf,Nb)–B	1996
Co–Fe–(Zr,Hf,Nb)–B	1996
Ni–(Zr,Hf,Nb)–(Cr,Mo)–B	1996
Fe–Co–Ln–B	1998
Fe–(Nb,Cr,Mo)–(P,C,B)	1999
Ni–(Nb,Cr,Mo)–(P,B)	1999

Table 2.2 The classification of amorphous systems [48].

(I) ETM (or Ln) + Al + LTM	Zr-Al-Ni, Zr-Al-Cu, Zr-Al-Ni-Cu, Zr-Ti-Al-Ni-Cu, Zr-Nb-Al-Ni-Ln, and Zr-Ga-Ni
	Ln-Al-Ni, Ln-Al-Cu, Ln-Al-Ni-Cu, Ln-Ga-Ni and Ln-Ga-Cu
(II) LTM + ETM + Metalloid	Fe-Zr-B, Fe-Hf-B, Fe-Zr-Hf-B, Fe-Co-Ln-B, Fe-Co-Ln-B and Co-Zr-Nb-B
(III) LTM (Fe) + Al or Ga + Metalloid	Fe-(Al, Ga)-Metalloid
Mg + Ln + LTM	Mg-Ln-Ni and Mg-Ln-Cu
(IV)	
ETM (Zr or Ti) + Be + LTM	Zr-Ti-Be-Ni-Cu
(V) LTM + Metalloid	Pd-Ni-P, Pd-Cu-Ni-P and Pt-Ni-P

Ln = lanthanide metal

ETM = IV ~ VI group transition metal

LTM = VII ~ VIII group transition metal

Table 2.3 Summary of $\Delta T_x (=T_x - T_g)$, $T_{rg} (=T_g/T_l)$, $\gamma (=T_x / (T_g + T_l))$, critical cooling rate R_c and critical section thickness Z_c for typical bulk metallic glasses [60].

Alloy	$T_x - T_g$	T_g / T_l	$T_x / (T_g + T_l)$	R_c (K/s)	Z_c (mm)
Mg ₈₀ Ni ₁₀ Nd ₁₀	16.3	0.517	0.353	1251.4 [26]	0.6 [26]
Mg ₇₅ Ni ₁₅ Nd ₁₀	20.4	0.570	0.379	46.1 [26]	2.8 [26]
Mg ₇₀ Ni ₁₅ Nd ₁₅	22.3	0.553	0.373	178.2 [26]	1.5 [26]
Mg ₆₅ Ni ₂₀ Nd ₁₅	42.1	0.571	0.397	30.0 [27]	3.5 [26]
Mg ₆₅ Cu ₂₅ Y ₁₀	54.9	0.551	0.401	50.0 [28]	7.0 [29]
Zr ₆₆ Al ₈ Ni ₂₆	35.6	0.537	0.368	66.6 [30]	
Zr ₆₆ Al ₈ Cu ₇ Ni ₁₉	58.4	0.552	0.387	22.7 [30]	
Zr ₆₆ Al ₈ Cu ₁₂ Ni ₁₄	77.4	0.559	0.401	9.8 [30]	
Zr ₆₆ Al ₉ Cu ₁₆ Ni ₉	79.5	0.561	0.403	4.1 [30]	
Zr ₆₅ Al _{7.5} Cu _{17.5} Ni ₁₀	79.1	0.562	0.403	1.5 [32]	16.0 [32]
Zr ₅₇ Ti ₅ Al ₁₀ Cu ₂₀ Ni ₈	43.3	0.591	0.395	10.0 [33]	10.0 [34]
Zr _{38.5} Ti _{16.5} Ni _{9.75} Cu _{15.25} Be ₂₀	48.0	0.628	0.415	1.4 [4]	
Zr _{39.88} Ti _{15.12} Ni _{9.98} Cu _{13.77} Be _{21.25}	57.0	0.625	0.420	1.4 [4]	
Zr _{41.2} Ti _{13.8} Cu _{12.5} Ni ₁₀ Be _{22.5}	49.0	0.626	0.415	1.4 [4]	50.0 [35]
Zr _{42.63} Ti _{12.37} Cu _{11.25} Ni ₁₀ Be _{23.75}	89.0	0.589	0.424	5.0 [4]	
Zr ₄₄ Ti ₁₁ Cu ₁₀ Ni ₁₀ Be ₂₅	114.0	0.518	0.404	12.5 [4]	
Zr _{45.38} Ti _{9.62} Cu _{8.75} Ni ₁₀ Be _{26.25}	117.0	0.503	0.397	17.5 [4]	
Zr _{46.25} Ti _{8.25} Cu _{7.5} Ni ₁₀ Be _{27.5}	105.0	0.525	0.402	28.0 [4]	
La ₅₅ Al ₂₅ Ni ₂₀	64.3	0.521	0.388	67.5 [36,37]	3.0 [38]
La ₅₅ Al ₂₅ Ni ₁₅ Cu ₅	67.6	0.526	0.394	34.5 [36]	
La ₅₅ Al ₂₅ Ni ₁₀ Cu ₁₀	79.8	0.560	0.420	22.5 [36]	5.0 [38]
La ₅₅ Al ₂₅ Ni ₅ Cu ₁₅	60.9	0.523	0.389	35.9 [36]	
La ₅₅ Al ₂₅ Cu ₂₀	38.9	0.509	0.366	72.3 [36]	3.0 [38]
La ₅₅ Al ₂₅ Ni ₅ Cu ₁₀ Co ₅	76.6	0.566	0.421	18.8 [36]	9.0 [38]
La ₆₆ Al ₁₄ Cu ₂₀	54.0	0.540	0.399	37.5 [18]	2.0 [18]
Pd ₄₀ Cu ₃₀ Ni ₁₀ P ₂₀	78.9	0.690	0.464	0.1 [39]	72.0 [39]
Pd _{81.5} Cu ₂ Si _{16.5}	37.0	0.577	0.387		2.0 [40,41]
Pd _{79.5} Cu ₄ Si _{16.5}	40.0	0.585	0.392	500.0 [42]	0.75 [43]
Pd _{77.5} Cu ₆ Si _{16.5}	41.0	0.602	0.400	100.0 [43]	1.5 [44]
Pd ₇₇ Cu ₆ Si ₁₇	44.0	0.569	0.388	125.0 [45]	2.0 [40,41]
Pd _{73.5} Cu ₁₀ Si _{16.5}	40.0	0.568	0.385		2.0 [40,41]
Pd _{71.5} Cu ₁₂ Si _{16.5}	28.0	0.565	0.377		2.0 [40,41]
Pd ₄₀ Ni ₄₀ P ₂₀	63.0	0.585	0.409	0.167 [31]	25.0 [42]
Nd ₆₀ Al ₁₅ Ni ₁₀ Cu ₁₀ Fe ₅	45.0	0.552	0.393		5.0 [46]
Nd ₆₁ Al ₁₁ Ni ₈ Co ₅ Cu ₁₅	24.0	0.598	0.394		6.0 [46]
Cu ₆₀ Zr ₃₀ Ti ₁₀	50.0	0.619	0.409		4.0 [5]
Cu ₅₄ Zr ₂₇ Ti ₉ Be ₁₀	42.0	0.637	0.412		5.0 [19]
Ti ₃₄ Zr ₁₁ Cu ₄₇ Ni ₈	28.8	0.597	0.389	100 [35]	4.5 [35,47]
Ti ₅₀ Ni ₂₄ Cu ₂₀ B ₁ Si ₂ Sn ₃	74.0	0.554	0.393		1.0 [20]

Table 3.1 The constituent contents of alloy systems in this study.

Mg-based BMG	Mg		Cu		Gd					
	at%	wt%	at%	wt%	at%	wt%				
Mg ₆₅ Cu ₂₅ Gd ₁₀	65	33.3	25	33.5	10	33.2				
Zr-based BMG	Zr		Ni		Cu		Al			
	at%	wt%	at%	wt%	at%	wt%	at%	wt%		
Zr _{63.8} Ni _{16.2} Cu ₁₅ Al ₅	63.8	74.1	16.2	12.1	15	12.1	5	1.7		
Au-based BMG	Au		Ag		Pd		Cu		Si	
	at%	wt%	at%	wt%	at%	wt%	at%	wt%	at%	wt%
Au ₄₉ Ag _{5.5} Pd _{2.3} Cu _{26.9} Si _{16.3}	49	76.2	5.5	4.6	2.3	1.9	26.9	13.5	16.3	3.6

Table 3.2 Nanoscratch testing condition

Scratch length	500 μm
Scratch velocity	10 $\mu\text{m/s}$
Starting scratch load	0.1 mN
Maximum scratch load	30 mN
Cross profile location (input scratch load)	15 mN
Load applied during profiling	100 μN

Table 4.1 The composition analyses of the $\text{Mg}_{65}\text{Cu}_{25}\text{Gd}_{10}$, $\text{Zr}_{63.8}\text{Ni}_{16.2}\text{Cu}_{15}\text{Al}_5$ and $\text{Au}_{49}\text{Ag}_{5.5}\text{Pd}_{2.3}\text{Cu}_{26.9}\text{Si}_{16.3}$ amorphous alloys by SEM/EDS.

Alloys	Elements	Ideal (at%)	SEM/EDS (at%)
$\text{Mg}_{65}\text{Cu}_{25}\text{Gd}_{10}$	Mg	65	64.3
	Cu	25	24.3
	Gd	10	11.4
$\text{Zr}_{63.8}\text{Ni}_{16.2}\text{Cu}_{15}\text{Al}_5$	Zr	63.8	65.1
	Ni	16.2	15.8
	Cu	15	14.2
	Al	5	4.9
$\text{Au}_{49}\text{Ag}_{5.5}\text{Pd}_{2.3}\text{Cu}_{26.9}\text{Si}_{16.3}$	Au	49	54.5
	Ag	5.5	5.4
	Pd	2.3	2.1
	Cu	26.9	24
	Si	16.3	14

Table 4.2 Thermal properties of the $Mg_{65}Cu_{25}Gd_{10}$, $Zr_{63.8}Ni_{16.2}Cu_{15}Al_5$ and $Au_{49}Ag_{5.5}Pd_{2.3}Cu_{26.9}Si_{16.3}$ amorphous alloys obtained from DSC.

Alloys	Heating rate (K/min)	T_g (K)	T_x (K)	ΔT_x (K)	T_m (K)	T_l (K)	T_{rg}	γ	γ_m
Mg-based BMG	40	421	490	69	684	738	0.570	0.423	0.757
Zr-based BMG	40	647	745	98	1114	1178	0.549	0.408	0.716
Au-based BMG	40	400	450	50	625	646	0.619	0.430	0.774

Table 4.3 Summary of the compressive stress/elastic modulus of Mg₆₅Cu₂₅Gd₁₀ (in at%) glass at different strain rates.

Sample size (Mg-based BMG)	$\dot{\epsilon} \sim 1 \times 10^{-4} \text{ s}^{-1}$	$\dot{\epsilon} \sim 1 \times 10^{-3} \text{ s}^{-1}$	$\dot{\epsilon} \sim 1 \times 10^{-2} \text{ s}^{-1}$
Bulk 3 mm	800 MPa / 50 GPa	--	--
3.8 μm	1342 MPa / 44 GPa	1362 MPa / 51 GPa	1384 MPa / 43 GPa
1 μm	1400 MPa / 51 GPa	1488 MPa / 46 GPa	1580 MPa / 56 GPa

Table 4.4 Summary of the compressive stress/elastic modulus of $Zr_{63.8}Ni_{16.2}Cu_{15}Al_5$ (in at%) glass at different strain rates.

Sample size (Zr-based BMG)	$\dot{\epsilon} \sim 1 \times 10^{-4} \text{ s}^{-1}$	$\dot{\epsilon} \sim 1 \times 10^{-3} \text{ s}^{-1}$	$\dot{\epsilon} \sim 1 \times 10^{-2} \text{ s}^{-1}$
Bulk 2 mm	1600 MPa / 80-90 GPa	1712 MPa / --	1847 MPa / --
3.8 μm	2088 MPa / 77 GPa	1992 MPa / 80 GPa	2054 MPa / 79 GPa
1 μm	2496 MPa / 63 GPa	2357 MPa / 81 GPa	2365 MPa / 85 GPa
700 nm	2972 MPa / 81 GPa	2590 MPa / 88 GPa	2733 MPa / 72 GPa

Table 4.5 Summary of the flow stress and deformation mode of the 1 μm Au-based BMG pillar samples at different temperatures with strain rate of $1 \times 10^{-2} \text{ s}^{-1}$.

Temperature (K)	300	343	373	383	393	403	408
Flow stress (GPa)	1.94	1.92	2.15	1.64	1.74	0.55	0.6
Deformation Mode	Inhomo	Inhomo	Inhomo	Inhomo	Inhomo	Homo	Homo

Table 4.6 Testing conditions for the different pillar samples.

Pillar	H (μm)	Temperature (K)	Nominal strain rate (s^{-1})
P-1	8.762	395.9	10^{-3}
P-2	8.849	395.9	10^{-3} to 5×10^{-3}
P-3	8.885	395.9	3×10^{-3} to 8×10^{-3} to 5×10^{-4}
P-4	9.01	401.2	10^{-3} to 10^{-2} to 5×10^{-3}

Table 4.7 Pillar sample height change and thermal drift in microcompression tests.

Pillar	H_1 (μm)	H_2 (μm)	ΔH (μm)	ΔL (μm)	t (sec)	$(\Delta H - \Delta L)/t$ (nm/s)	Drift rate (nm/s)
P-1	8.762	7.936	0.826	0.737	114	0.78	0.82
P-2	8.849	7.789	1.06	1.045	97	0.15	0.22
P-3	8.885	7.633	1.252	1.212	97	0.41	0.56
P-4	9.01	7.812	1.198	1.126	79	0.91	0.76

Table 4.8 Summary of the data measured using MTS NanoIndenter XP system.

BMG	Elastic modulus (GPa)	Hardness (GPa)	Wear coefficient	Wear resistance (10^{11} Pa)
Mg-based BMG	69.1±2.8	3.7±0.36	4.136 x 10 ⁻²	0.97
Au-based BMG	91.7±2.4	4.1±0.24	1.396 x 10 ⁻²	2.17
Zr-based BMG	90.3±0.6	5.2±0.04	1.156 x 10 ⁻²	4.17

Table 5.1 Summary of data measured using microcompression tests and nanoscratch tests.

BMG	Strain rate (s ⁻¹)	Strain burst speed (nm/s)		Wear resistance (10 ¹¹ Pa)
		1 μm	3.8 μm	
Mg-based BMG	1x10 ⁻⁴	747	9178	0.97
	1x10 ⁻³	792	10031	
	1x10 ⁻²	1551	10619	
Zr-based BMG	1x10 ⁻⁴	263~282	997~3292	4.17
	1x10 ⁻³	110~469	818~2809	
	1x10 ⁻²	231~433	933~4000	

Table 5.2 Fitted parameters in Eq. (5-1) from the results of microcompression of the 3.8 μm Au-based BMG pillar samples.

T (K)	$\dot{\epsilon}_T$ (s^{-1})	V (\AA^3)	v_0 (\AA^3)
395.9	0.0026 ± 0.0001	55 ± 2	440 ± 15
401.2	0.0027 ± 0.0001	62 ± 2	496 ± 15

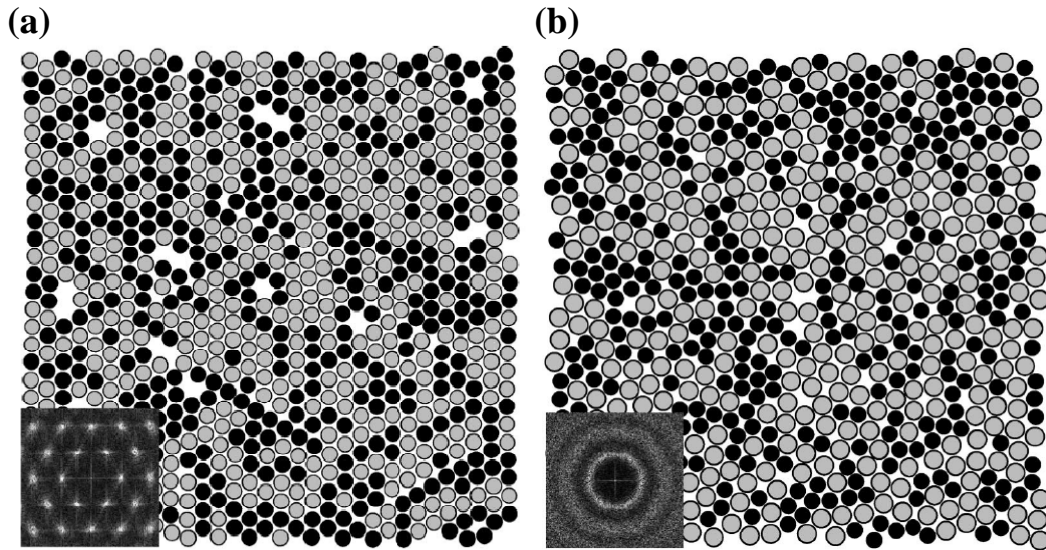


Figure 1.1 Schematic illustrations showing atomic structures of (a) crystalline materials and (b) amorphous alloys. The inset in the lower left corner shows a diffraction pattern [1].

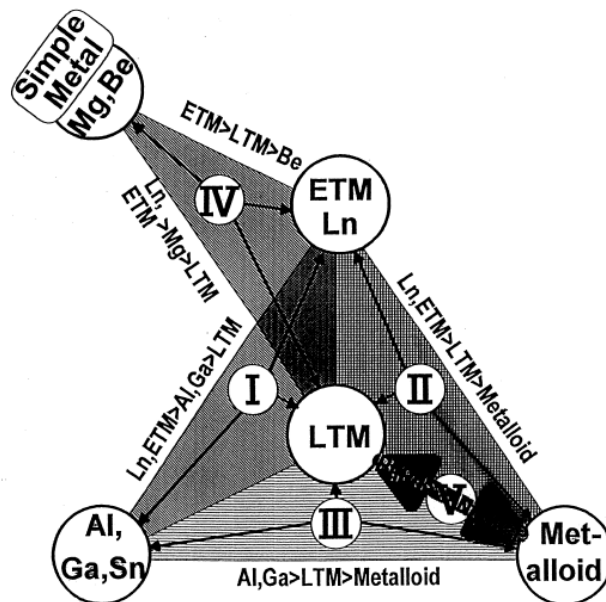


Figure 2.1 The classification of amorphous alloy system [48] (ETM = IV ~ VI group transition metal; LTM = VII ~ VIII group transition metal).

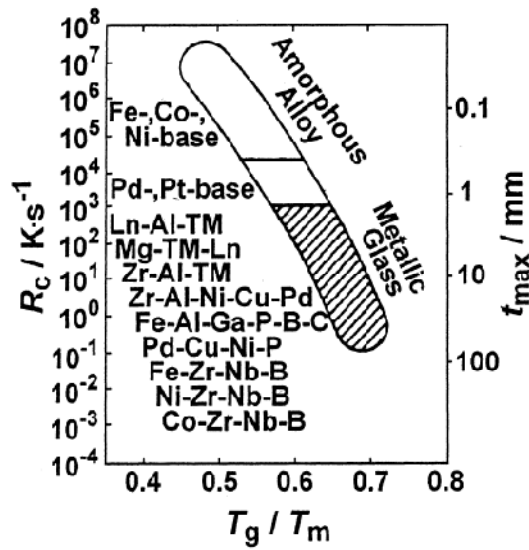


Figure 2.2 Relationship between the critical cooling rate (R_c), maximum sample thickness (t_{\max}) and reduced glass transition temperature (T_g/T_m) for bulk amorphous alloy systems [48].

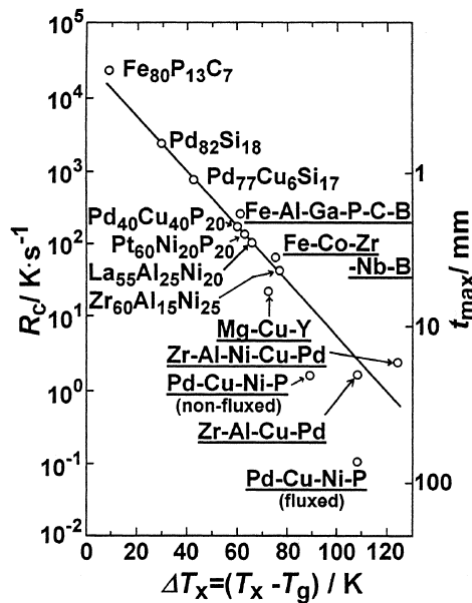


Figure 2.3 Relationship between the critical cooling rate (R_c), maximum sample thickness (t_{\max}) and supercooled liquid range $\Delta T_x (= T_x - T_g)$ for bulk amorphous alloys [48].

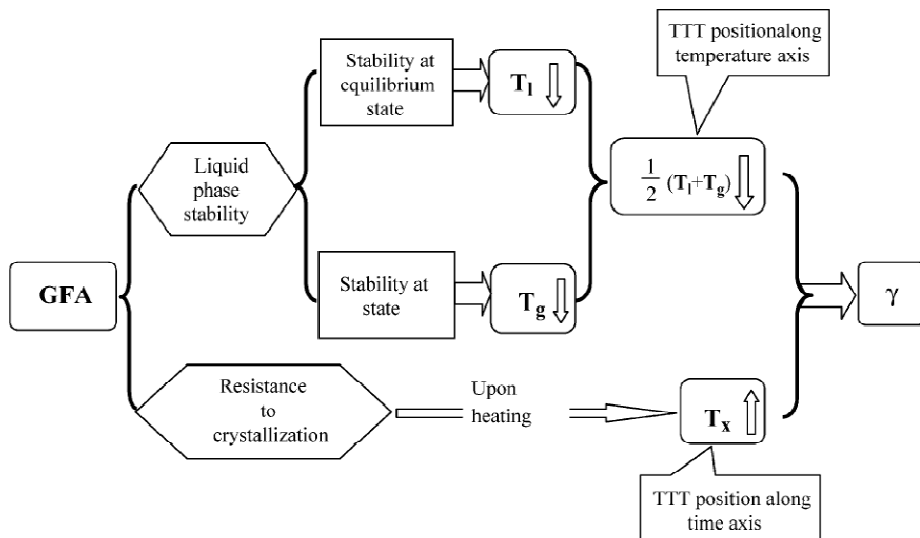


Figure 2.4 New parameter γ for understanding GFA of metallic glasses [61].

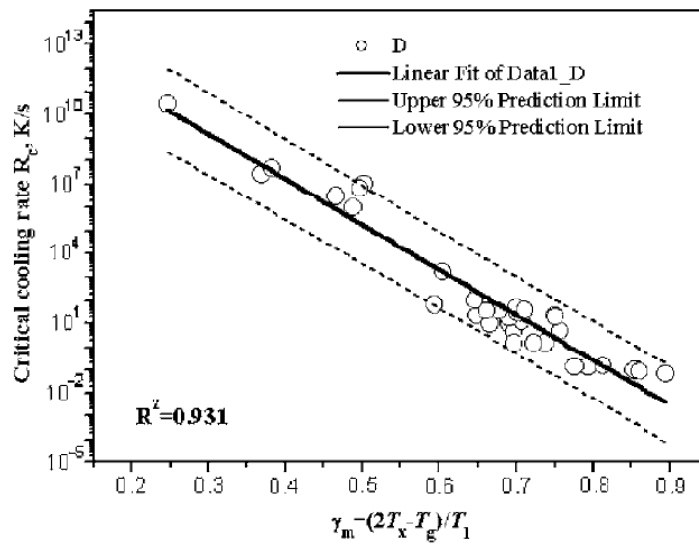


Figure 2.5 The correlation between the R_c and γ_m for metallic glasses. Data were taken from the study of Lu et al. [62].

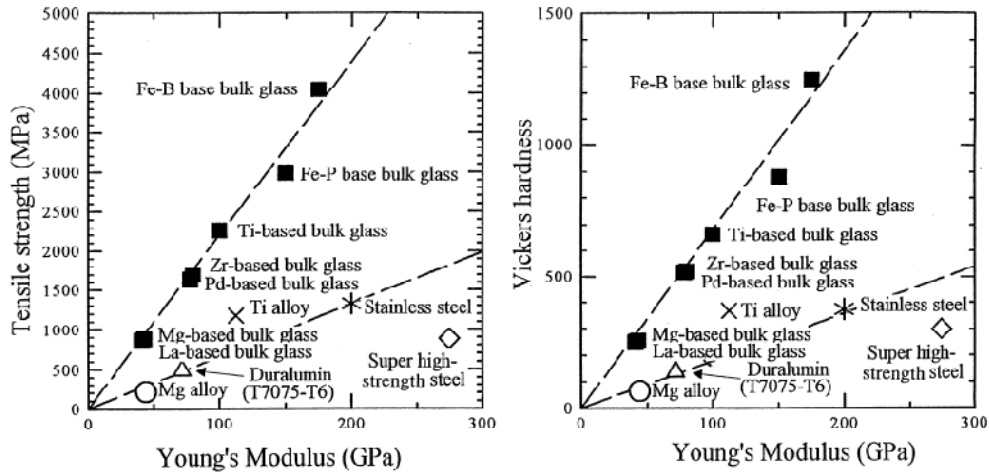


Figure 2.7 The relationship between the tensile strength, Vickers hardness and Young's modulus for various bulk metallic glasses [48].

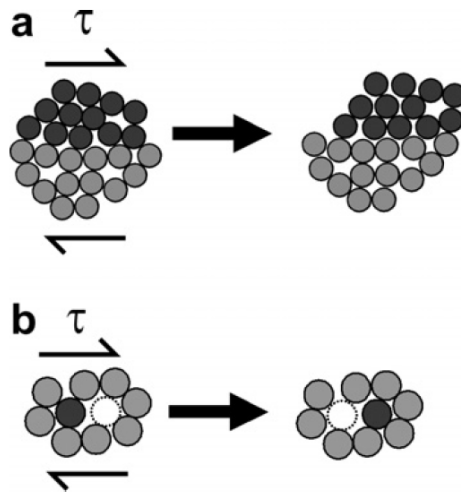


Figure 2.8 Two-dimensional schematics of the atomistic deformation mechanisms in the amorphous alloys, including (a) a shear transformation zone (STZ) and (b) a local atomic jump [33].

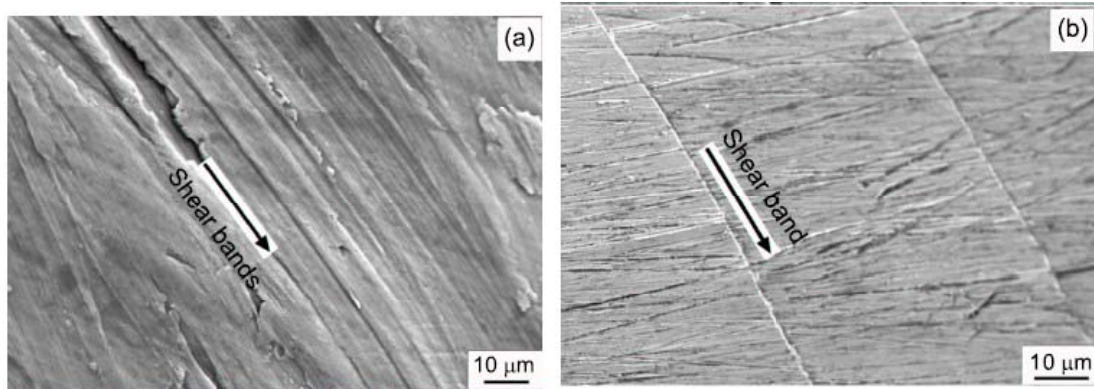


Figure 2.9 SEM micrograph of the sample surface for the $Zr_{59}Cu_{20}Al_{10}Ni_8Ti_3$ amorphous alloy under (a) compressive loading and (b) tensile loading [82].

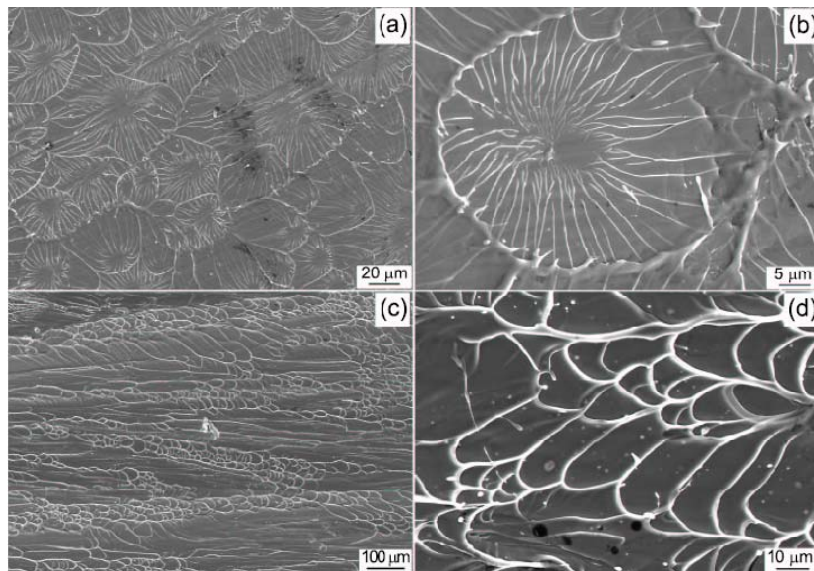


Figure 2.10 SEM micrograph of typical shear fracture surfaces for the $Zr_{52.5}Ni_{14.6}Al_{10}Cu_{17.9}Ti_5$ amorphous alloy under tensile loading (a)-(b); under compressive loading (c)-(d) [82].

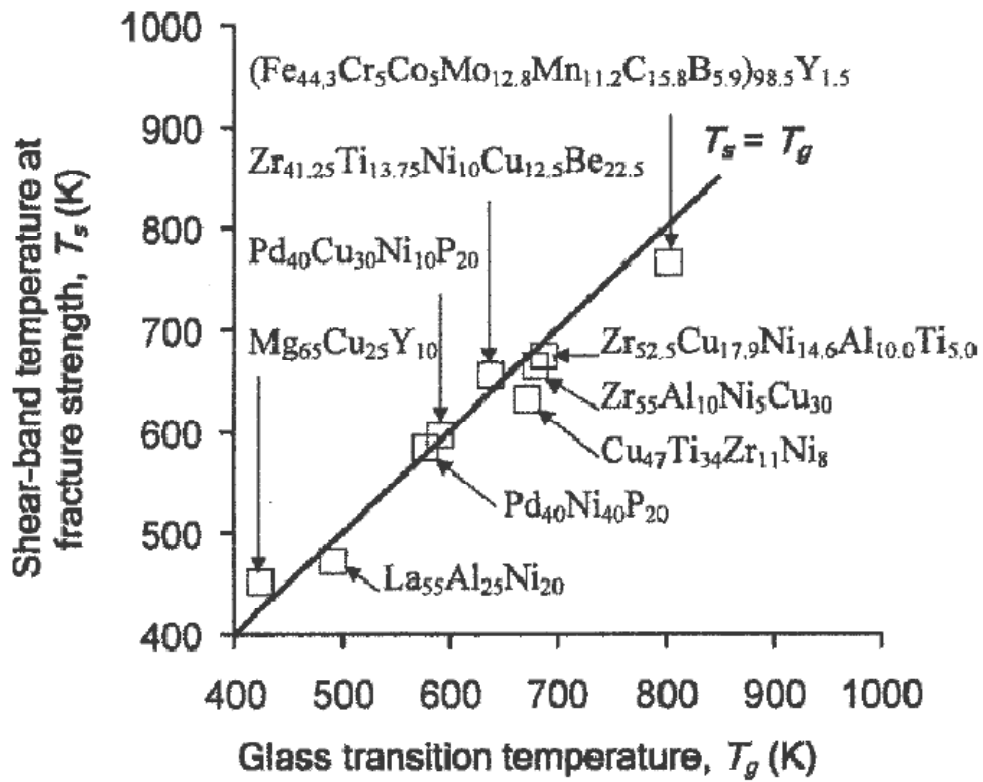


Figure 2.11 Comparison between the glass transition temperature and calculated shear band temperature at fracture strength for different BMGs [93].

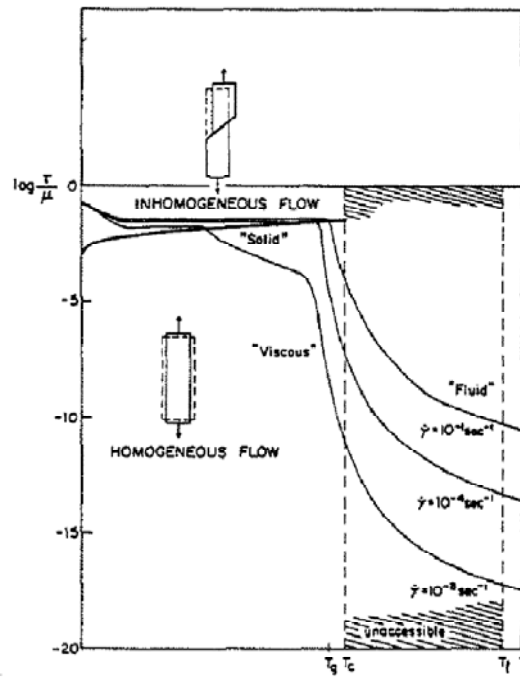


Figure 2.12 Deformation map of a typical amorphous alloy [31].

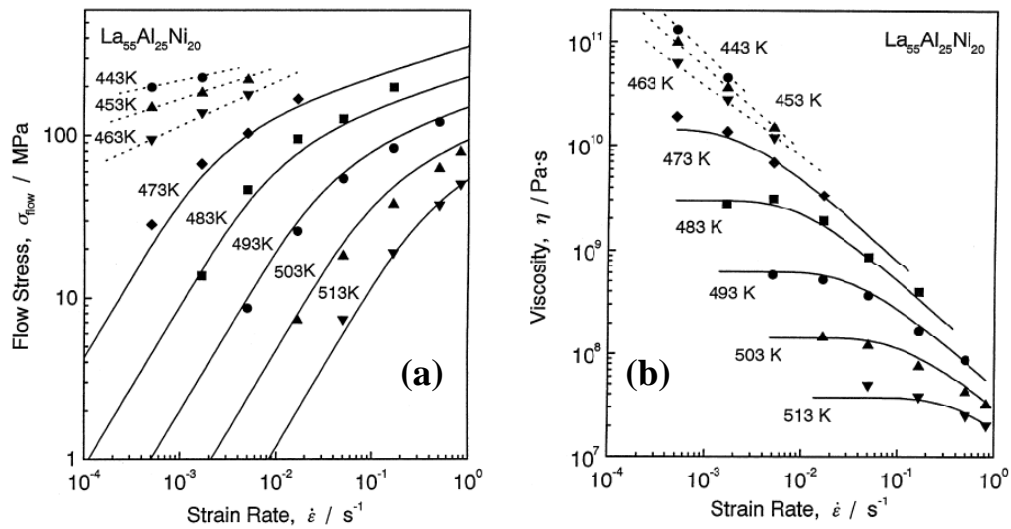


Figure 2.13 Strain-rate dependence of the flow stress (σ_{flow}) and viscosity (η) for the homogeneous deformation in the $\text{La}_{55}\text{Al}_{25}\text{Ni}_{20}$ amorphous alloy [101].

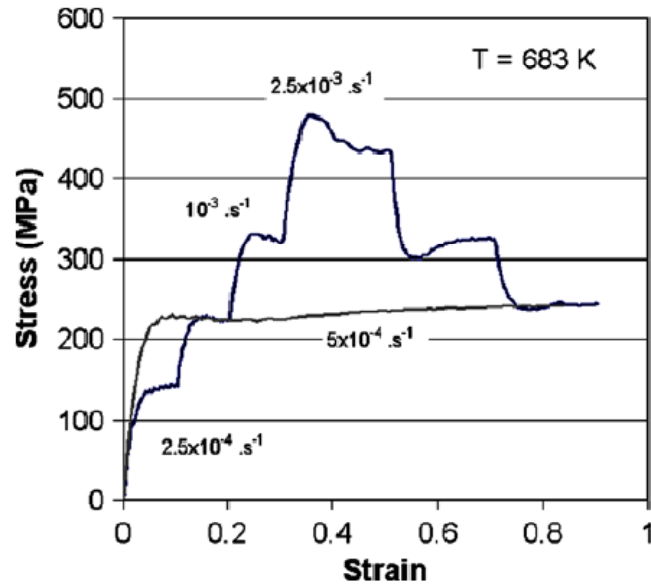


Figure 2.14 Strain-stress curves of a $Zr_{52.5}Al_{10}Cu_{22}Ti_{2.5}Ni_{13}$ amorphous alloy at temperature of 683 K in strain rate change and constant strain rate tests [107].

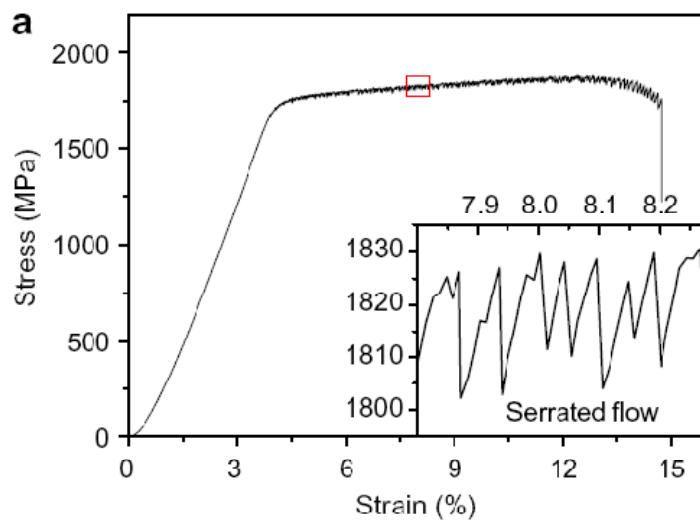


Figure 2.15 Serrated flow on stress-strain curve of the $Ni_{50}Pd_{30}P_{20}$ BMG [108].

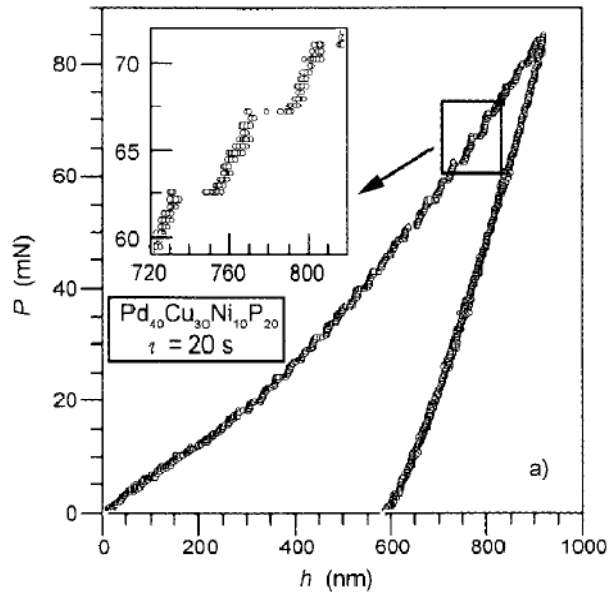


Figure 2.16 The typical p-h curve of the Pd₄₀Cu₃₀Ni₁₀P₂₀ amorphous alloy [111].

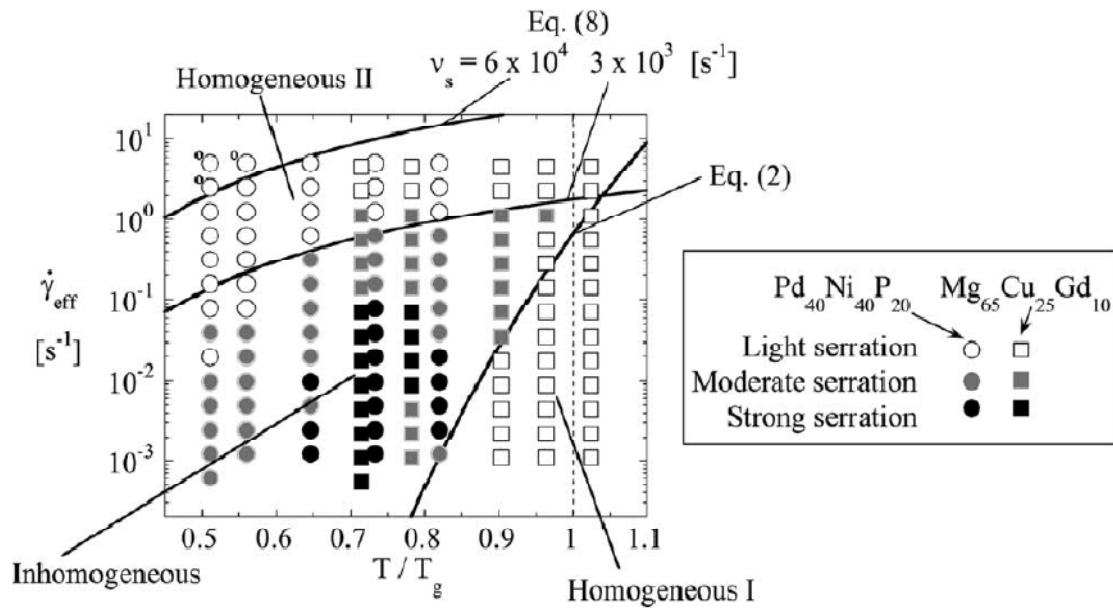


Figure 2.17 Deformation map of the Pd₄₀Ni₄₀P₂₀ and Mg₆₅Cu₂₅Gd₁₀ amorphous alloys [118].

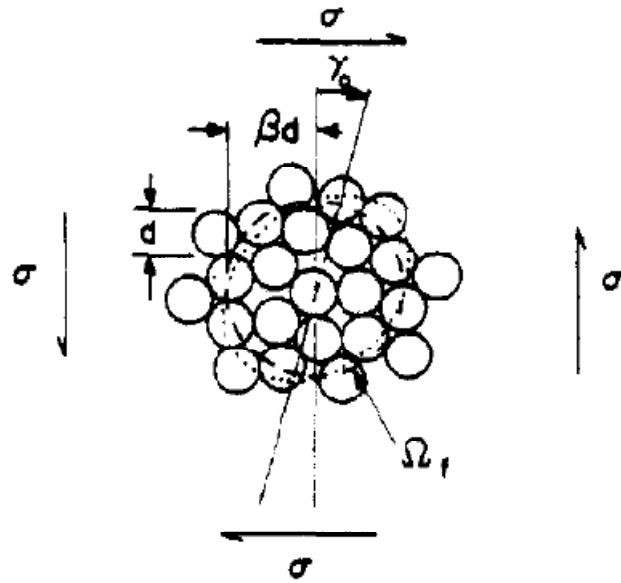


Figure 2.18 A diffuse shear transformation inside a spherical volume element, Ω_f , is favored at high temperatures [32].

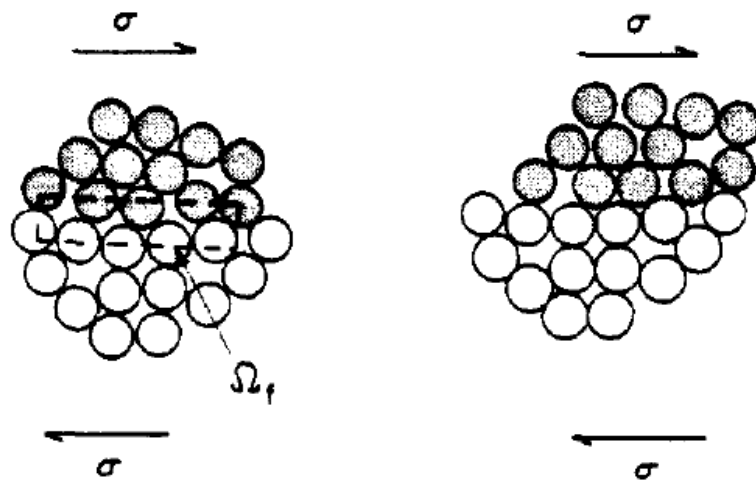


Figure 2.19 A more intense shear transformation inside a disk shaped volume element, Ω_f , is favored at low temperatures [32].

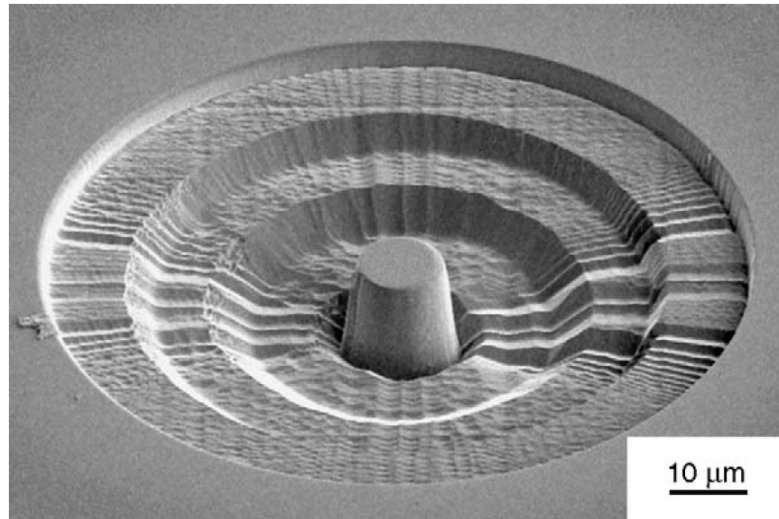


Figure 2.20 Annular milling patterns have been used to mill a roughly defined micropillar sample of Ni single crystal [131].

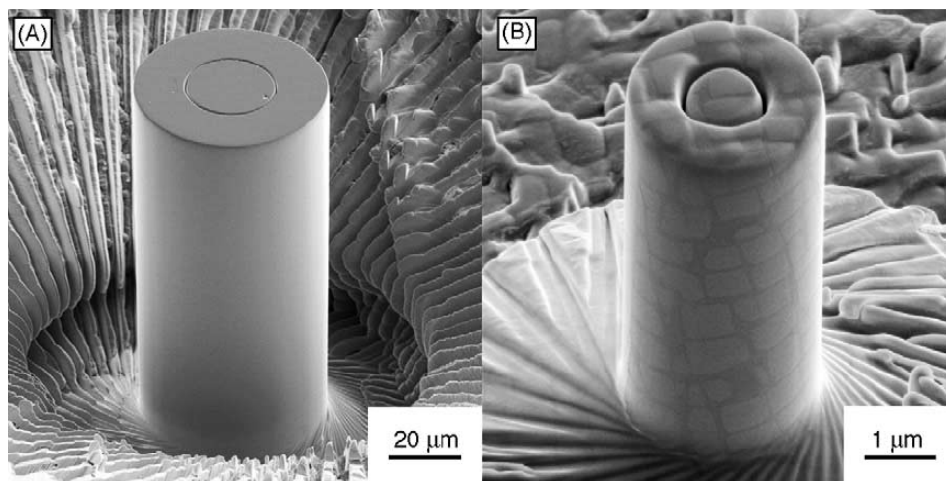


Figure 2.21 The microcompression samples were fabricated into (A) a Ni_3Al alloy and (B) Ni-based superalloy by using lathe milling program [131]. The diameter of microcompression samples are 43 μm and 2.3 μm, respectively.

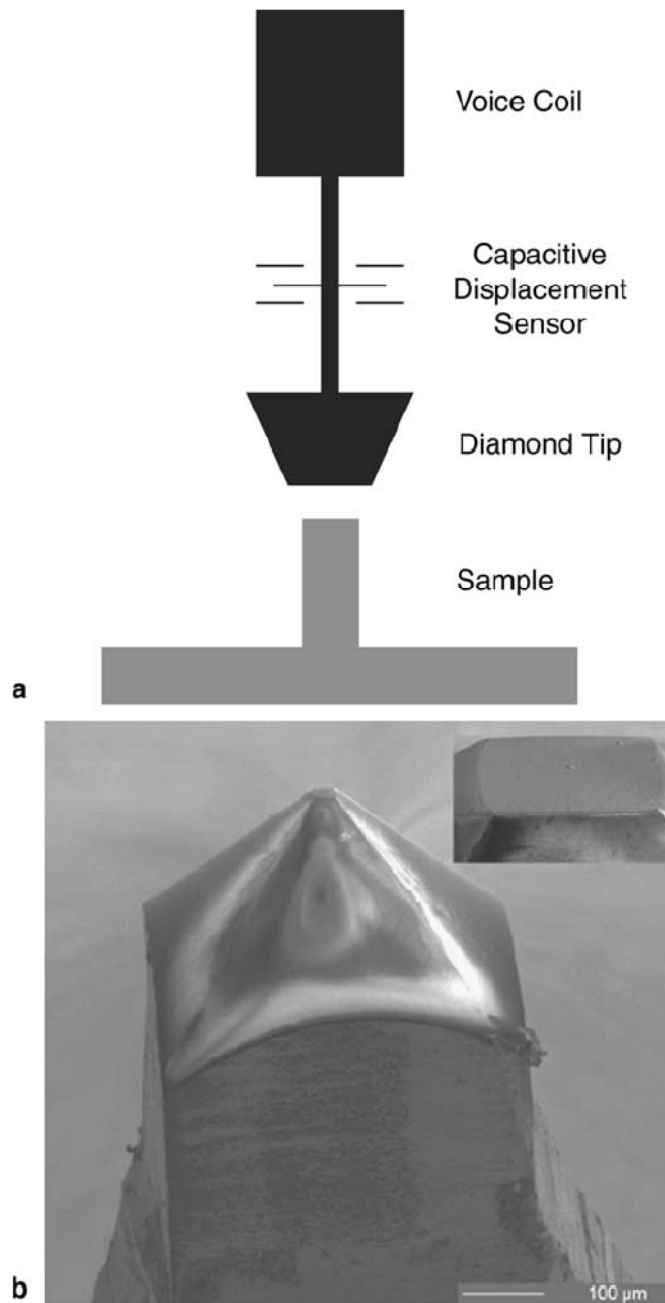


Figure 2.22 (a) Schematic of the microcompression test setup; (b) A SEM micrograph with a flat diamond tip of 30 μm in size [135].

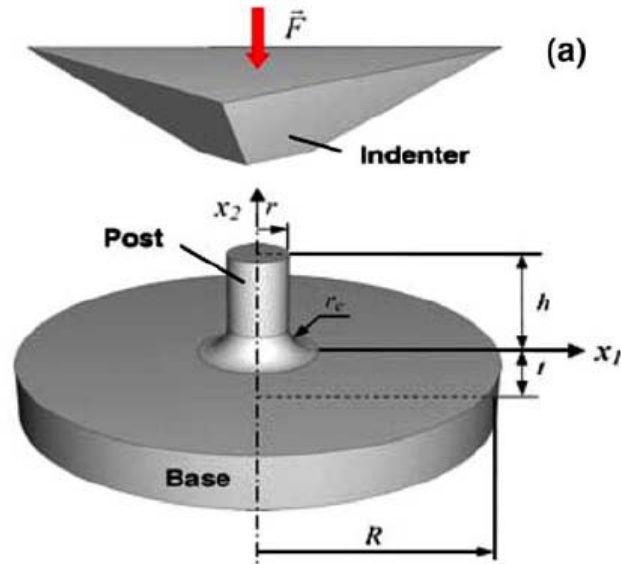


Figure 2.23 Schematic of a cylindrical pillar and its base [136].

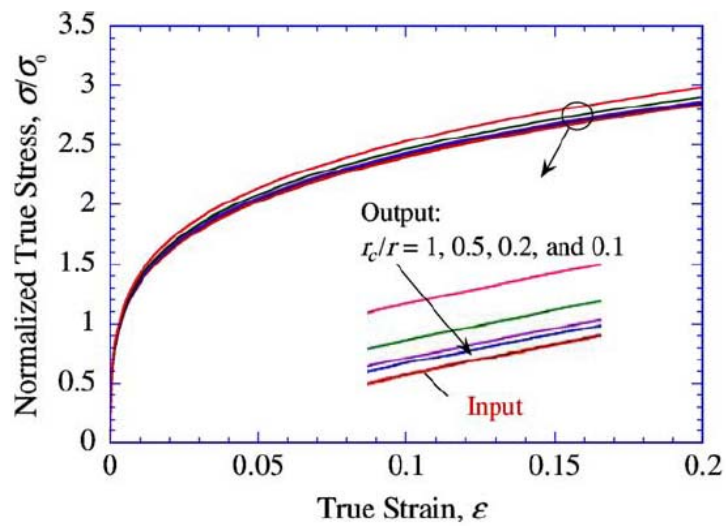


Figure 2.24 Effect of fillet radius/pillar radius ratio on numerical simulation output [136]. The inset shows an enlargement of the circled region to facilitate comparison.

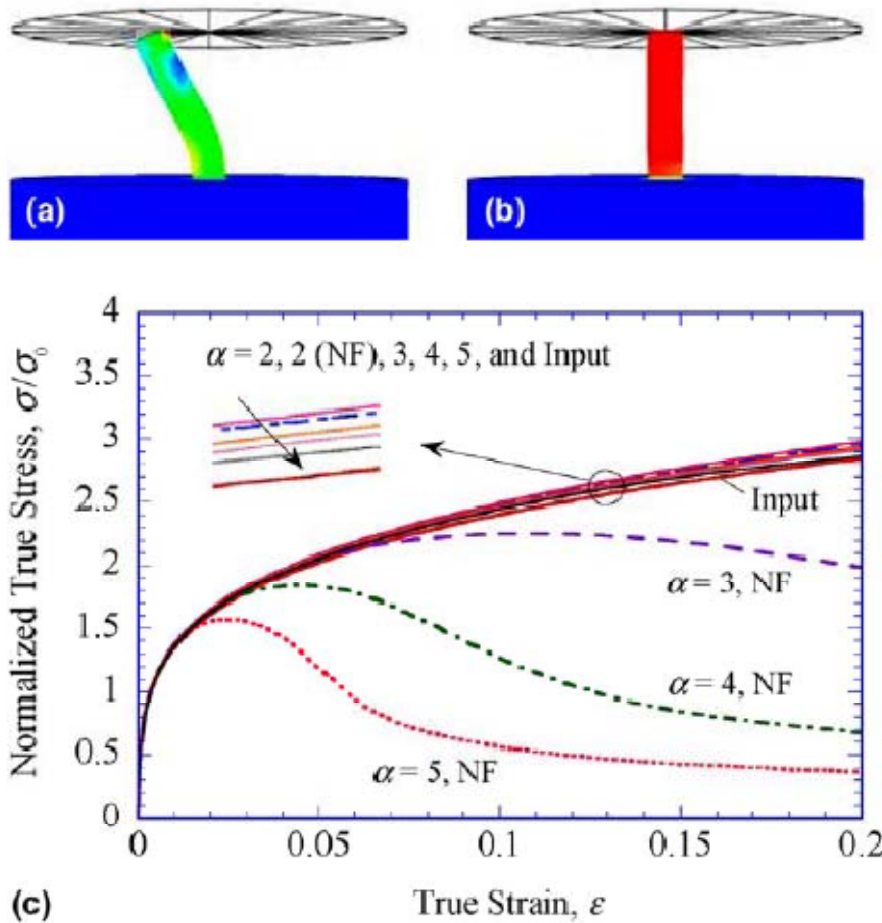


Figure 2.25 (a) Deformed configuration of a circular cylindrical pillar with an aspect ratio $\alpha = 5$ at a strain of 0.1. (b) Deformed configuration of the pillar at the same strain of 0.1, but now considering friction. (c) Input and output stress-strain curves for a pillar with an aspect ratios $\alpha = 2-5$, both with friction and without friction (NF) [136].

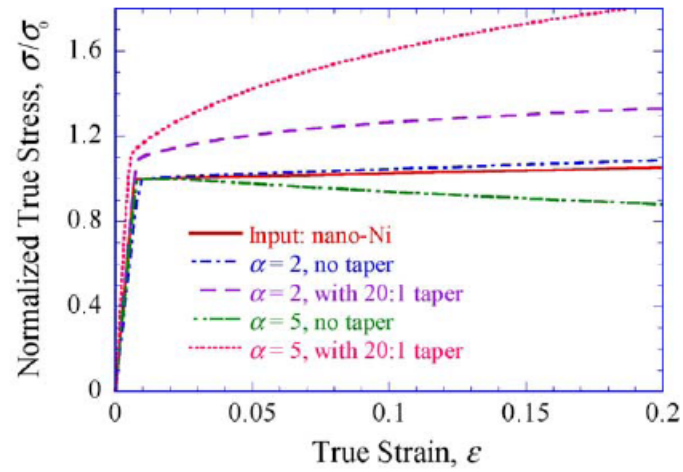


Figure 2.26 Effect of taper on numerical simulation output [136].

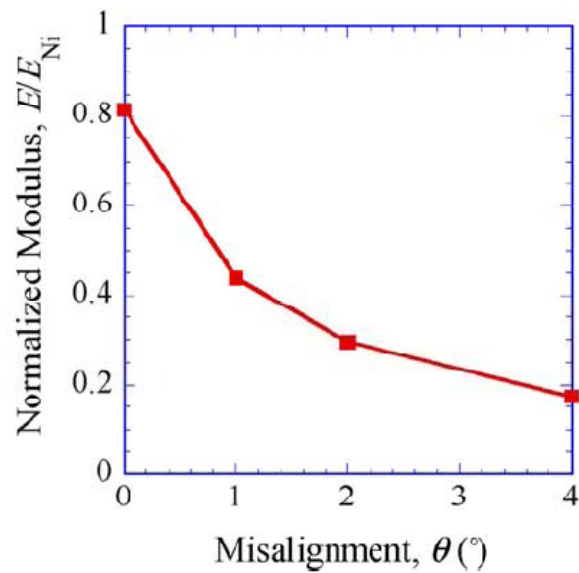


Figure 2.27 Effect of misalignment of the system on the error in elastic modulus [136].

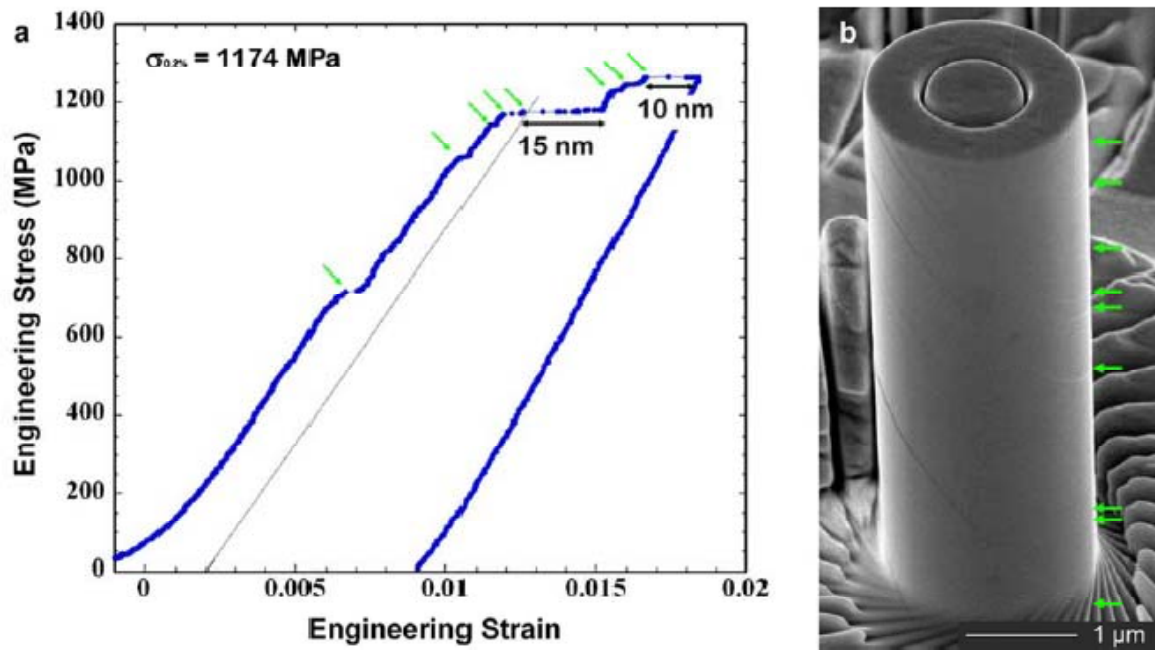


Figure 2.28 (a) The microcompressive engineering stress-strain curve of the $\text{Ni}_{76}\text{Al}_{24}$ alloy with $2\ \mu\text{m}$ diameter. (b) SEM micrograph of a micropillar after microcompression test. Strain bursts are indicated by arrows in figure (a), and appearance of slip lines are also observed on the micropillar surface, as also indicated by arrows [138].

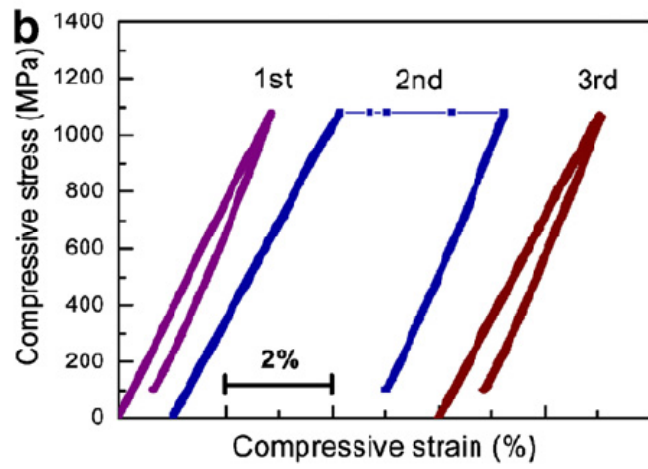


Figure 2.29 Engineering stress-strain curve obtained from the microcompression test of the 12 μm $\text{Mg}_{61}\text{Cu}_{28}\text{Gd}_{11}$ BMG [34].

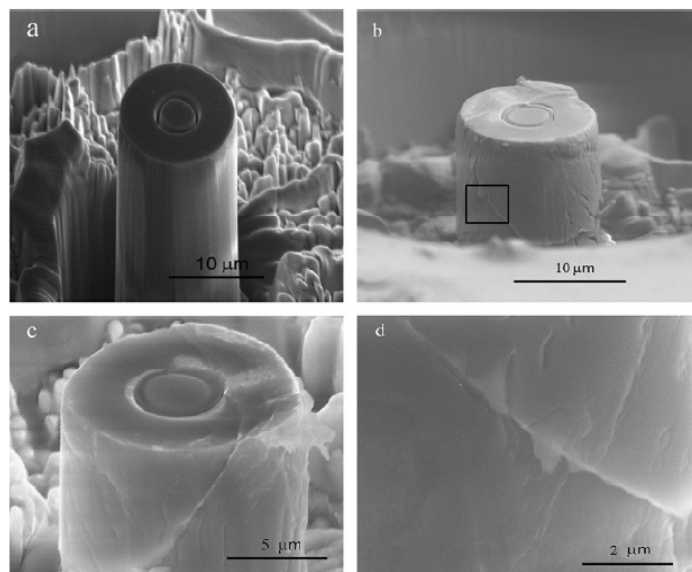


Figure 2.30 Micrographs of the micropillar, (a) before and (b) and (c) after microcompression test. (d) Close-up view showing the shear bands [34].

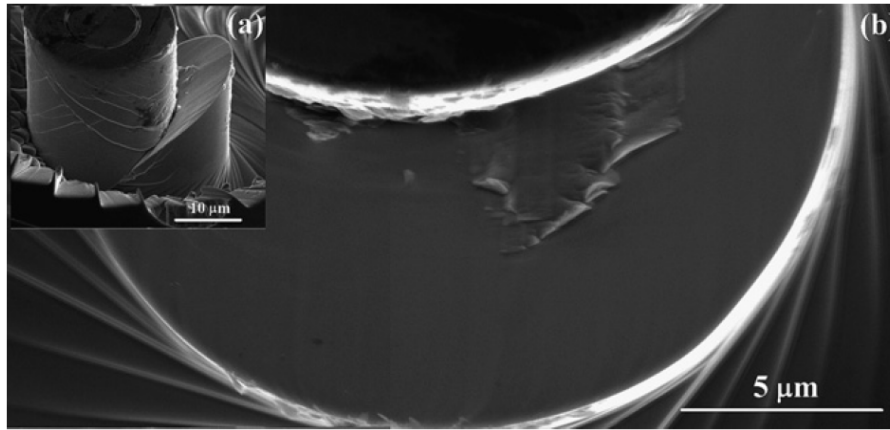


Figure 2.31 (a) An SEM micrograph of the pillar sample with the diameter of 20 μm after microcompression test, and the corresponding fracture surface as shown in (b) [141]. (No evidence of localized melting or river pattern is apparent in fracture surface.)

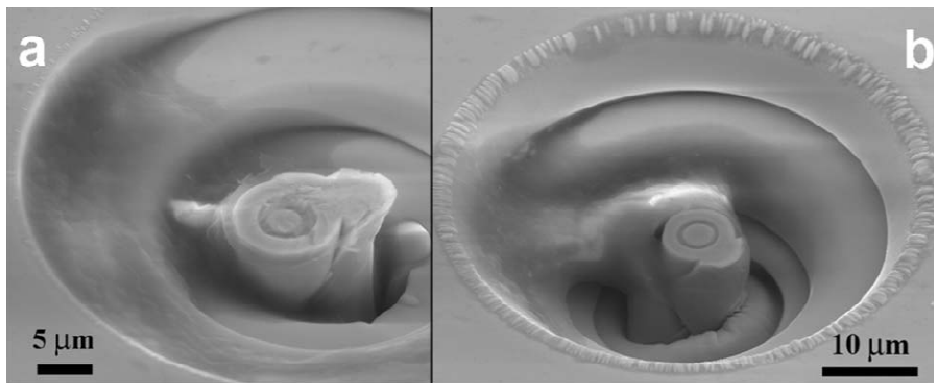


Figure 2.32 SEM micrographs of the pillar samples with diameters of (a) 10 μm and 8 μm after microcompression test [142]. (Global melting is observed in micropillar samples under microcompression test.)

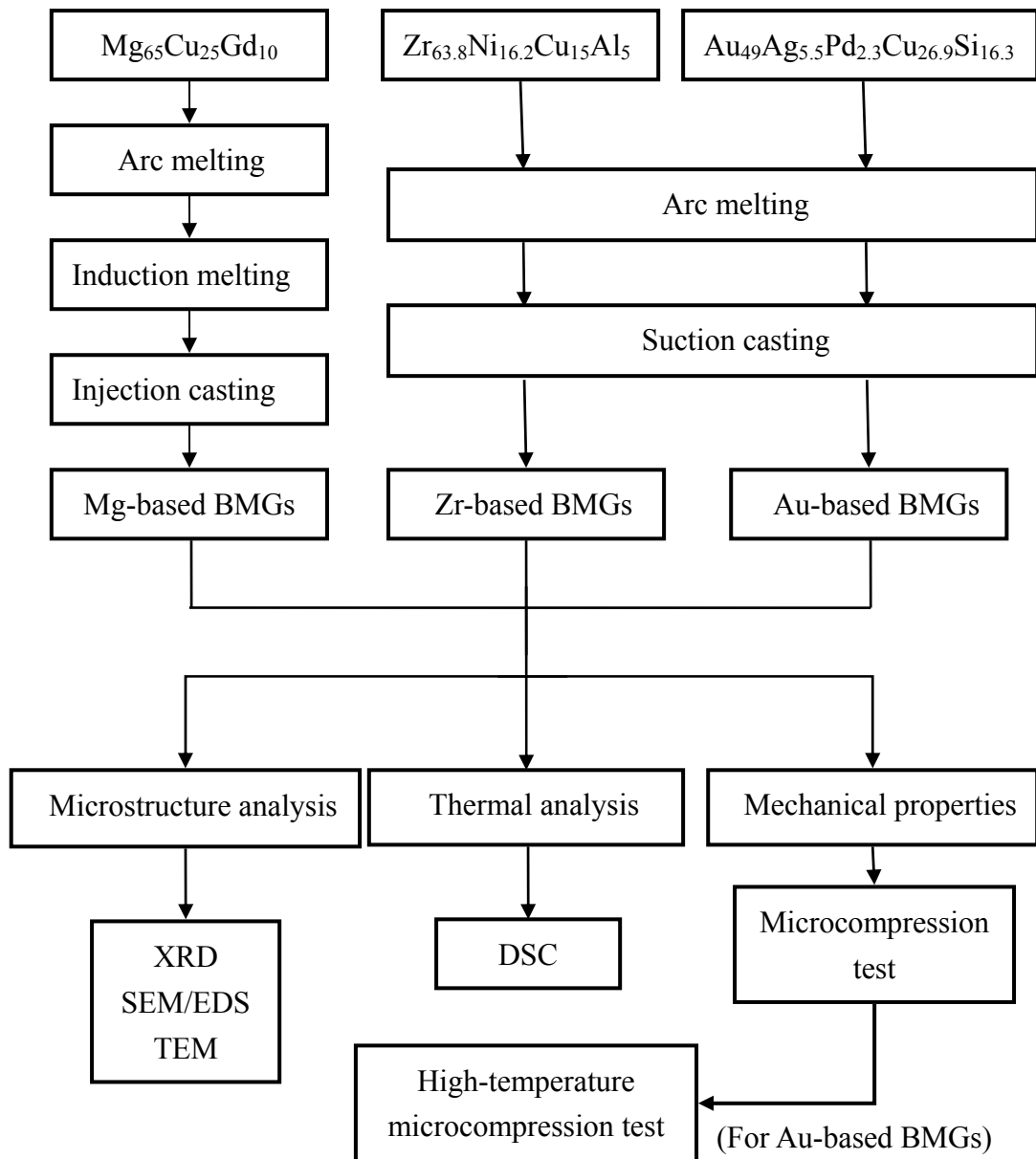


Figure 3.1 The flow chart of the experimental procedures.



Figure 3.2 Photograph of the arc melting device.

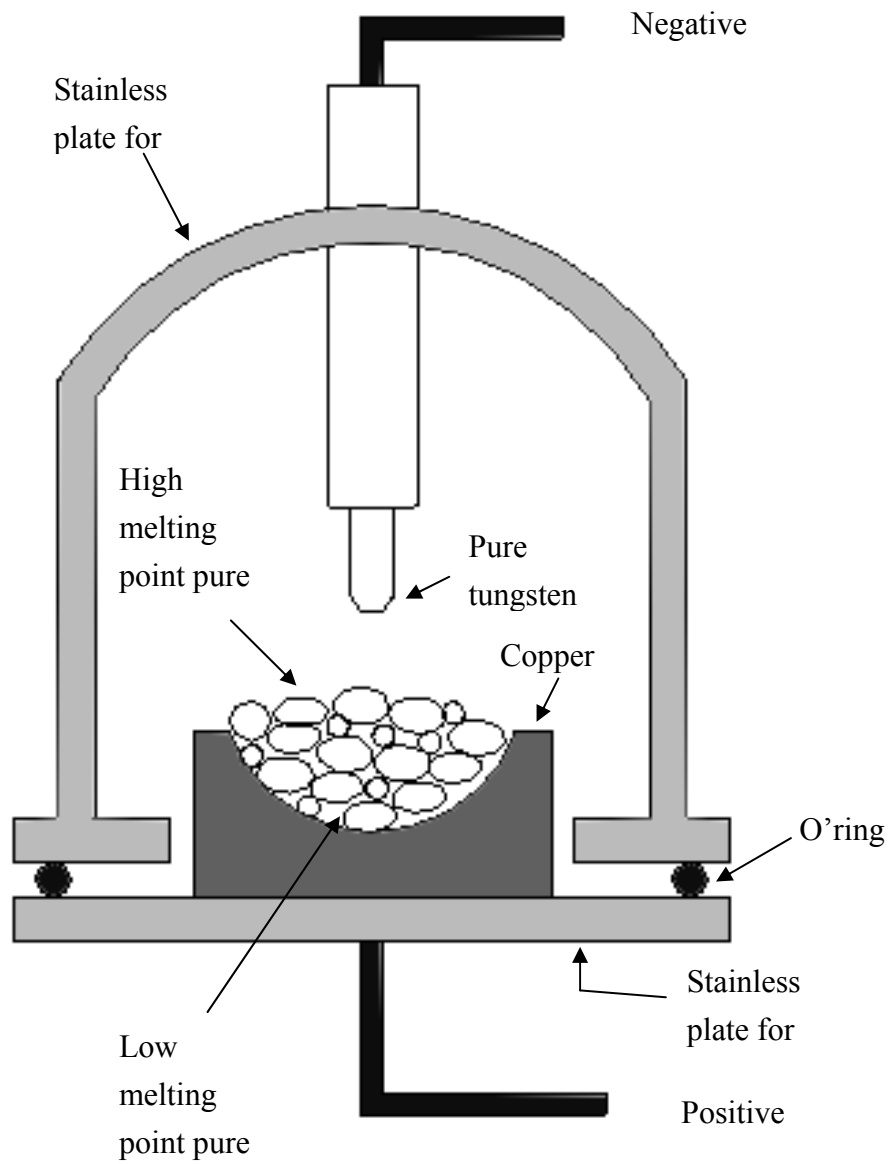


Figure 3.3 Schematic diagram of the arc melting device.

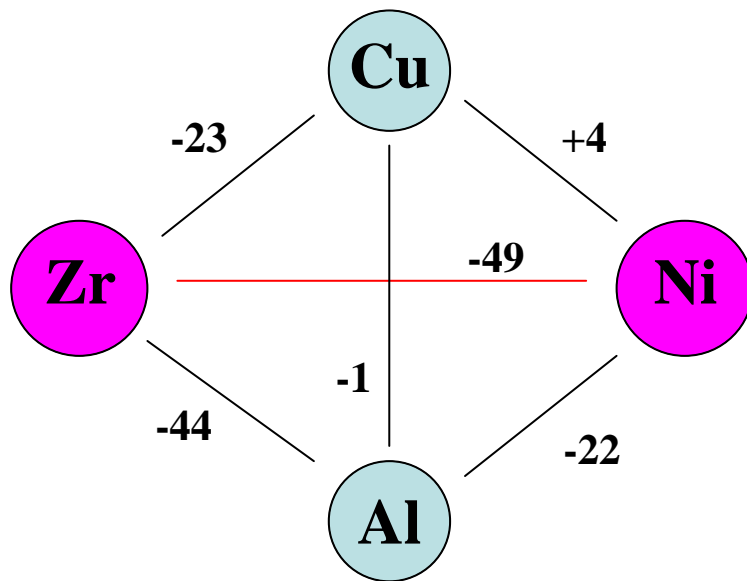


Figure 3.4 The relationship of fusion heat among the constituent elements in the Zr-Cu-Ni-Al alloy system (unit: kJ/mol) [143].

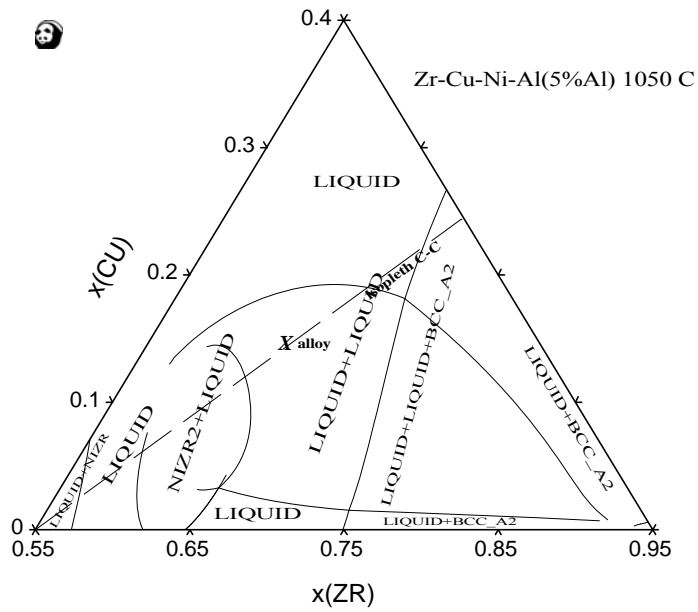


Figure 3.5 The simulated phase diagram for a Zr-rich isothermal section calculated under constant 5 at% Al at 1050 °C [151].

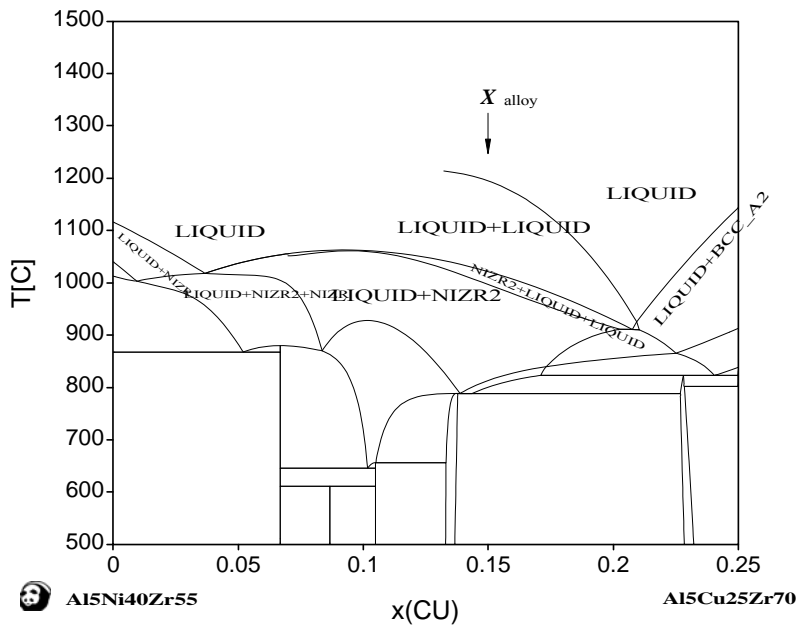


Figure 3.6 The simulated phase diagram for the composition cut between $Zr_5Ni_{40}Zr_{55}$ and $Al_5Cu_{25}Zr_{70}$, obtained from the isopleth C-C in Figure 3.5 [151].



- | | |
|----------------------------------|-------------------------------------|
| 1. Nano Indenter [®] XP | 5. Computer |
| 2. Vibration Isolation Table | 6. Continuous Stiffness Measurement |
| 3. Vibration Isolation Cabinet | 7. Data Acquisition/Control Unit |
| 4. Monitor | 8. Printer |



Figure 3.7 Schematic diagram and photographs of the standard Nano Indenter[®] XP system.

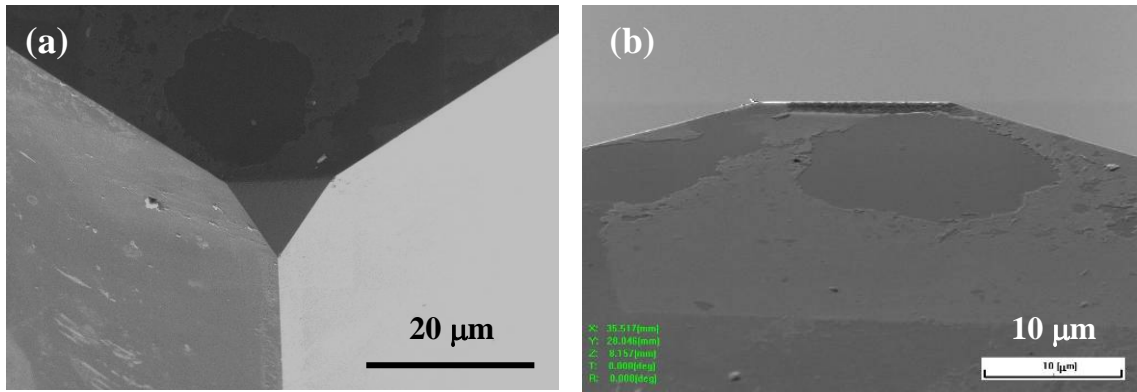


Figure 3.8 SEM micrographs of the flat-punch tip: (a) top view and (b) side view.

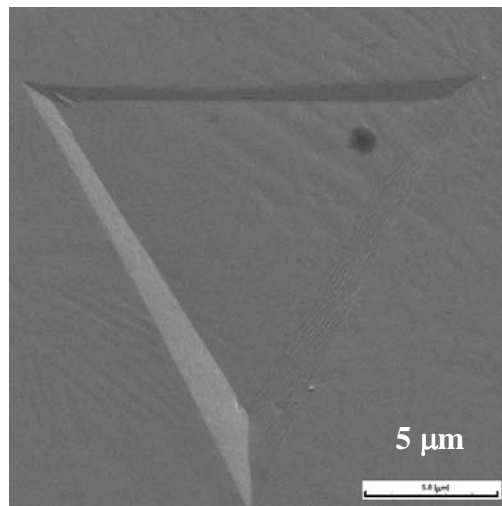


Figure 3.9 SEM micrograph showing the projected area of the punch tip.

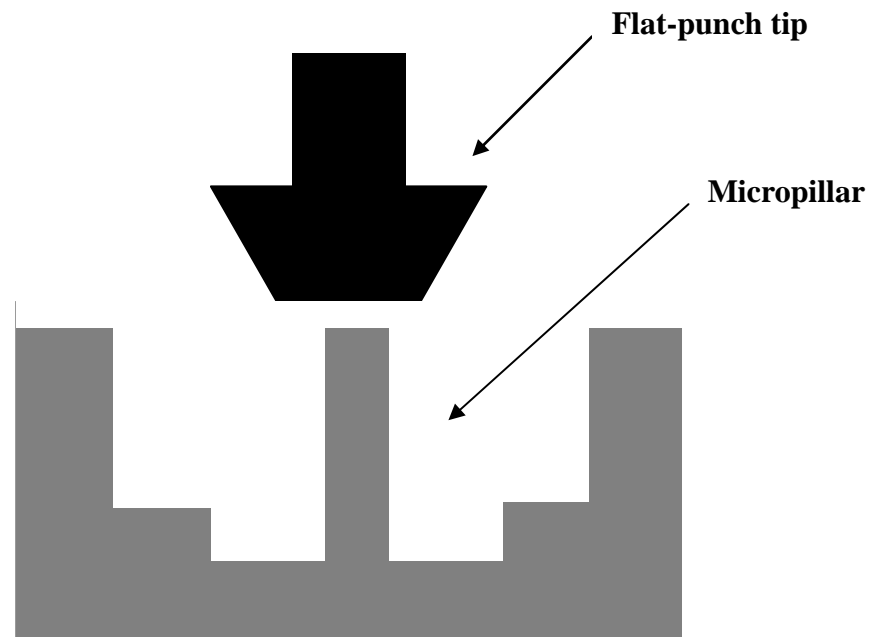


Figure 3.10 Schematic of the microcompression setup. (Black region represents the flat punch indenter tip; the lower grey area represents the micropillar.)

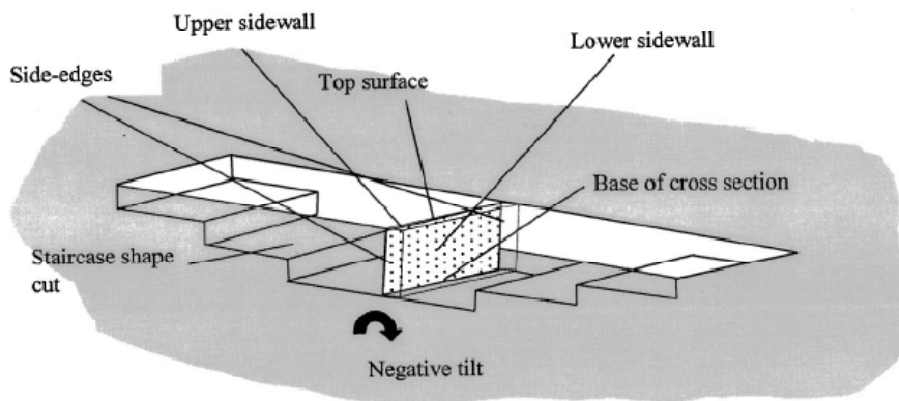


Figure 3.11 Schematic illustration of TEM sample procedure using FIB [156].

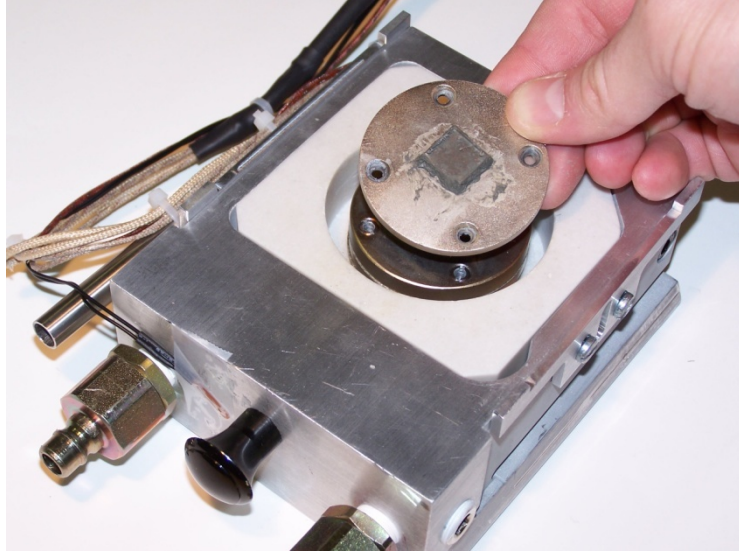


Figure 3.12 The photograph of the heating stage for MTS Nanoindenter XP system.

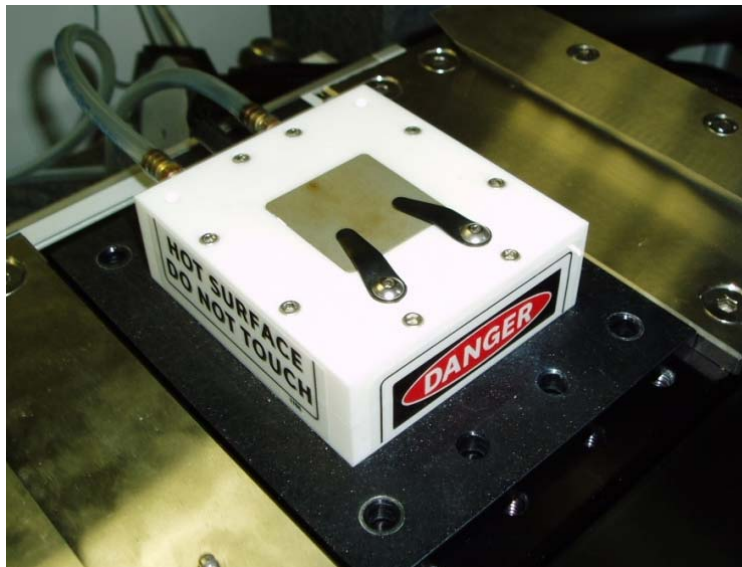


Figure 3.13 The photograph of the heating stage for Hysitron Triboindenter system.



Figure 3.14 The picture of Hysitron Triboindenter system.

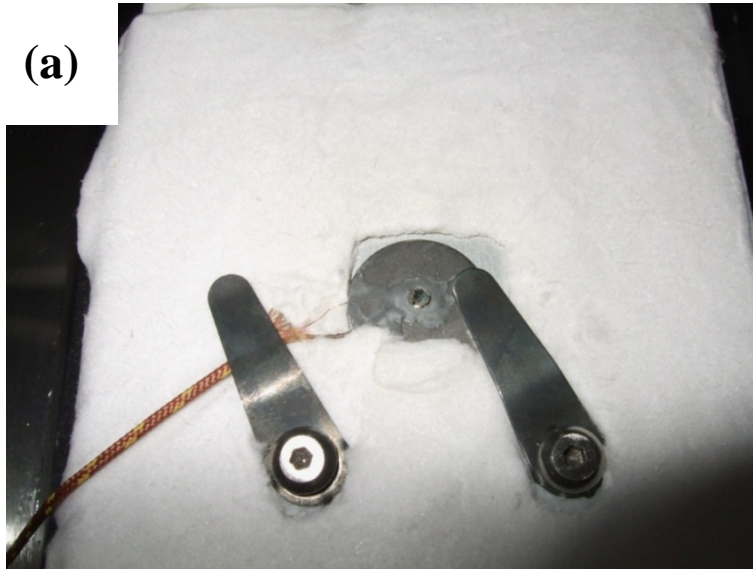


Figure 3.15 The photographs of the heating stage set-up: (a) the heating stage covered with a sheet of alumina-silica paper and (b) test samples attached with a thermal couple.

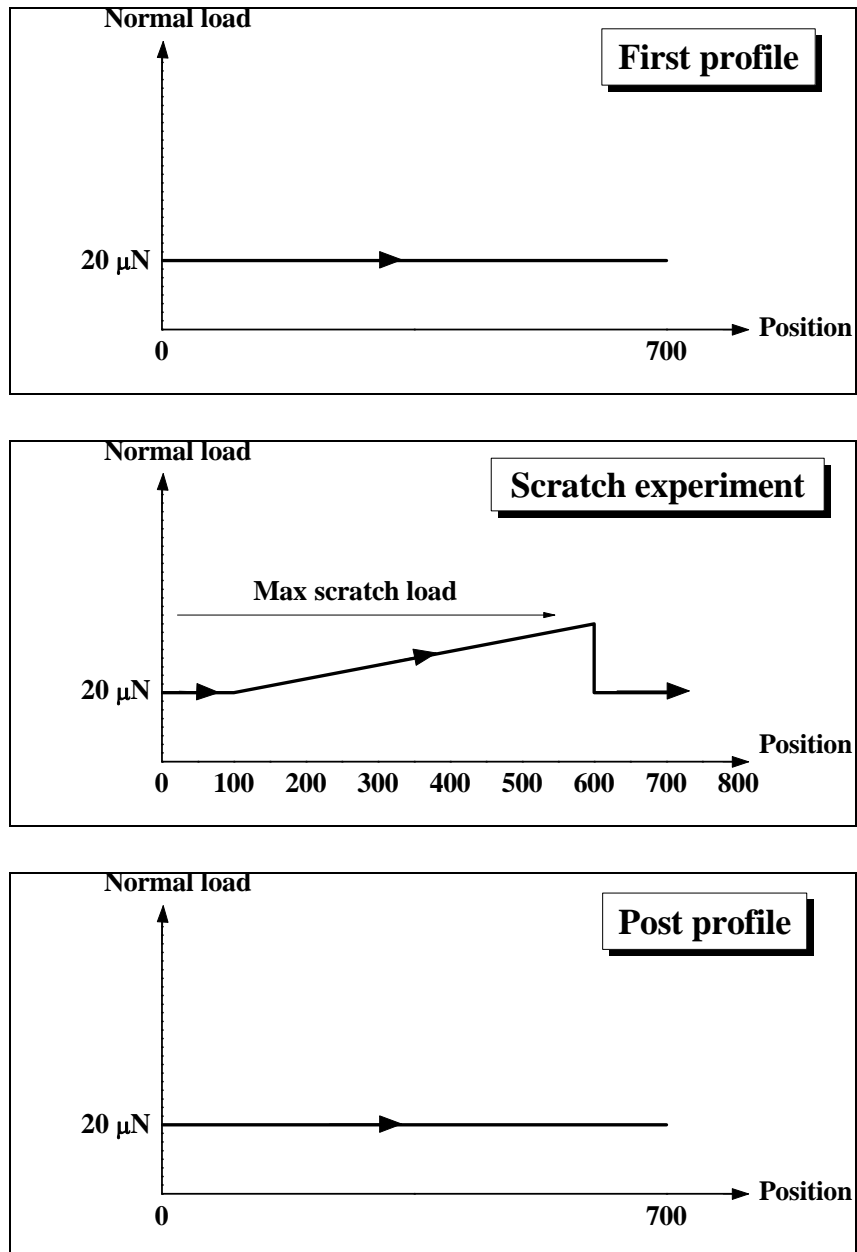
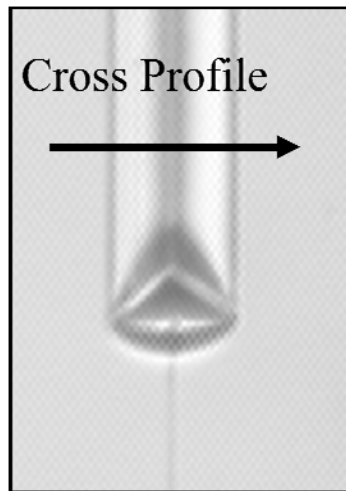


Figure 3.16 Schematic diagrams of the standard scratch procedure.

(a)



(b)

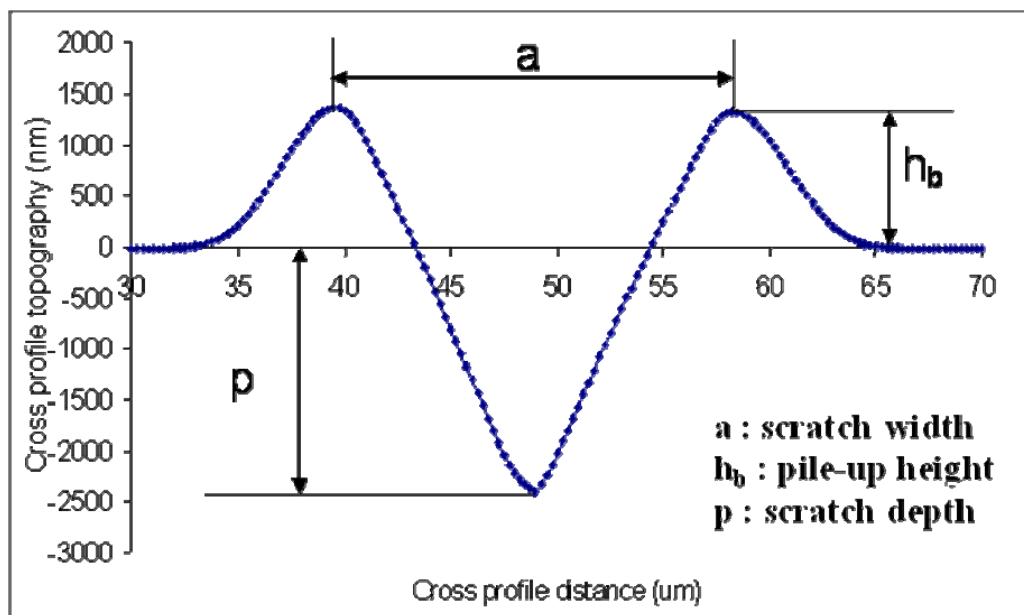


Figure 3.17 (a) A example of the worn scratch track (cross profile direction as indicated by arrow) and (b) a typical result of the cross-sectional profile.

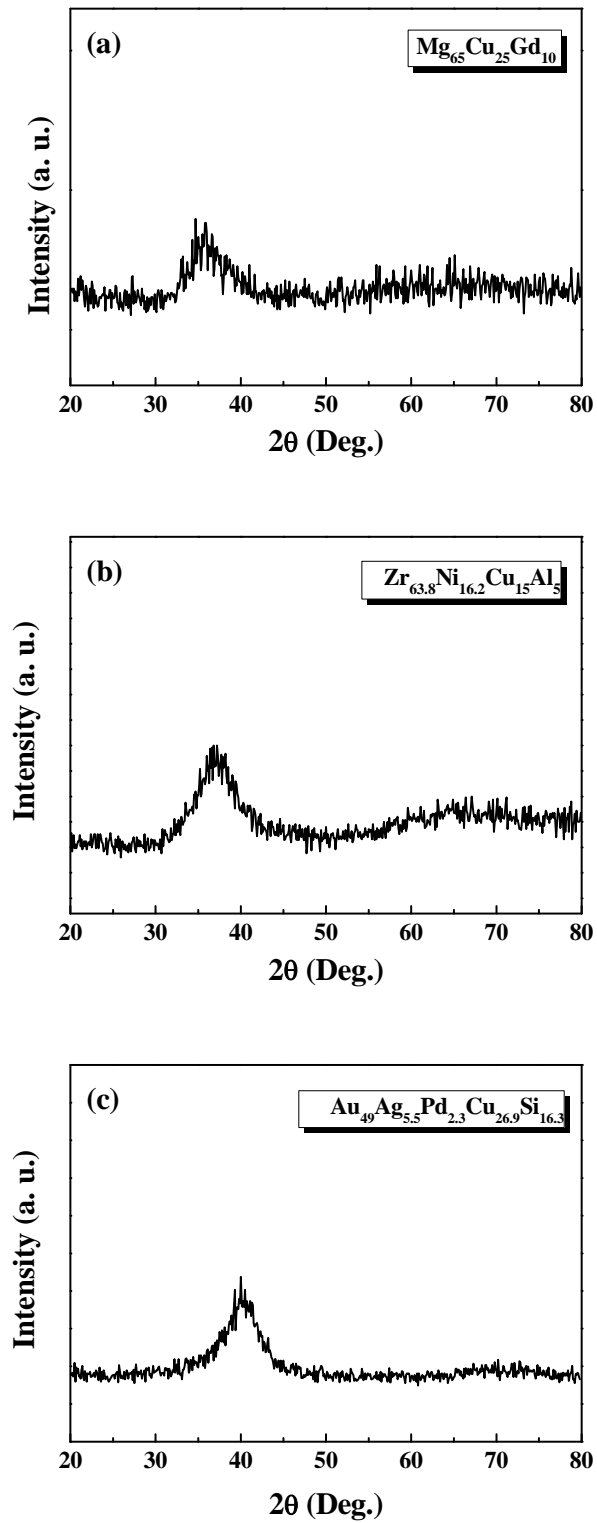


Figure 4.1 XRD patterns taken from the cross-sectional surface of the as-cast (a) $\text{Mg}_{65}\text{Cu}_{25}\text{Gd}_{10}$, (b) $\text{Zr}_{63.8}\text{Ni}_{16.2}\text{Cu}_{15}\text{Al}_5$ and (c) $\text{Au}_{49}\text{Ag}_{5.5}\text{Pd}_{2.3}\text{Cu}_{26.9}\text{Si}_{16.3}$ amorphous alloys.

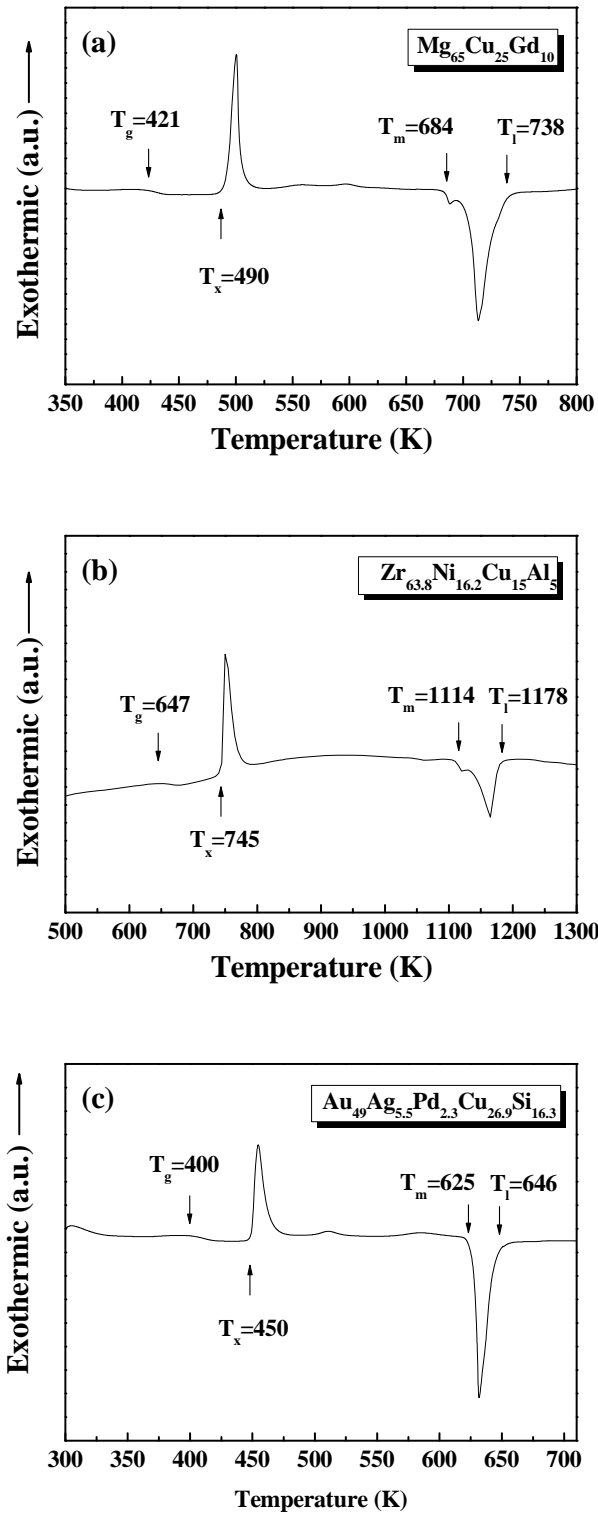


Figure 4.2 DSC thermograms of the as-cast (a) $\text{Mg}_{65}\text{Cu}_{25}\text{Gd}_{10}$, (b) $\text{Zr}_{63.8}\text{Ni}_{16.2}\text{Cu}_{15}\text{Al}_5$ and (c) $\text{Au}_{49}\text{Ag}_{5.5}\text{Pd}_{2.3}\text{Cu}_{26.9}\text{Si}_{16.3}$ amorphous alloys (heating rate of 40 K/min).

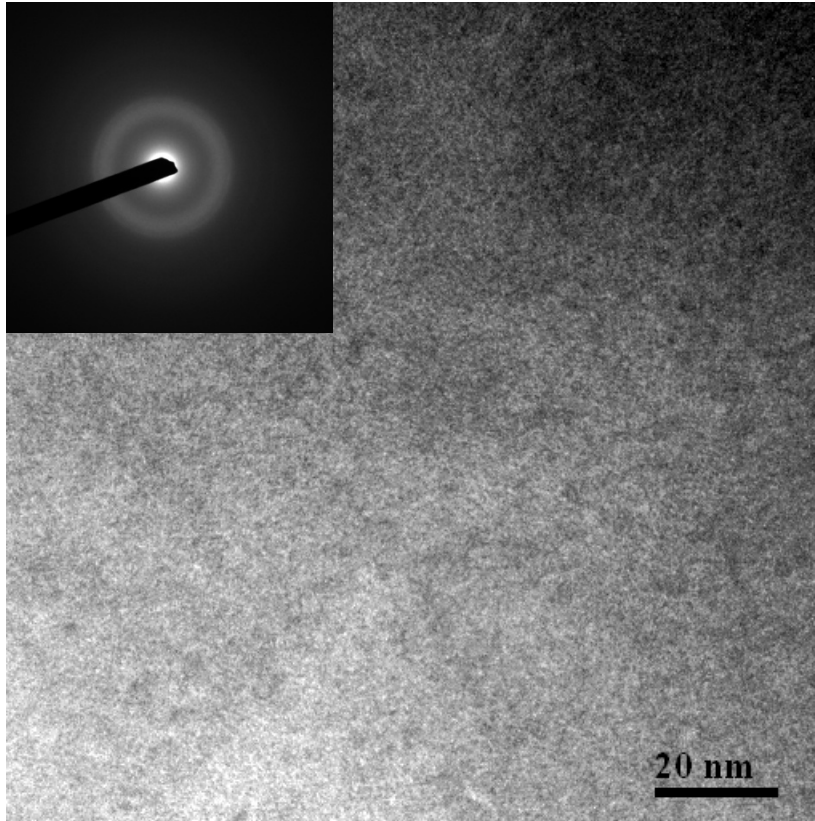


Figure 4.3 TEM bright field image of the as-cast Mg₆₅Cu₂₅Gd₁₀ amorphous alloy with an inserted diffraction pattern.

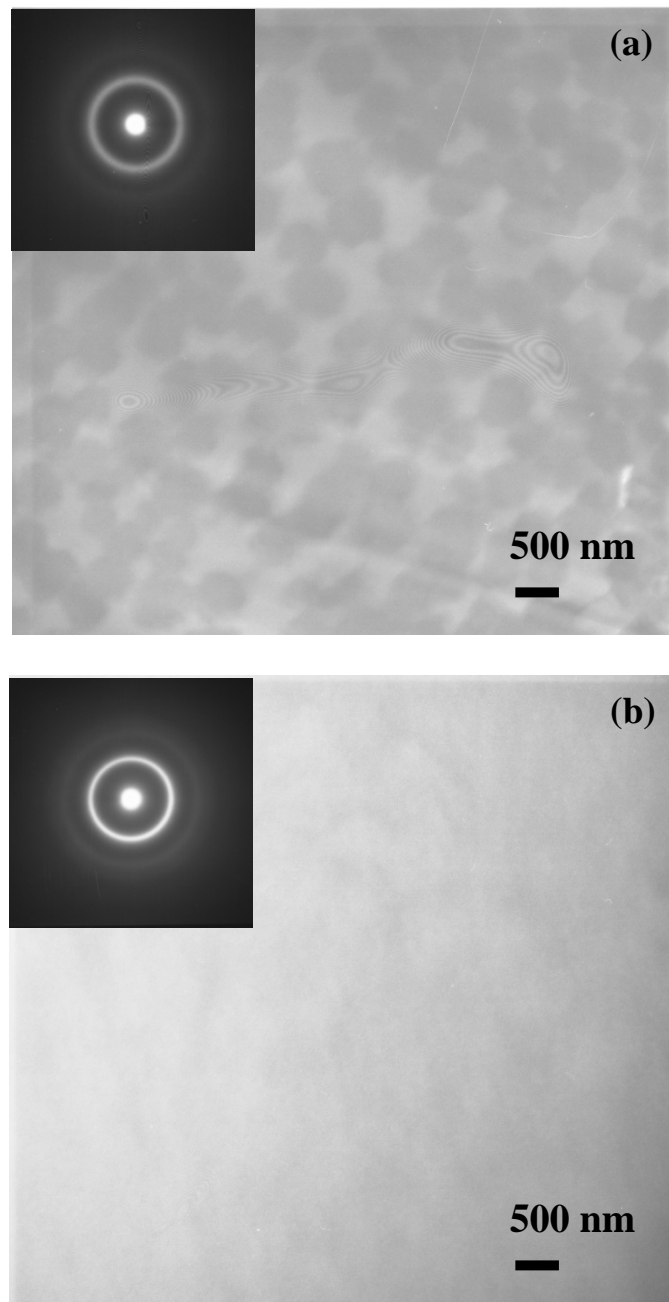


Figure 4.4 TEM bright field images of the as-cast $Zr_{63.8}Ni_{16.2}Cu_{15}Al_5$ amorphous alloy for two different regions with their corresponding diffraction patterns: (a) phase separation region and (b) glassy matrix region.

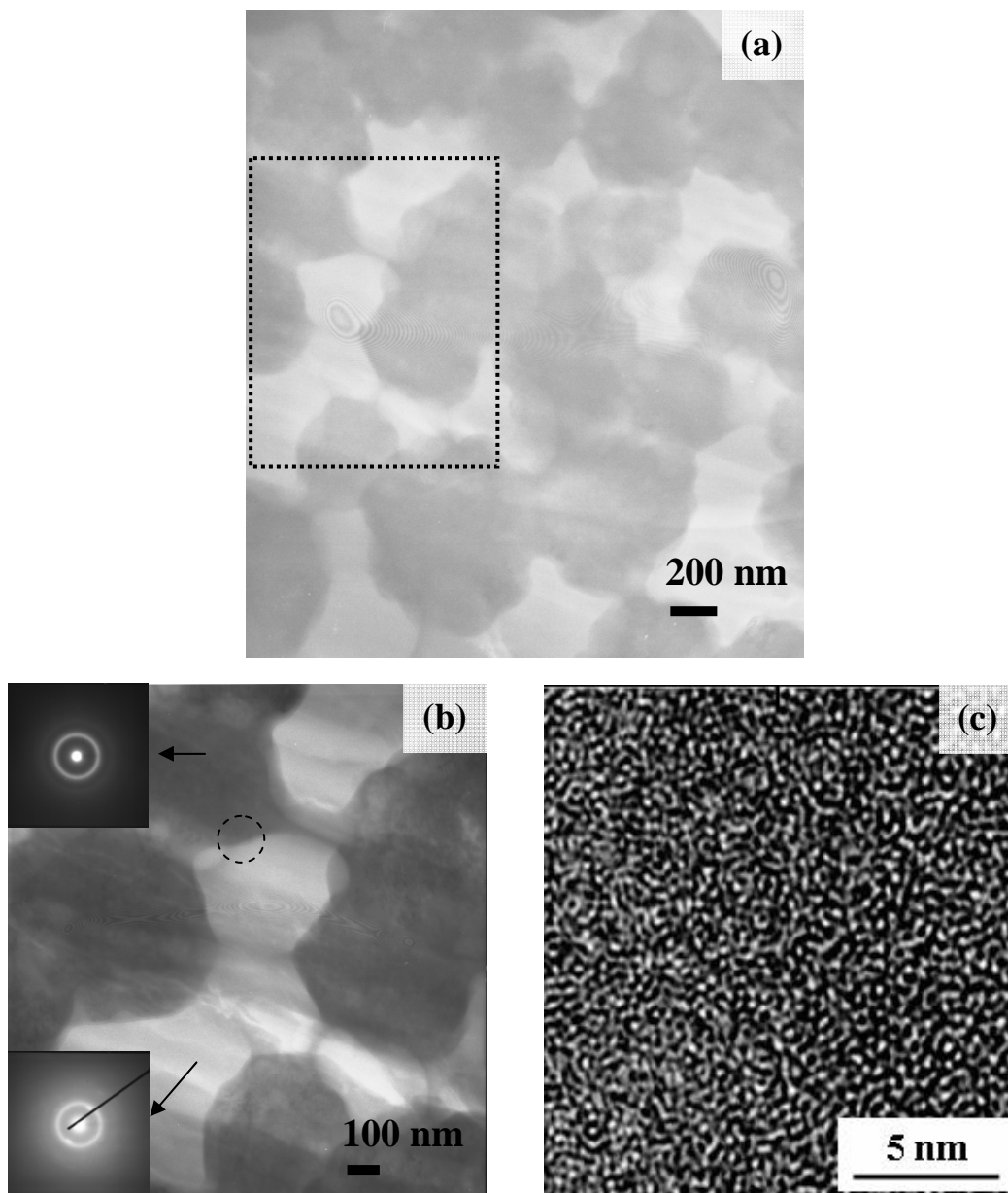


Figure 4.5 Microstructure of the as-cast $Zr_{63.8}Ni_{16.2}Cu_{15}Al_5$ amorphous alloy for the phase separated region: (a) A bright field TEM image, (b) the corresponding selected area diffraction patterns of the bright and dark regions, and (c) HREM image of the interface denoted by the dotted circle in (b).

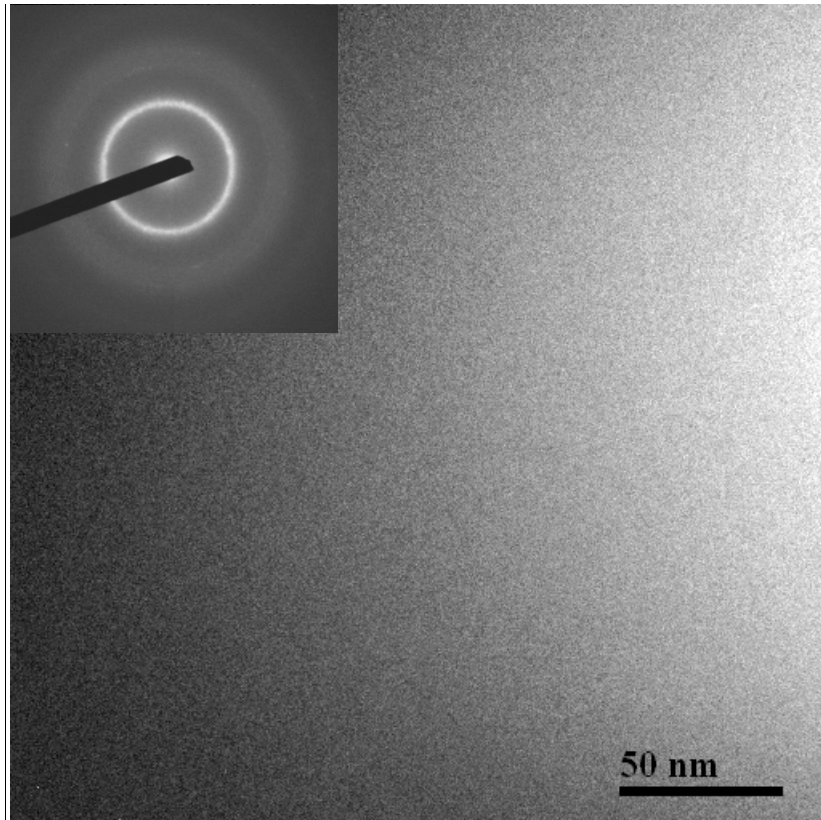


Figure 4.6 TEM bright field image of the as-cast $\text{Au}_{49}\text{Ag}_{5.5}\text{Pd}_{2.3}\text{Cu}_{26.9}\text{Si}_{16.3}$ amorphous alloy with an inserted diffraction pattern.

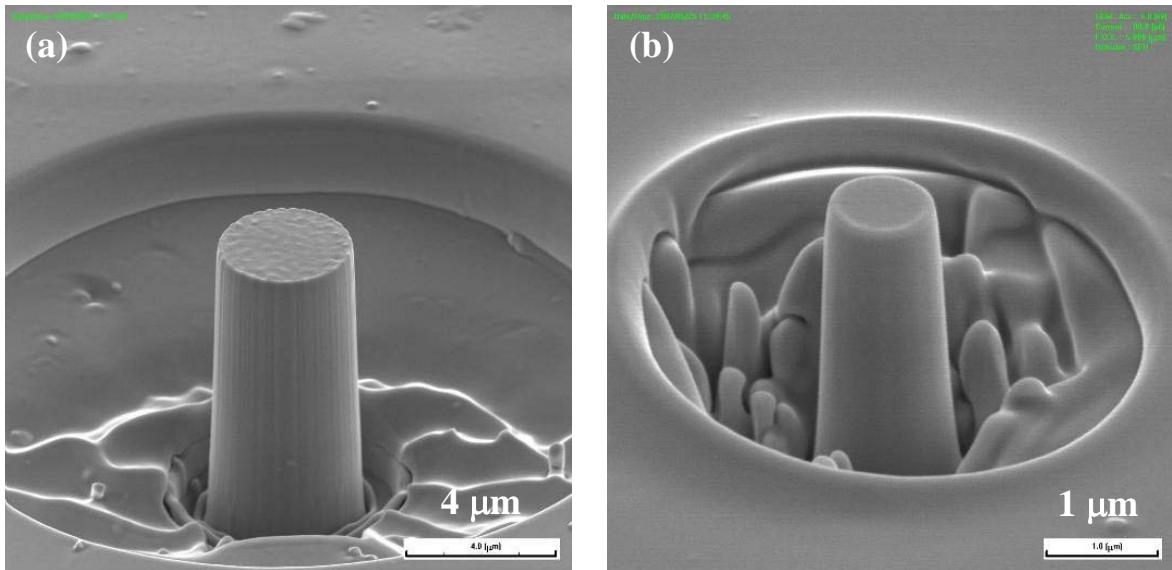


Figure 4.7 SEM micrographs of pillars for the Mg-based BMG before microcompression test. The pillars with diameters of (a) 3.8 μm and (b) 1 μm . The tilt angle of the sample in SEM is 55° for both images.

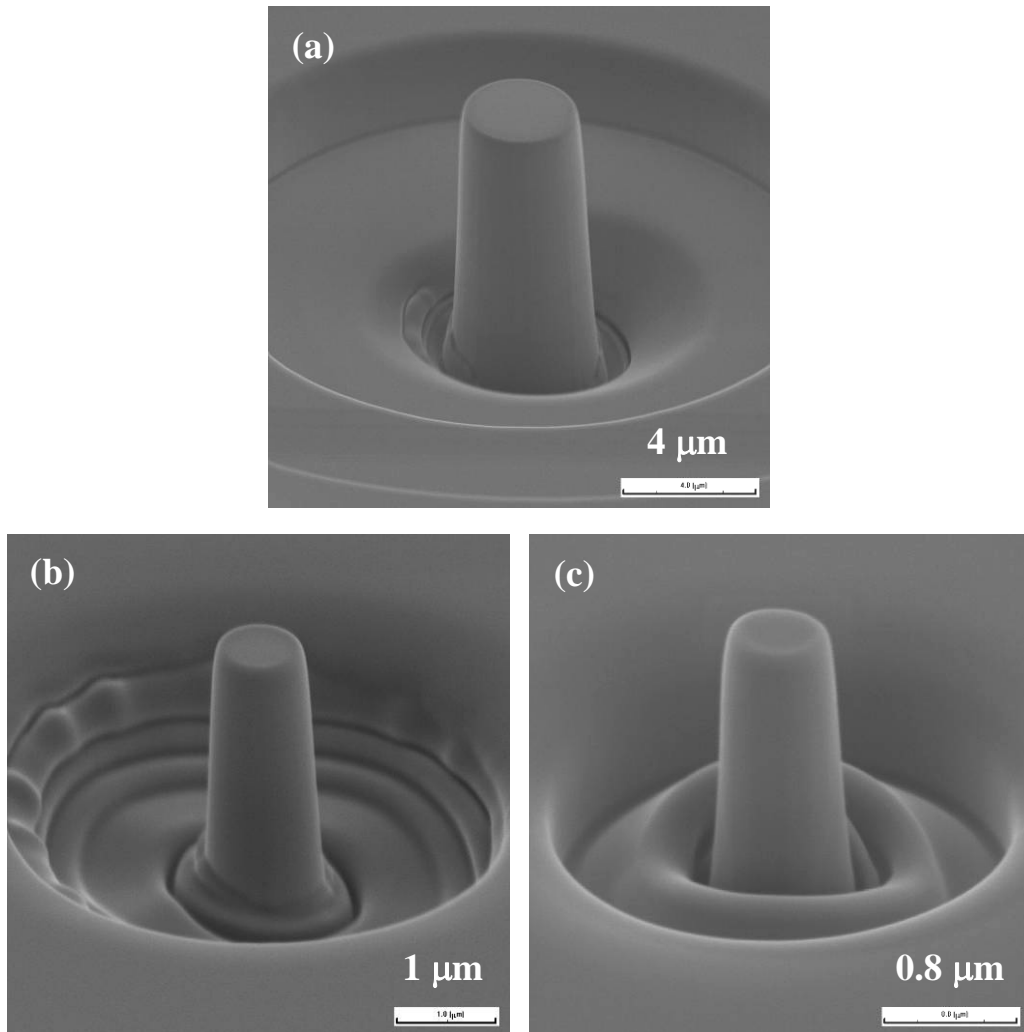


Figure 4.8 SEM micrographs of pillars for the Zr-based BMG before microcompression test. The pillars with diameters of (a) 3.8 μm, (b) 1 μm and (c) 700 nm. The tilt angle of the sample in SEM is 55° for all images.

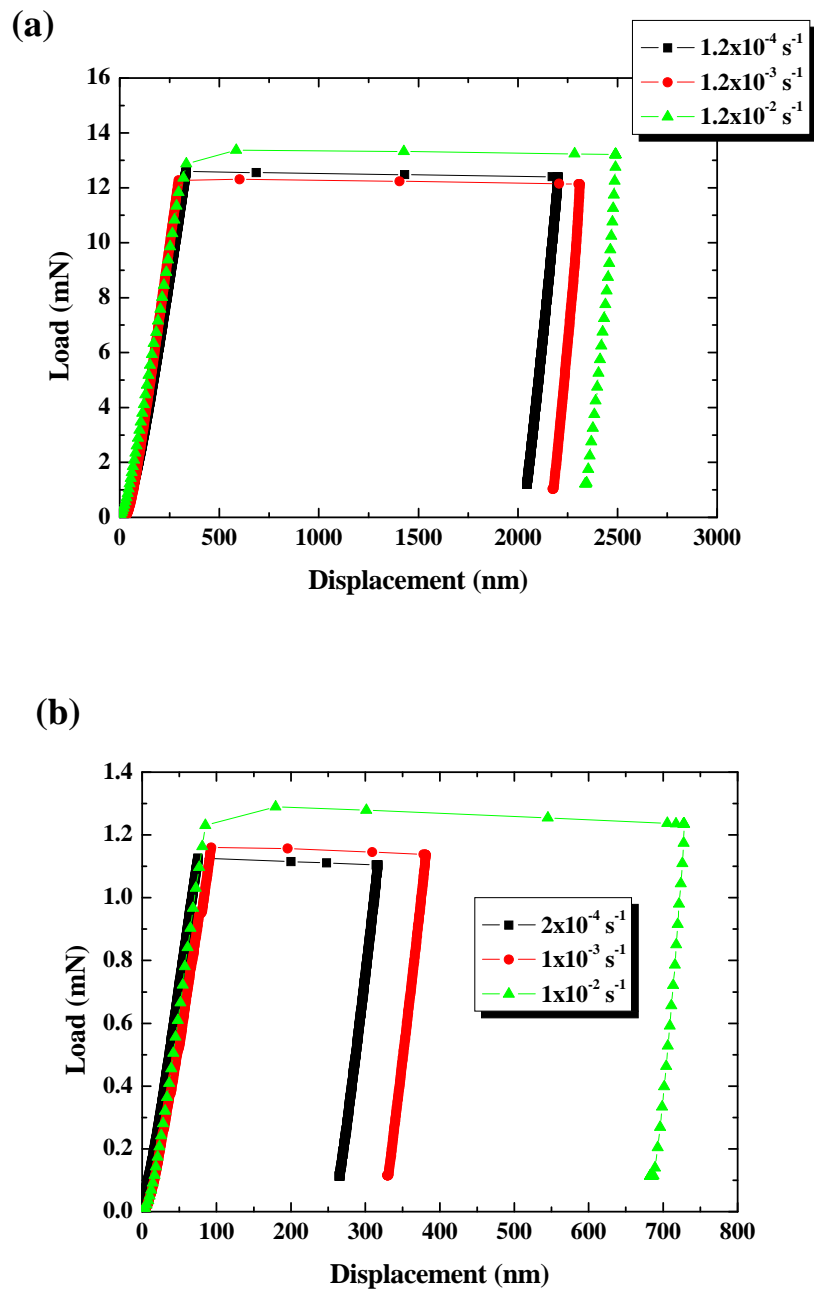


Figure 4.9 Compressive load-displacement curves of the Mg-based BMG of (a) 3.8 μm and (b) 1 μm at different strain rates.

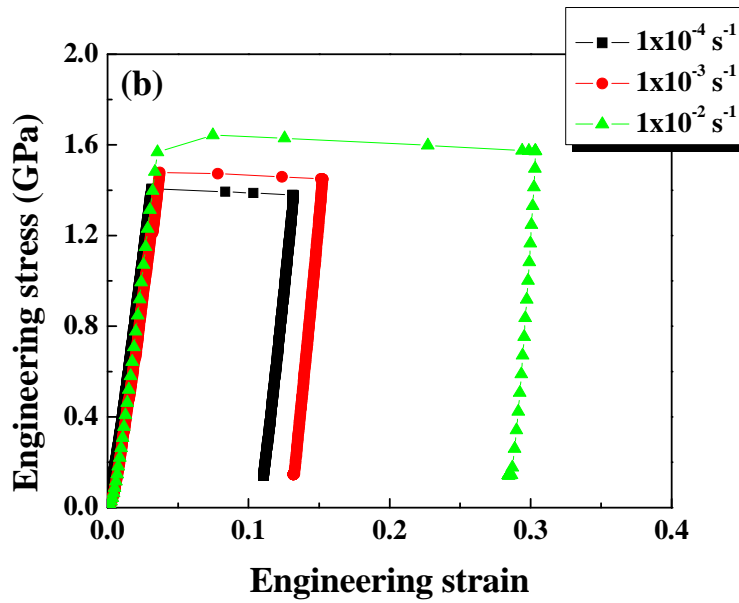
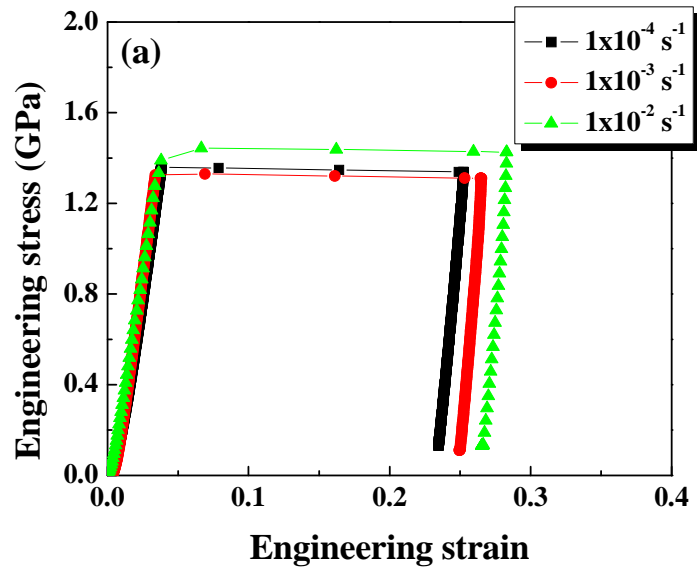


Figure 4.10 The engineering stress-strain curves of the Mg-based BMG of (a) 3.8 μm and (b) 1 μm at different strain rates.

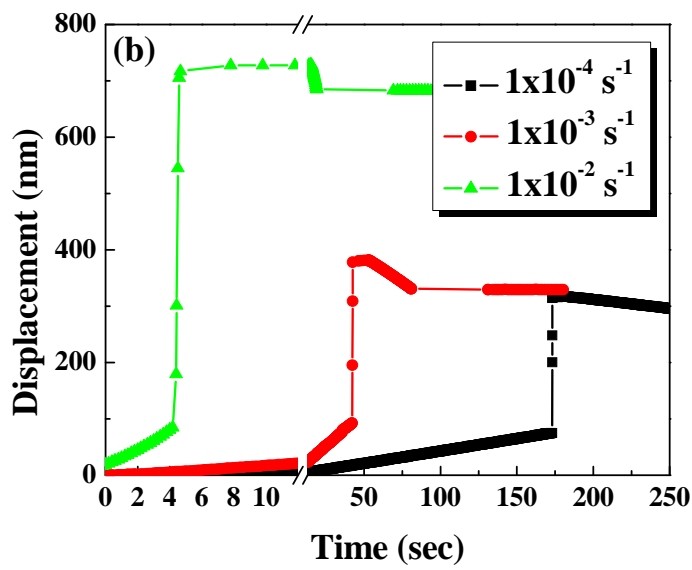
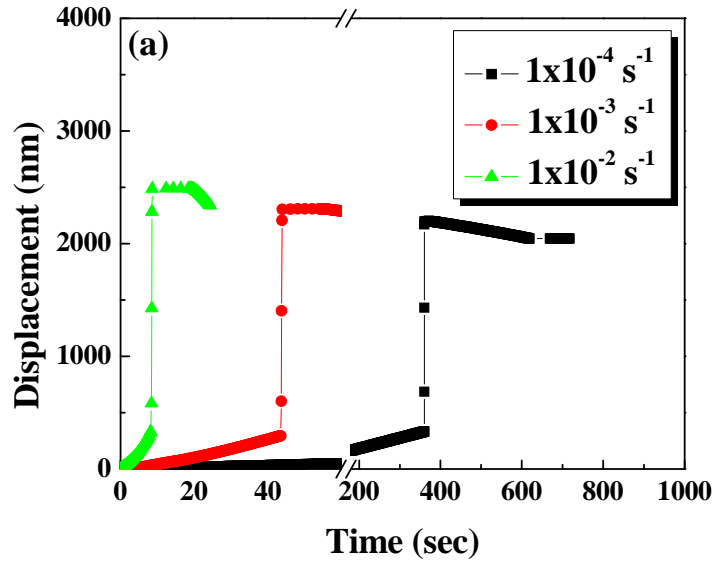


Figure 4.11 The displacement-time curves of the Mg-based BMG of (a) 3.8 μm and (b) 1 μm at different strain rates.

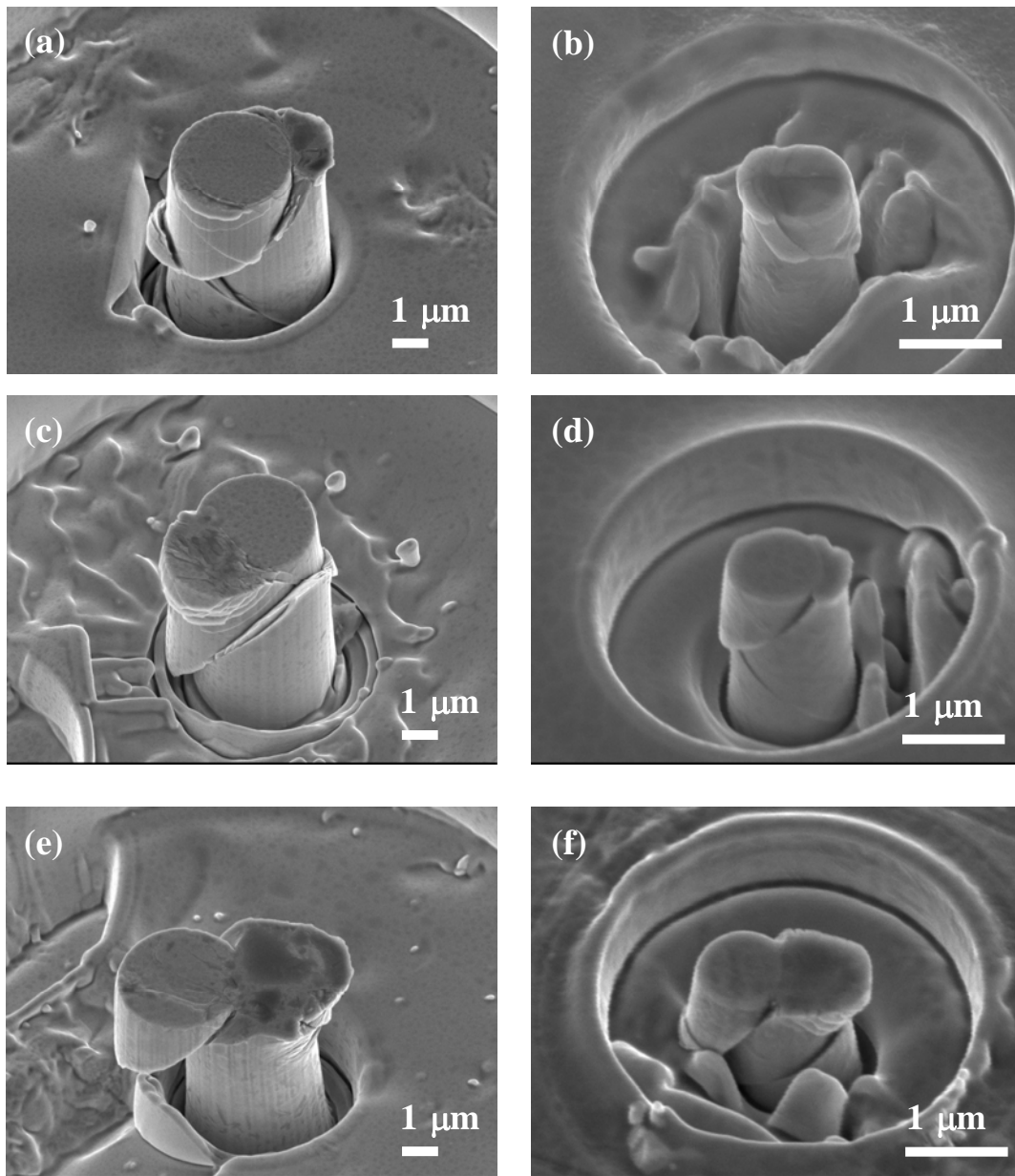


Figure 4.12 SEM micrographs showing the appearance of deformed pillars for the Mg-based BMG with the size and strain rate: (a) 3.8 μm , $\sim 6 \times 10^{-4} \text{ s}^{-1}$, (b) 1 μm , $\sim 2 \times 10^{-4} \text{ s}^{-1}$, (c) 3.8 μm , $\sim 1.2 \times 10^{-3} \text{ s}^{-1}$, (d) 1 μm , $\sim 1 \times 10^{-3} \text{ s}^{-1}$, (e) 3.8 μm , $\sim 1 \times 10^{-2} \text{ s}^{-1}$, and (f) 1 μm , $\sim 1 \times 10^{-2} \text{ s}^{-1}$.

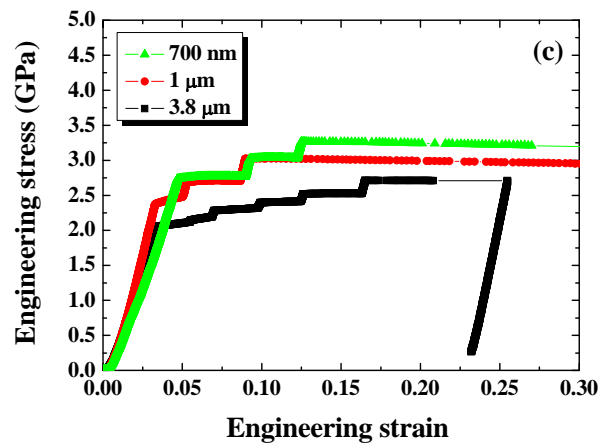
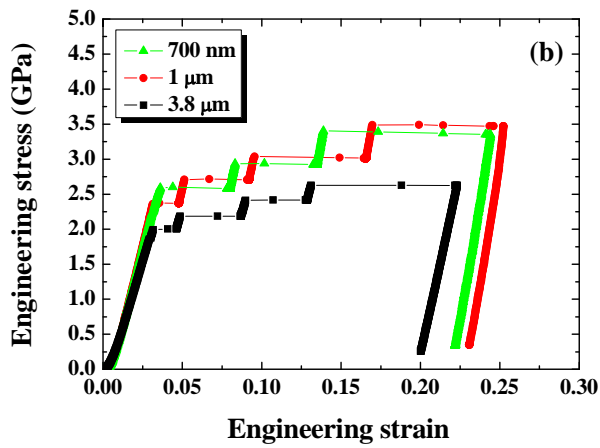
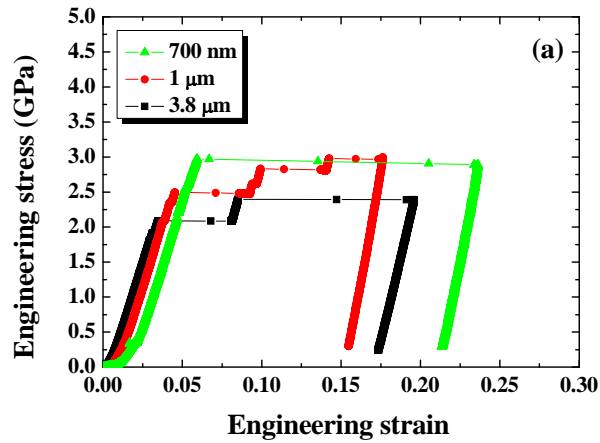


Figure 4.13 The microcompression engineering stress-strain curves of the 3.8 μm , 1 μm and 700 nm micropillars at different strain rates of (a) $1 \times 10^{-4} \text{ s}^{-1}$, (b) $1 \times 10^{-3} \text{ s}^{-1}$, and (c) $1 \times 10^{-2} \text{ s}^{-1}$.

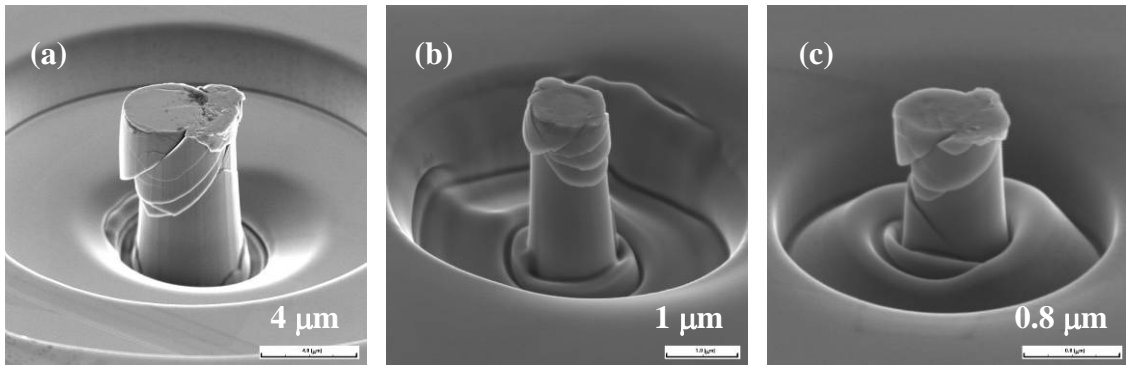


Figure 4.14 SEM micrographs showing the appearance of deformed pillars for the Zr-based BMG at a strain rate of $1 \times 10^{-4} \text{ s}^{-1}$: (a) $3.8 \mu\text{m}$, (b) $1 \mu\text{m}$, and (c) 700 nm .

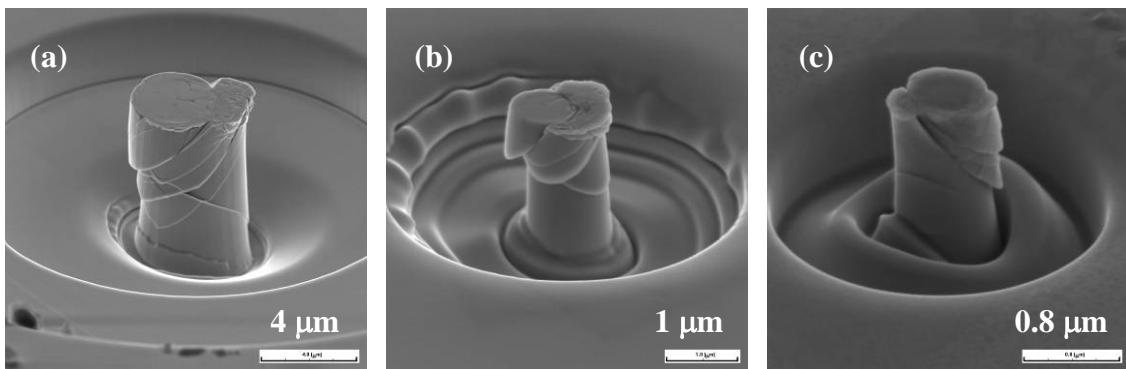


Figure 4.15 SEM micrographs showing the appearance of deformed pillars for the Zr-based BMG at a strain rate of $1 \times 10^{-3} \text{ s}^{-1}$: (a) $3.8 \mu\text{m}$, (b) $1 \mu\text{m}$, and (c) 700 nm .

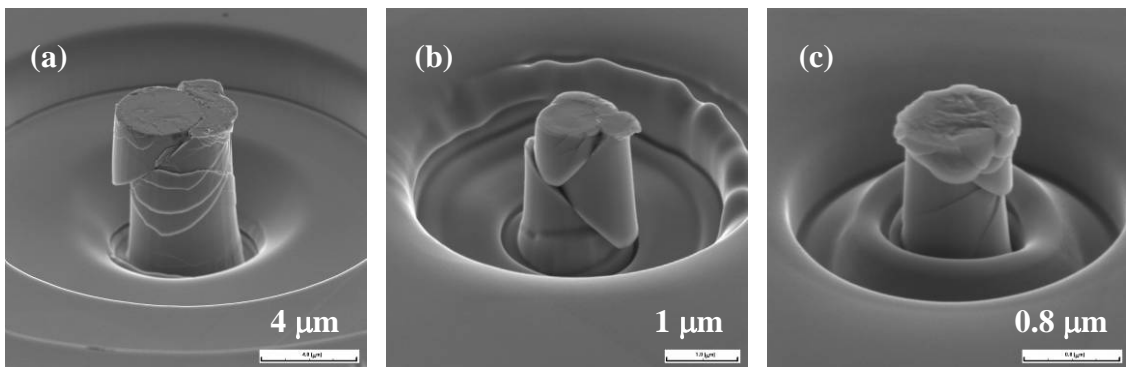


Figure 4.16 SEM micrographs showing the appearance of deformed pillars for the Zr-based BMG at a strain rate of $1 \times 10^{-2} \text{ s}^{-1}$: (a) $3.8 \mu\text{m}$, (b) $1 \mu\text{m}$, and (c) 700 nm .

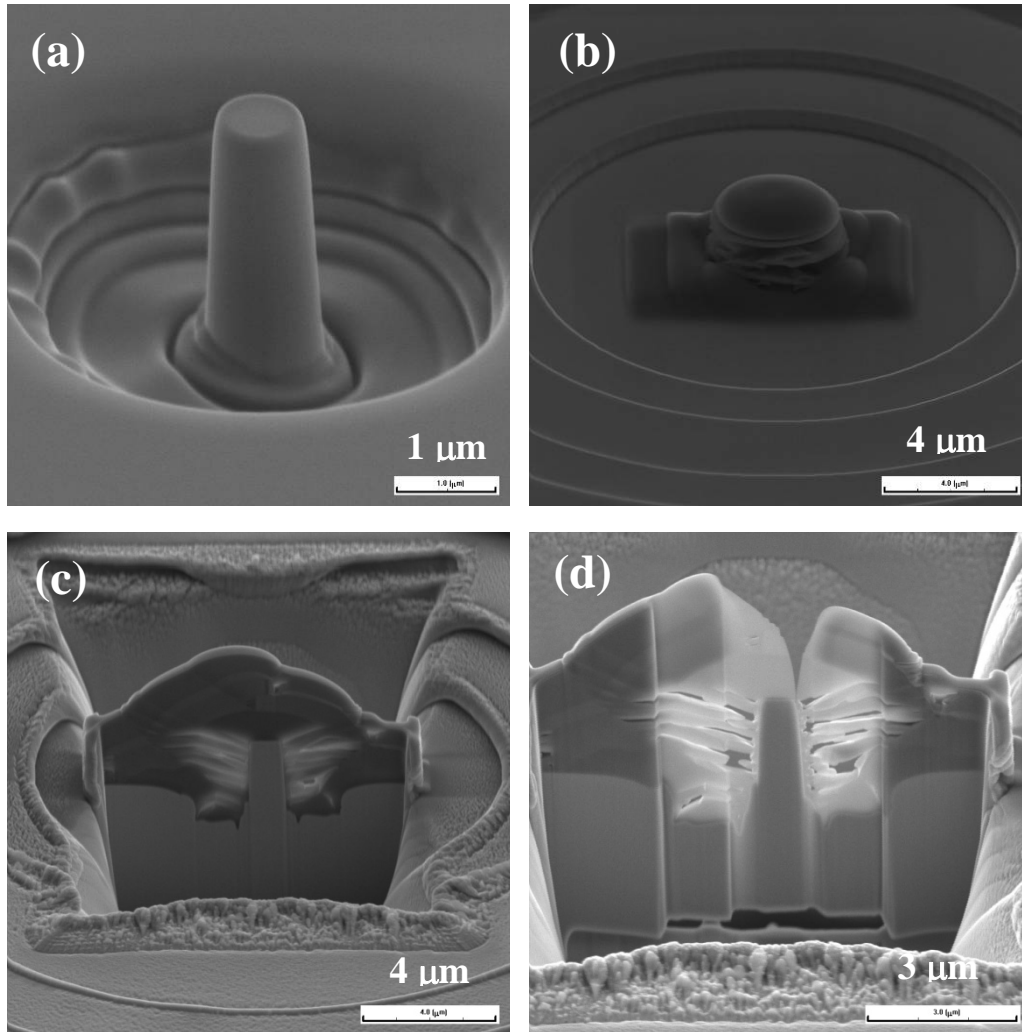


Figure 4.17 TEM sample preparation procedures: (a) Zr-based BMG micropillar with 1 μm diameter before compression test, (b) carbon is deposited around the pillar, (c) an energetic Ga ion beam is used to cut the trench, and (d) TEM sample can be further thinned by using the Ga ion beam with lower voltage or current. The tilt angle of the sample in SEM is 55° for all images.

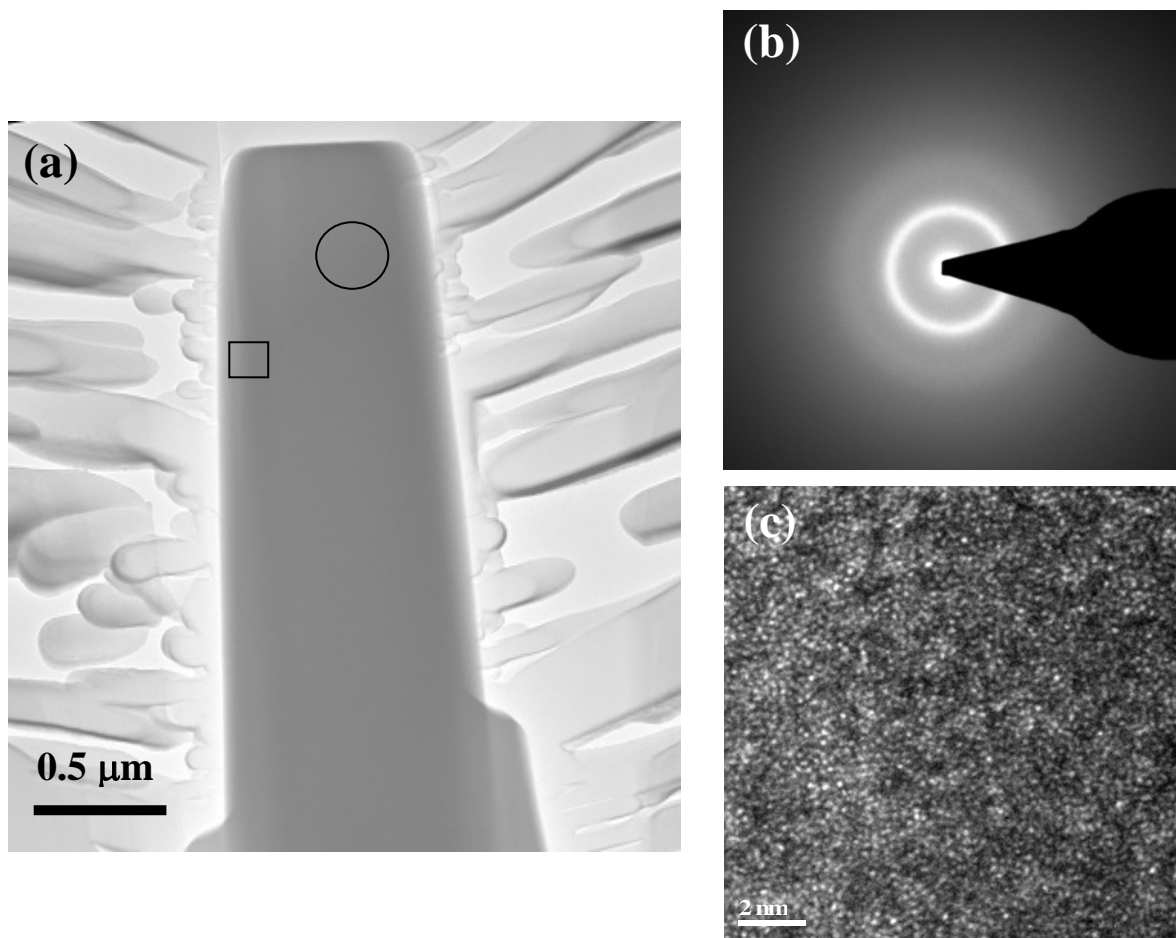


Figure 4.18 (a) Bright field TEM image of a lamella prepared from the undeformed Zr-based pillar. (b) A diffraction pattern from the indicated region of the pillar in figure (a), as marked by a circle. (c) The HREM image from the indicated region of the pillar in figure (a), as marked by a square.

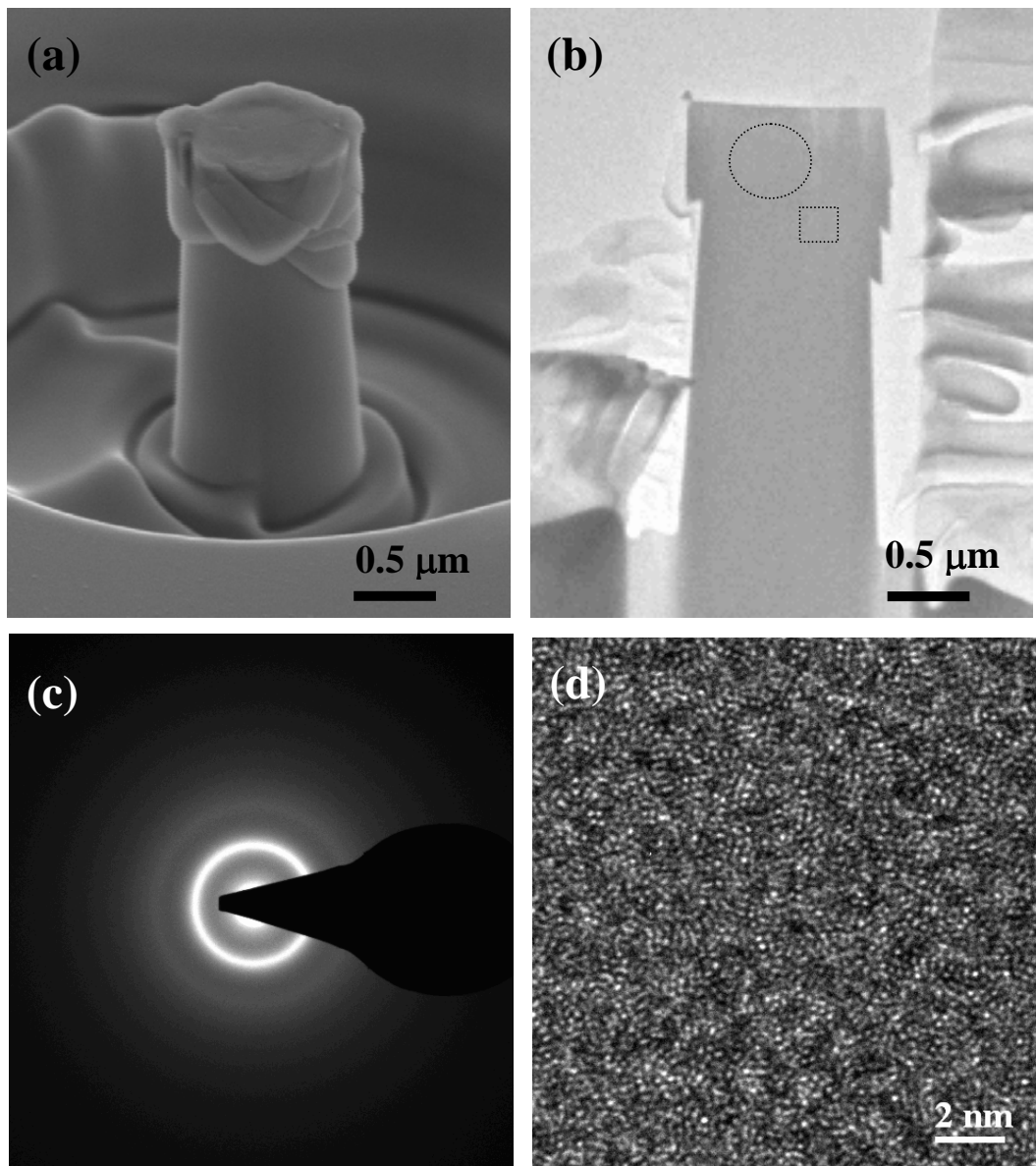


Figure 4.19 (a) The SEM image showing the 1 μ m Zr-based BMG pillar sample. (b) The corresponding bright field TEM image. (c) A diffraction pattern from the indicated region of the pillar in figure (b), as marked by a circle. (d) The HREM image from the indicated region of the pillar in figure (a), as marked by a square.

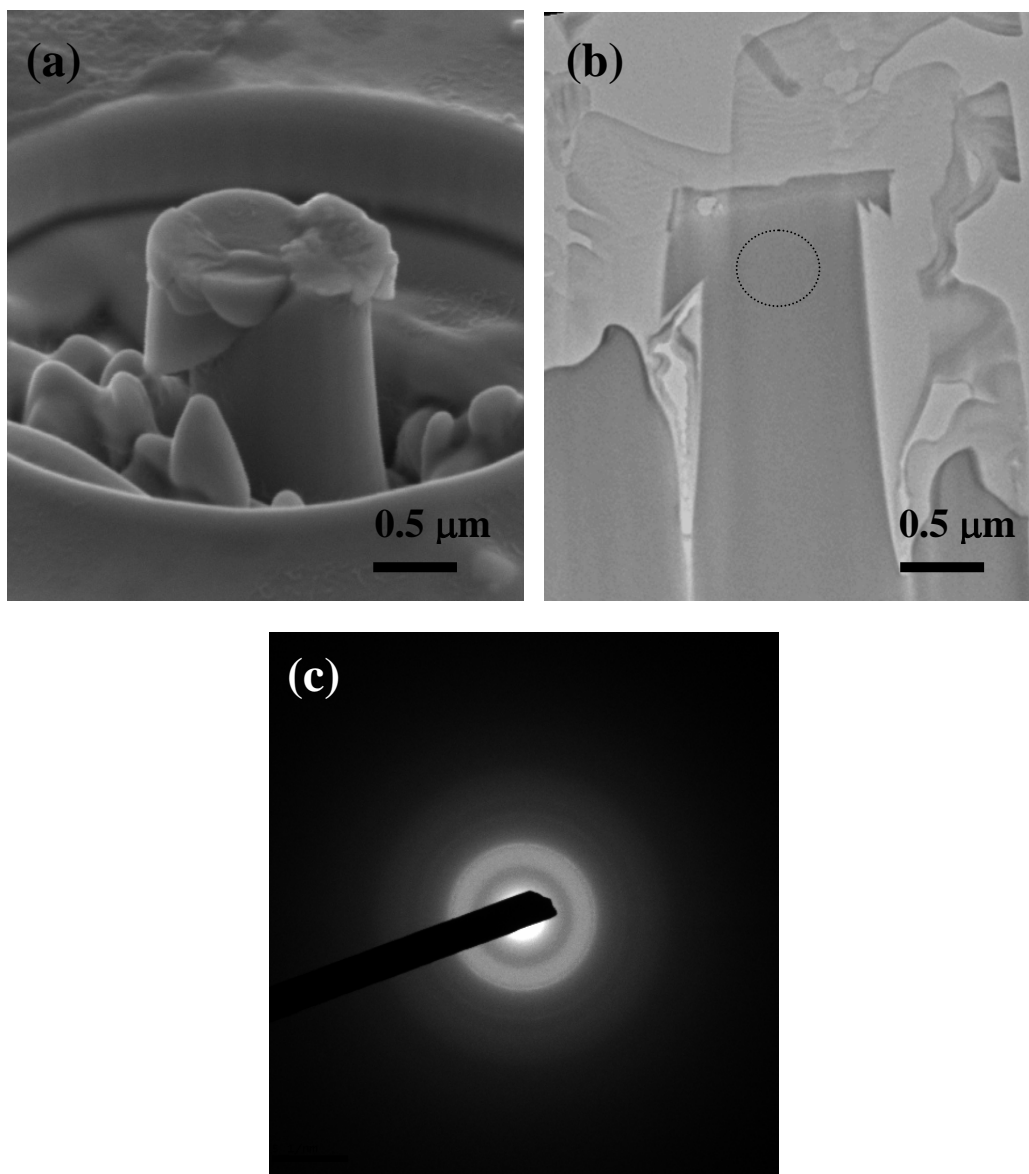


Figure 4.20 (a) The SEM image showing the 1 μm Mg-based BMG pillar sample. (b) The corresponding bright field TEM image. (c) A diffraction pattern from the indicated region of the pillar in figure (b), as marked by a circle.

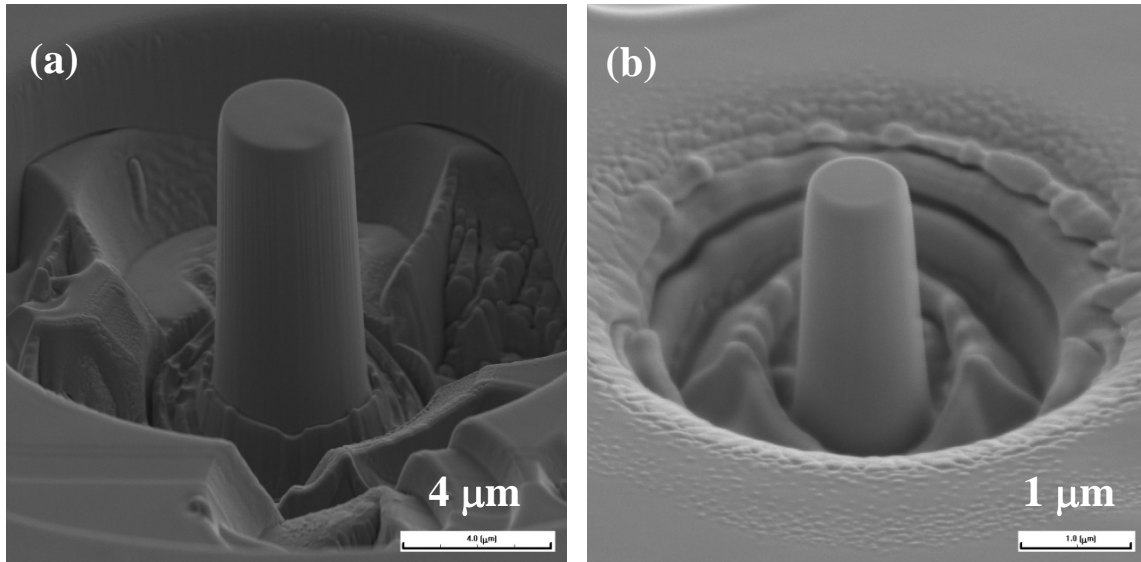


Figure 4.21 SEM micrographs of pillars for the Au-based BMG before microcompression test. The pillars with diameters of (a) 3.8 μm and (b) 1 μm.

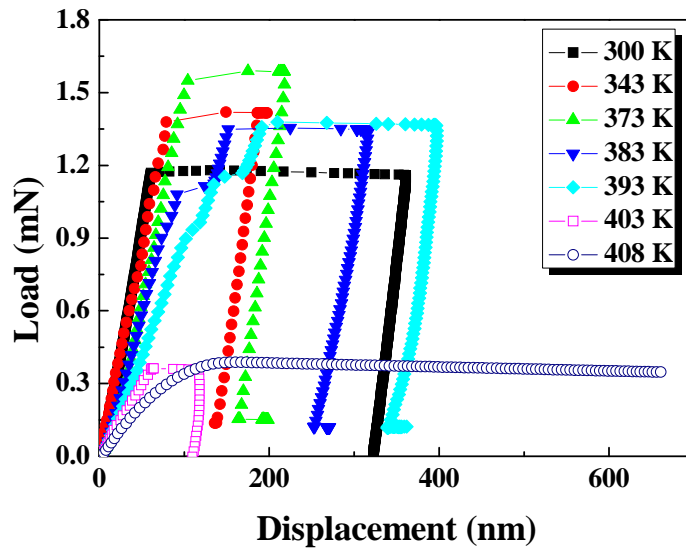


Figure 4.22 Compressive load-displacement curves of the 1 μm Au-based BMG pillar samples deformed at different temperatures.

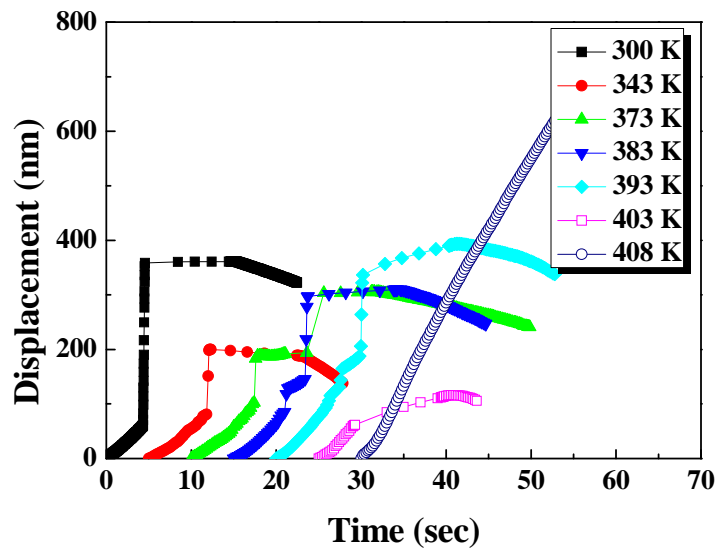


Figure 4.23 The time-displacement curves of the 1 μm Au-based BMG pillar samples deformed at different temperatures.

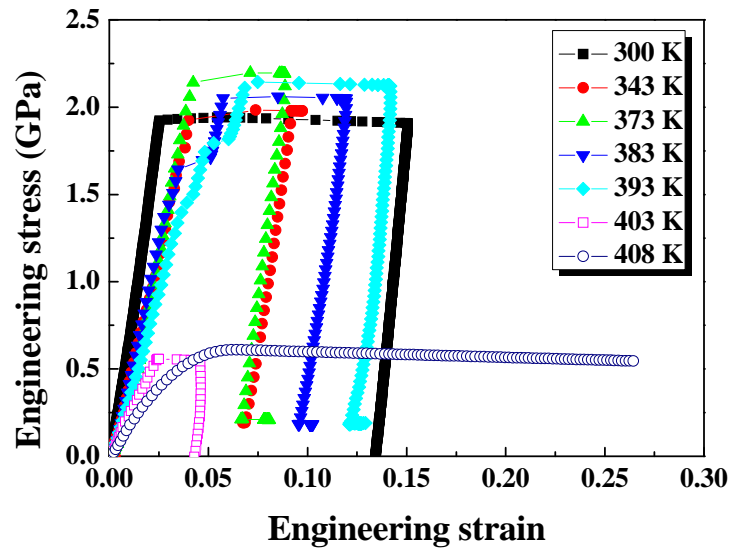


Figure 4.24 The engineering stress-strain curves of the 1 μm Au-based BMG pillar samples deformed at different temperatures.

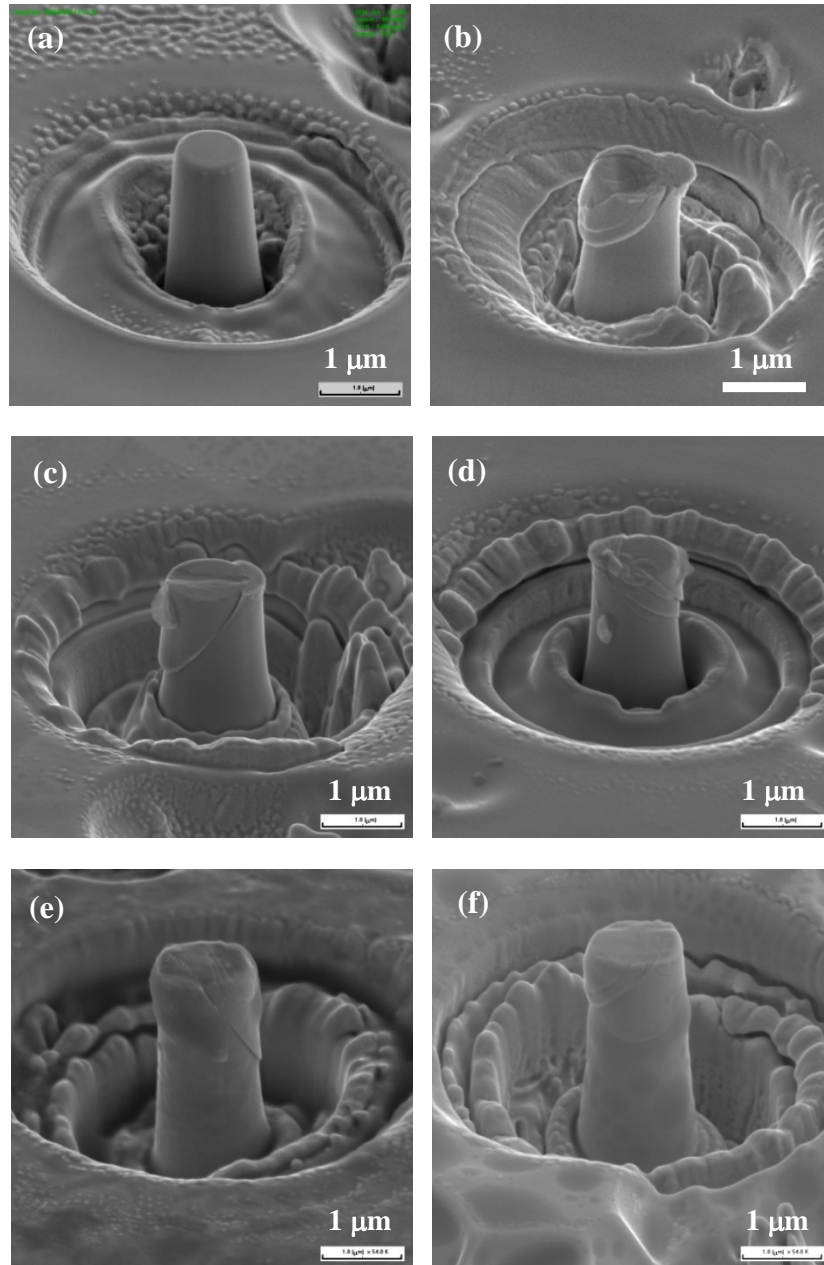


Figure 4.25 SEM images of the 1 μm Au-based BMG pillar sample (a) before and after compression at (b) room temperature, (c) 343 K, (d) 373 K, (e) 383 K and (f) 393 K.

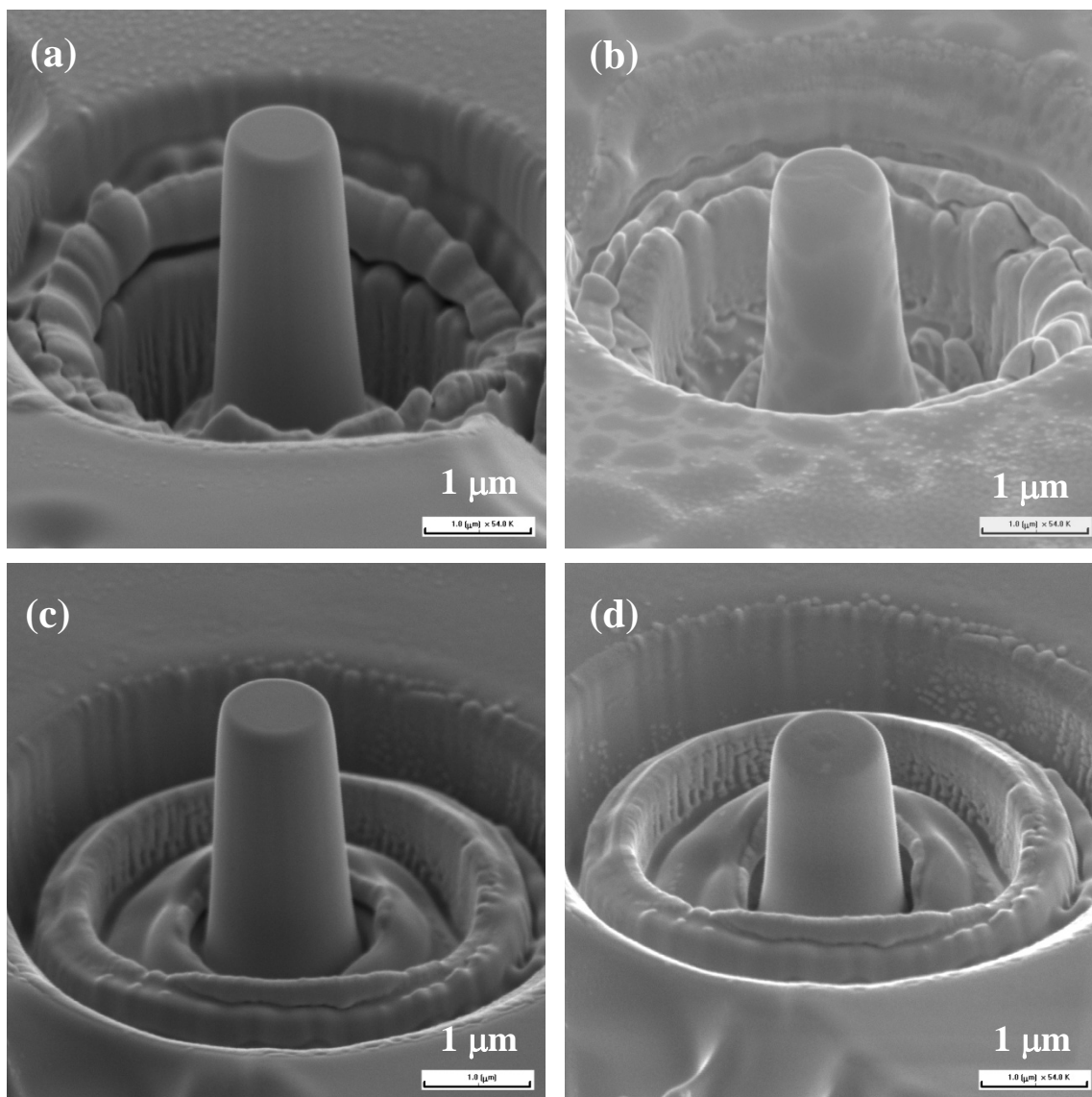


Figure 4.26 SEM images of the 1 μm Au-based BMG pillar sample (a) (c) before and (b) (d) after compression at 403 and 408 K.

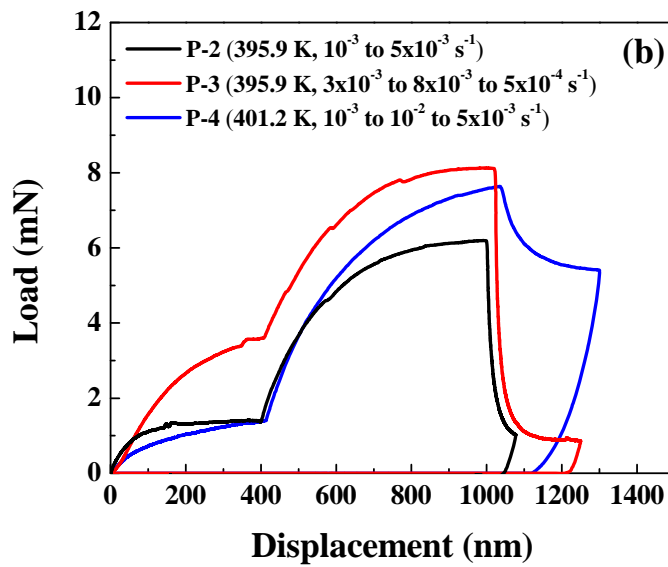
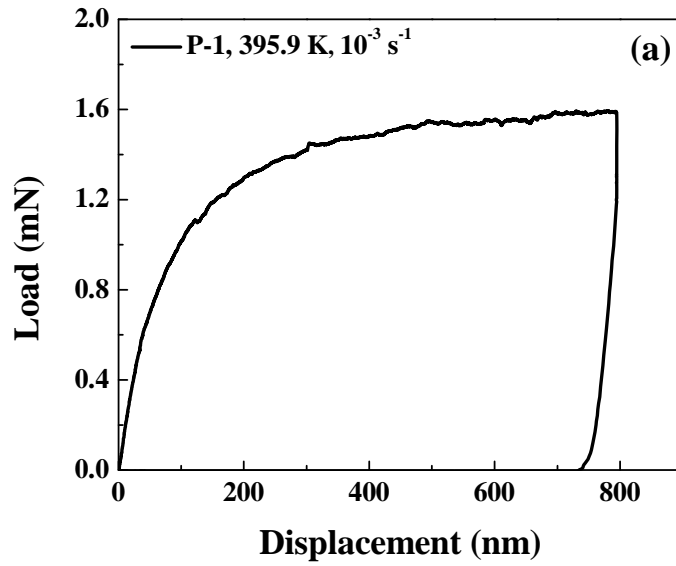


Figure 4.27 The load-displacement curves from microcompression of the Au-based BMG pillar samples at high temperatures: (a) constant strain rate and (b) strain rate change tests.

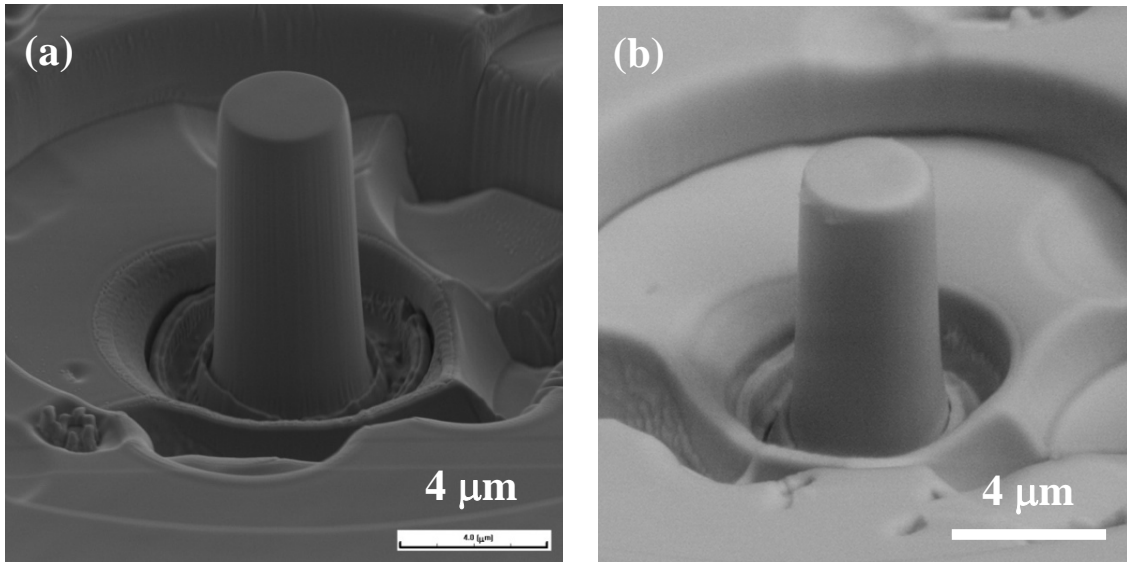


Figure 4.28 SEM images of a typical 3.8 μm Au-based BMG pillar sample (a) before and (b) after compression at 395.9 K with strain rates of 3×10^{-3} – 8×10^{-3} – $5 \times 10^{-4} \text{ s}^{-1}$.

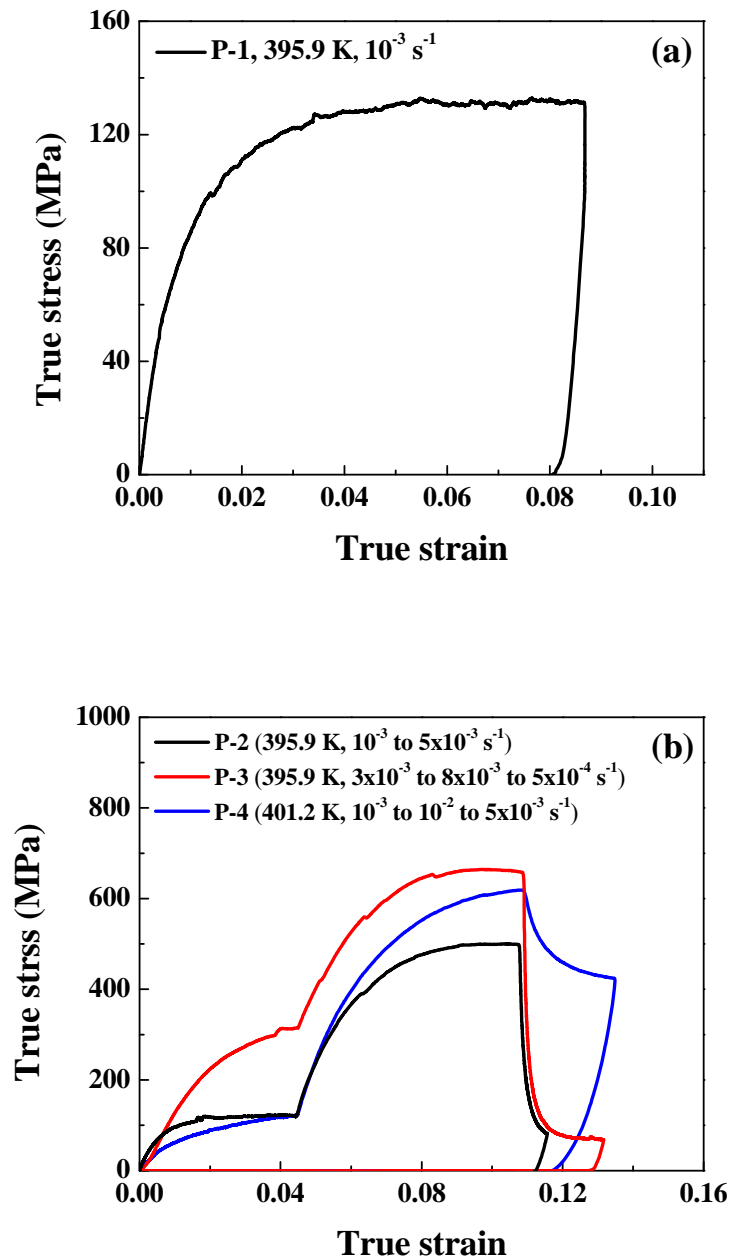


Figure 4.29 True stress-strain curves from microcompression of the Au-based BMG pillar samples at high temperatures: (a) constant strain rate and (b) strain rate change tests.

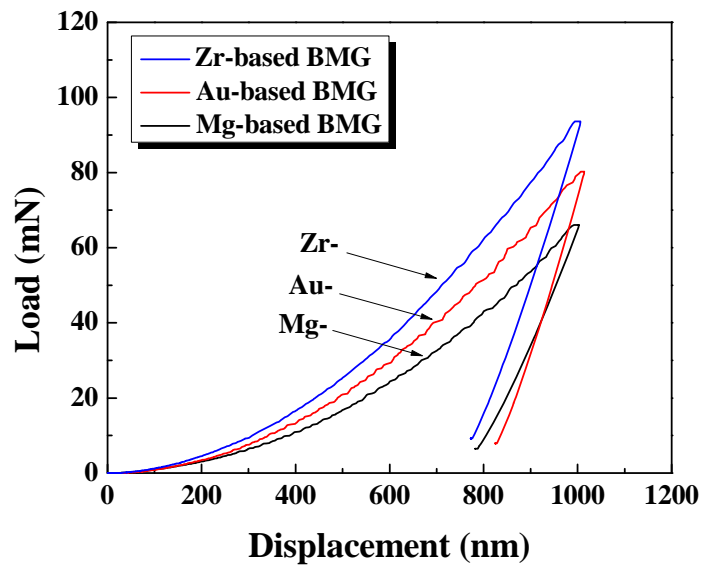


Figure 4.30 The typical load-depth curves of the Mg-, Au- and Zr-based BMGs at strain rate of $5 \times 10^{-2} \text{ s}^{-1}$.

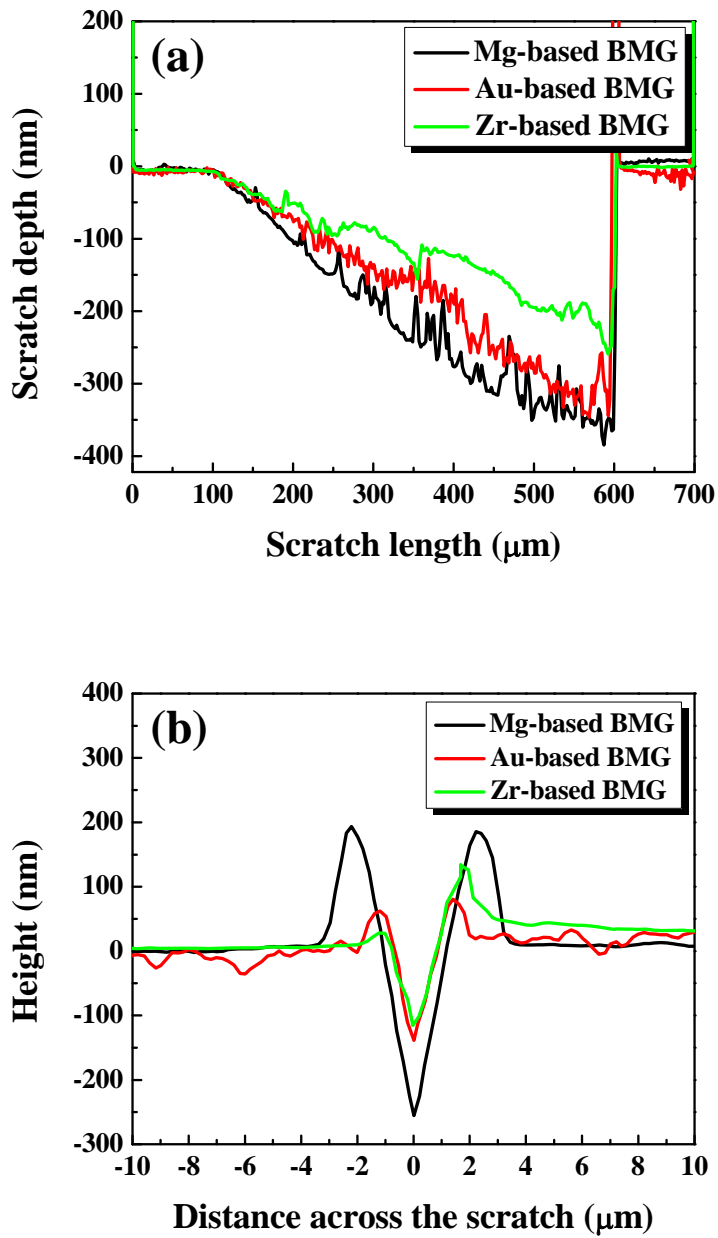


Figure 4.31 (a) Scratch depth profile versus scratch length and (b) cross-sectional profile for the Mg-, Au- and Zr-based BMGs.

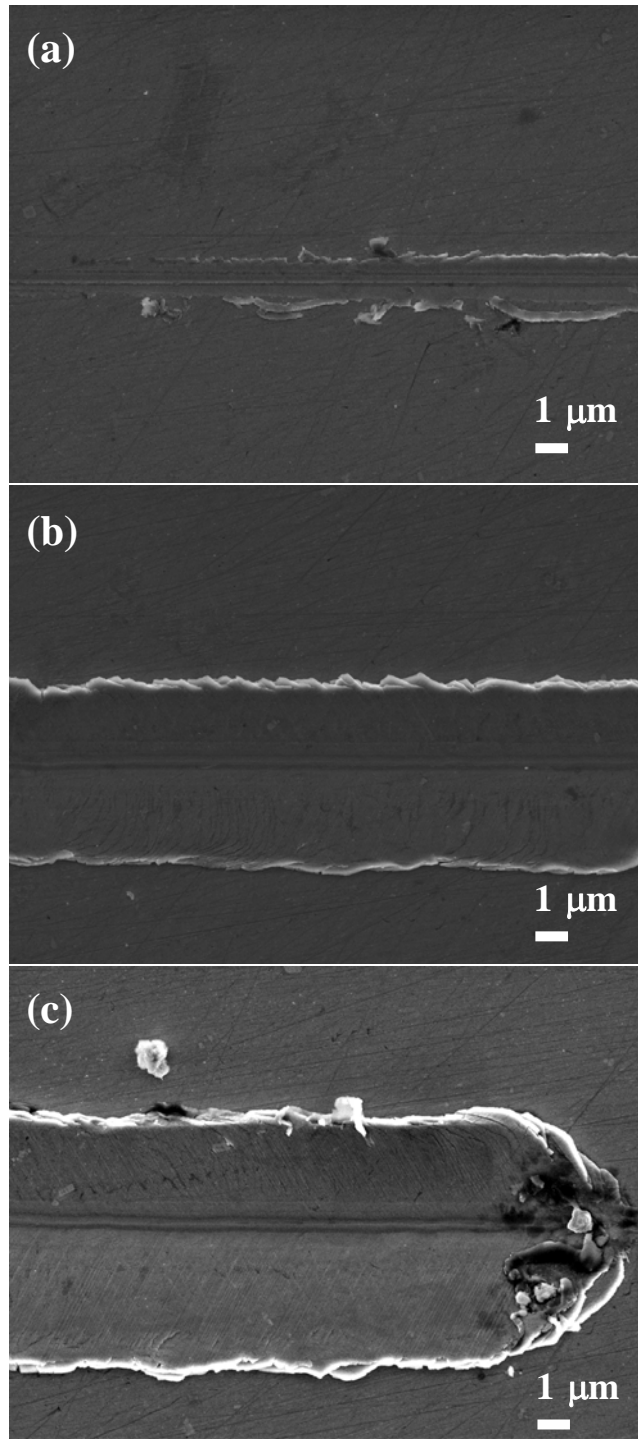


Figure 4.32 SEM images of the scratched regions in the (a) beginning, (b) middle and (c) end of the scratch made in the Mg-based BMG.

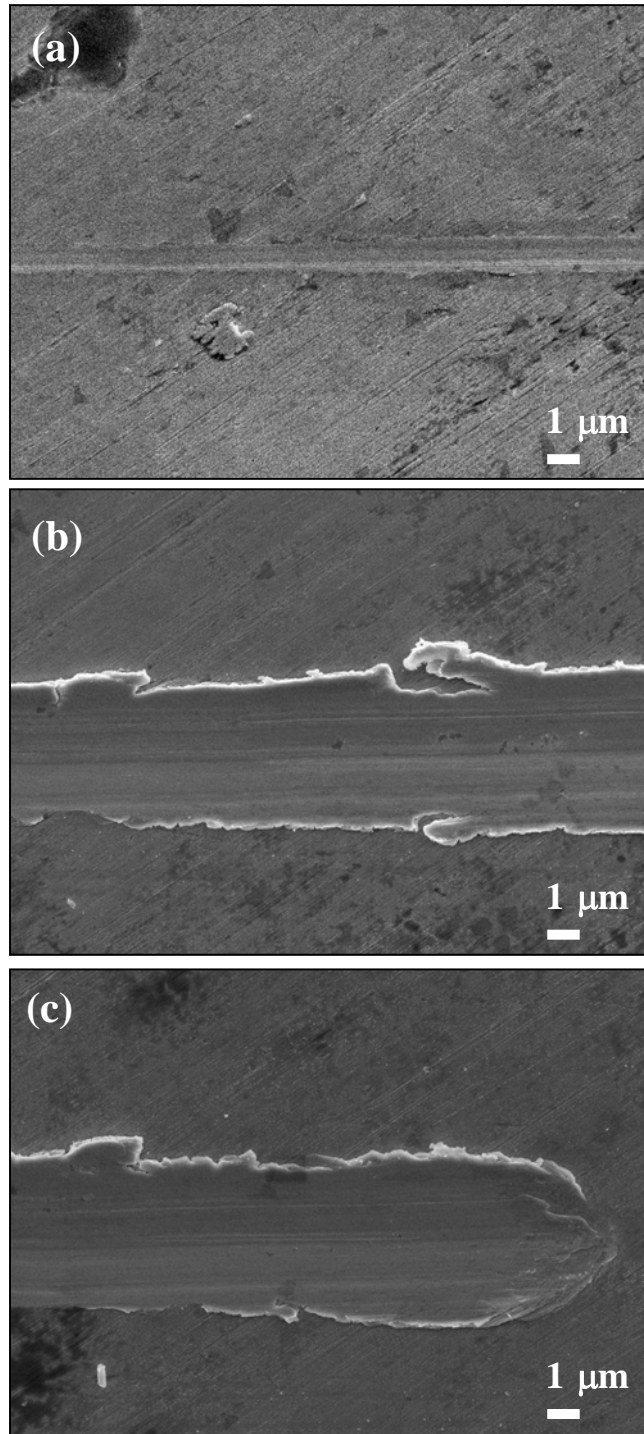


Figure 4.33 SEM images of the scratched regions in the (a) beginning, (b) middle and (c) end of the scratch made in the Au-based BMG.

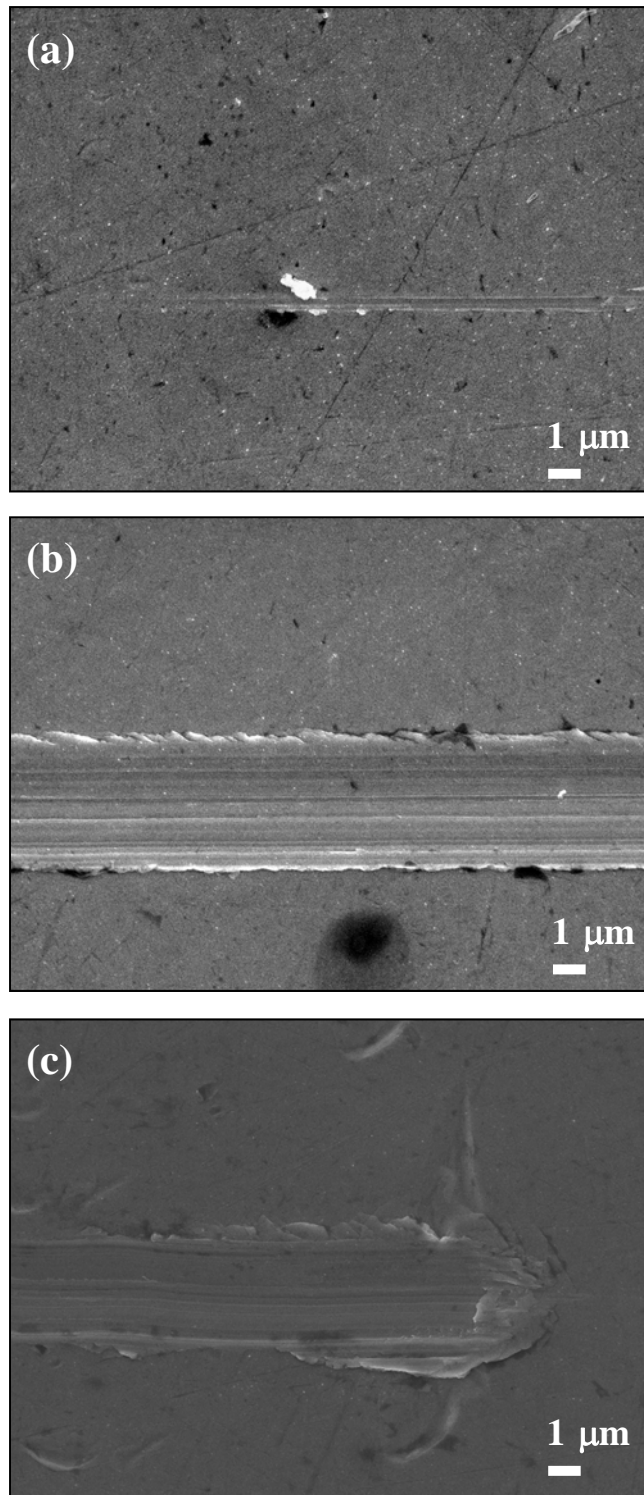


Figure 4.34 SEM images of the scratched regions in the (a) beginning, (b) middle and (c) end of the scratch made in the Zr-based BMG.

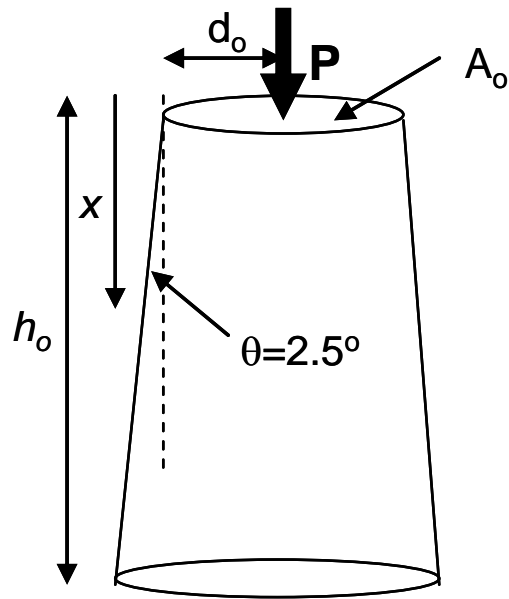


Figure 5.1 Schematic illustration of the deformation for a tapered pillar sample.

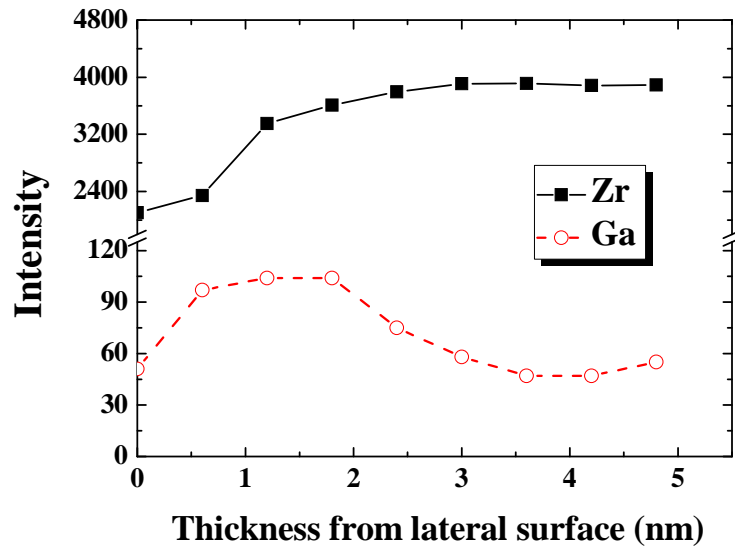


Figure 5.2 AES depth profile of the FIB milled Zr-based BMG micropillar with a diameter of $3.8 \mu\text{m}$.

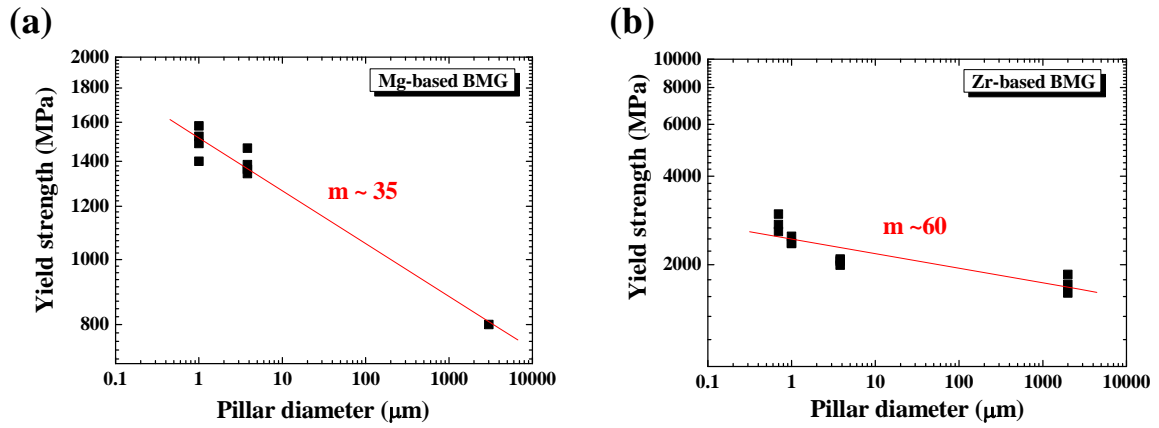


Figure 5.3 The strength-sample size relationship for (a) the Mg-based BMG, and (b) the Zr-based BMG samples with different pillar diameters from 3 mm down to 1 μm , and from 2 mm down to 700 nm, respectively.

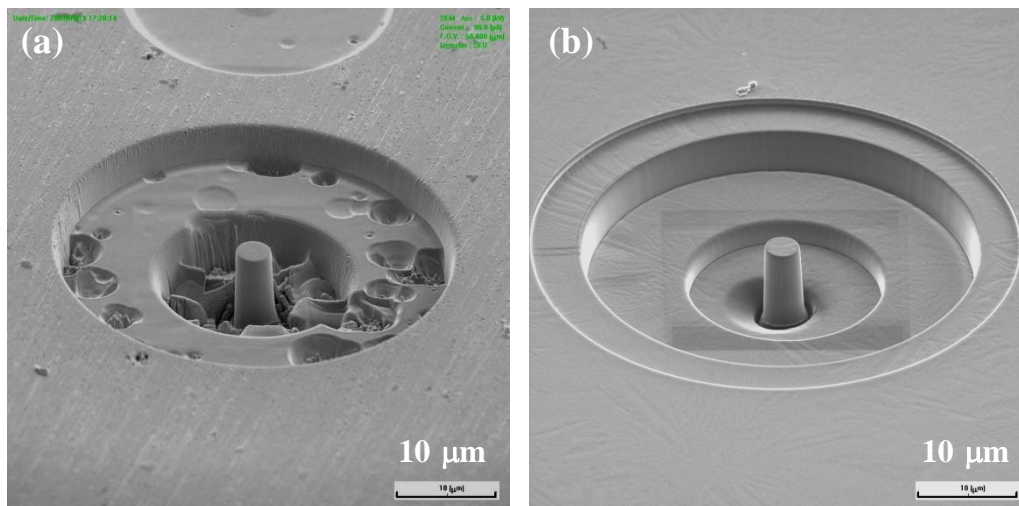


Figure 5.4 The appearance of the 3.8 μm (a) Mg-based BMG and (b) the Zr-based BMG pillar sample after FIB milling.

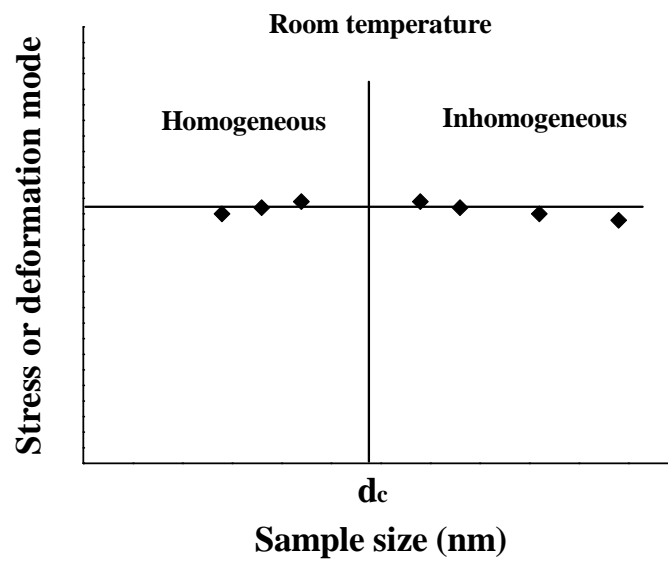


Figure 5.5 Schematic illustration of the sample size effect on homogeneous deformation.

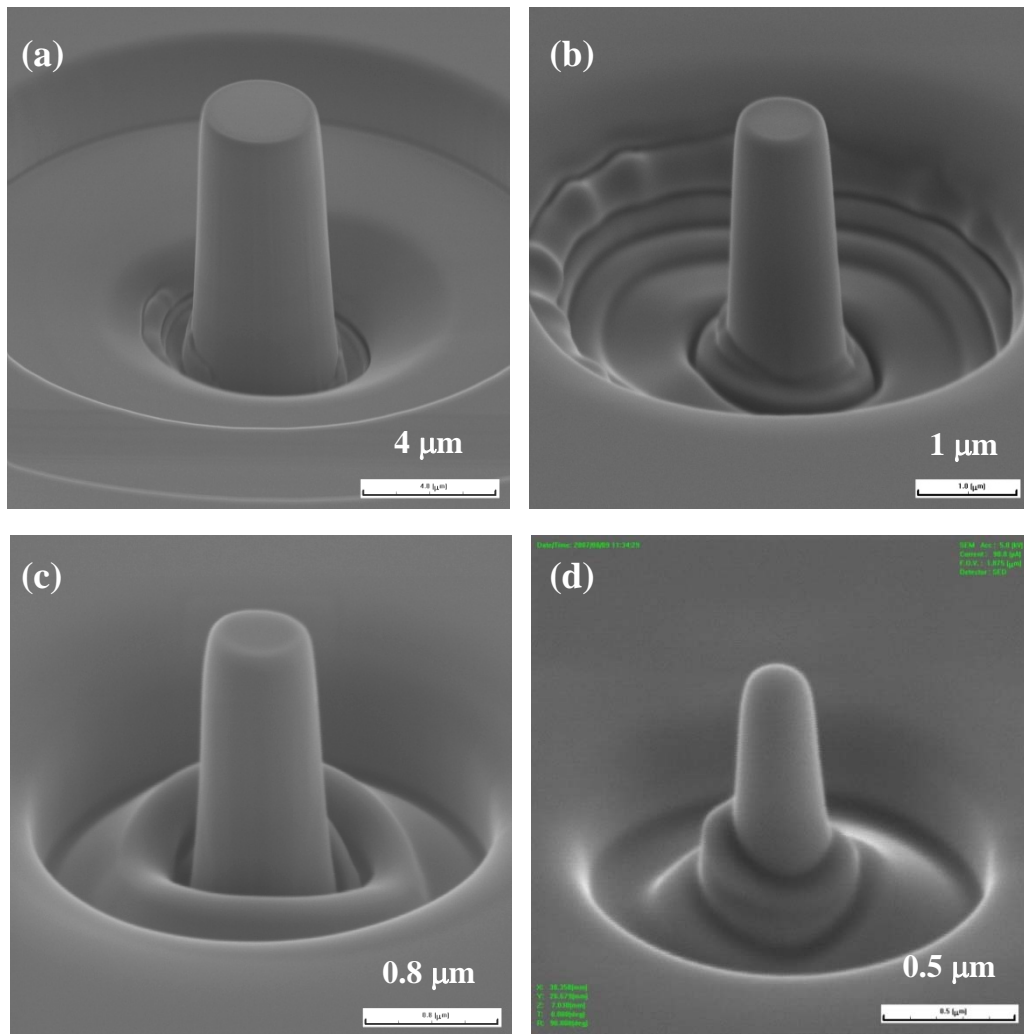


Figure 5.6 The SEM images of the Zr-based BMG pillar sample at the four different sizes: (a) 3.8 μm , (b) 1 μm , (c) 700 nm and (d) 300 nm in diameter.

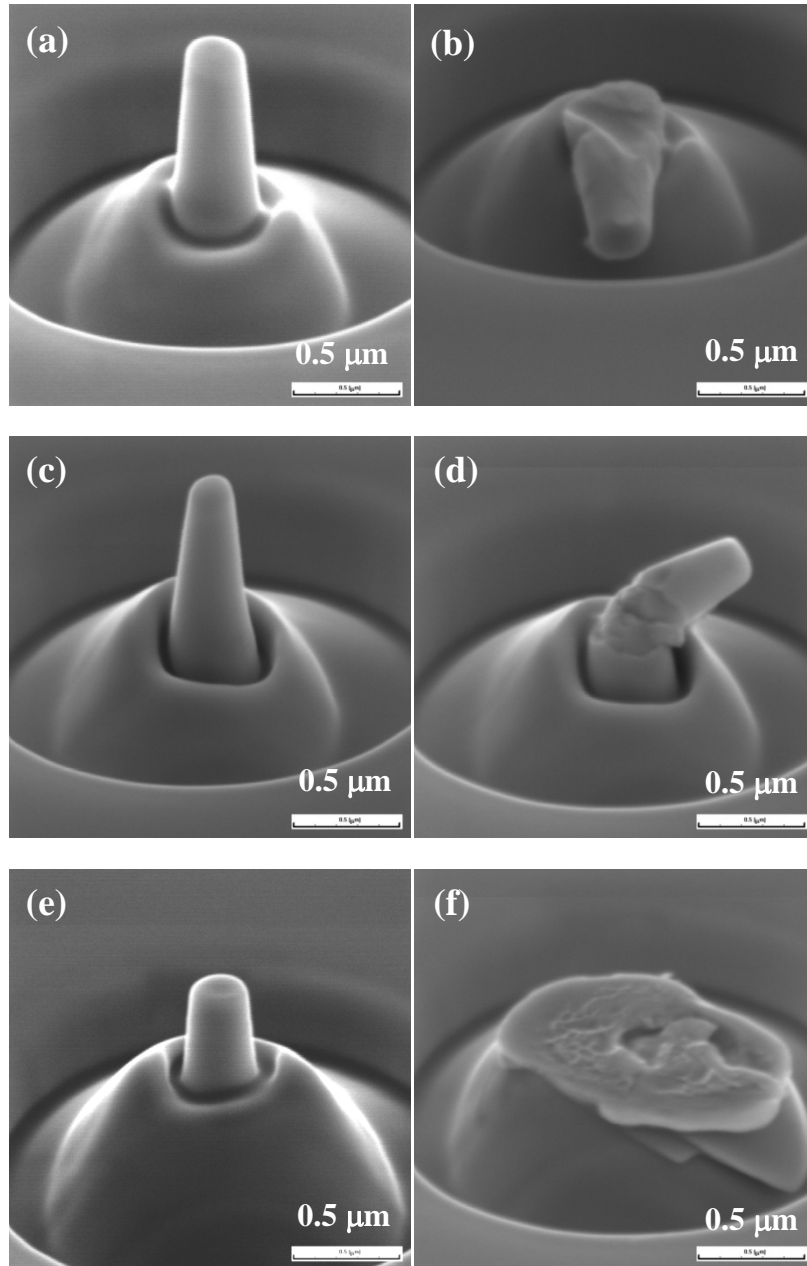


Figure 5.7 The SEM images showing the appearance of the three different 300 nm pillar samples: (a) (c) (e) before and (b) (d) (f) after compression.

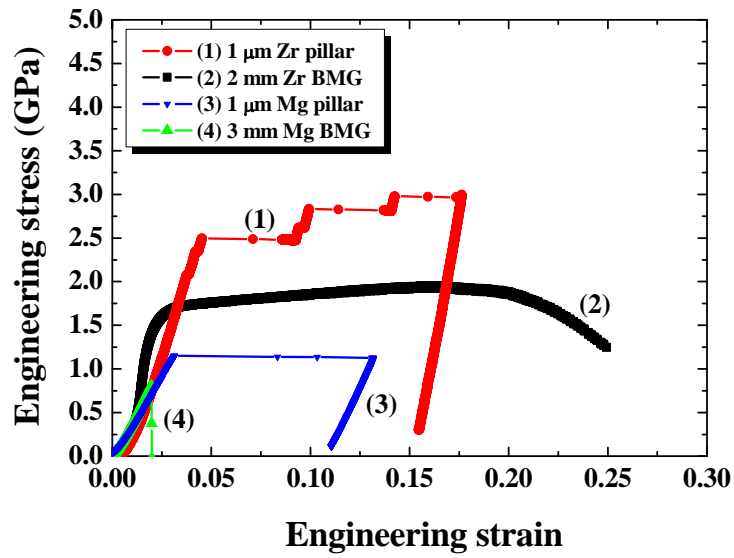


Figure 5.8 The comparison of the curves for the Mg- and Zr-based bulk compression samples, and the 1 μm Mg- and Zr-based micropillars, compressed at the strain rate of 10^{-4} s^{-1} .

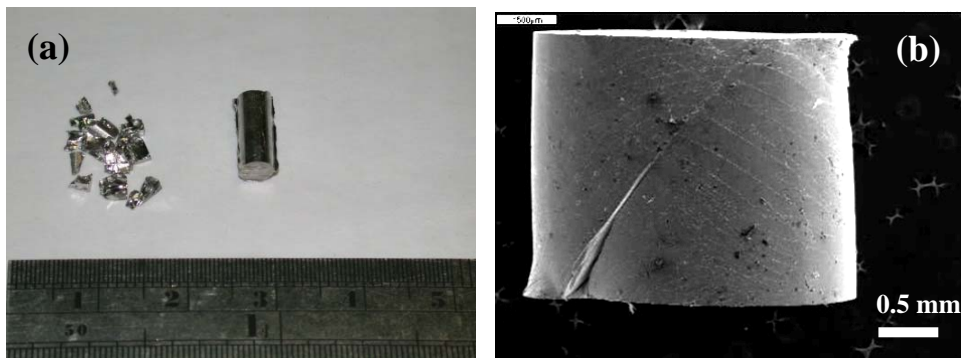


Figure 5.9 SEM micrographs showing the appearance of the deformed (a) Mg- and (b) Zr-based bulk compression samples.

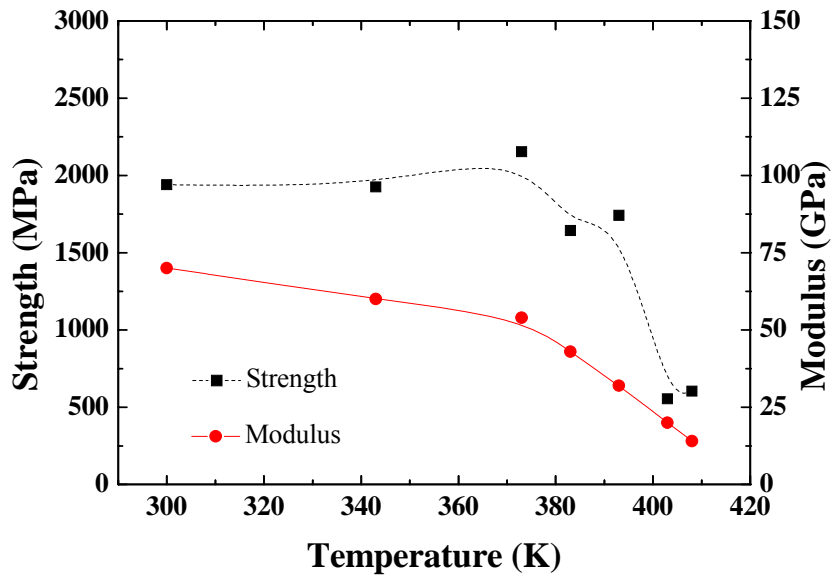


Figure 5.10 The function of temperature versus strength and modulus for the 1 μm Au-based BMG pillar samples at strain rate of $1 \times 10^{-2} \text{ s}^{-1}$.

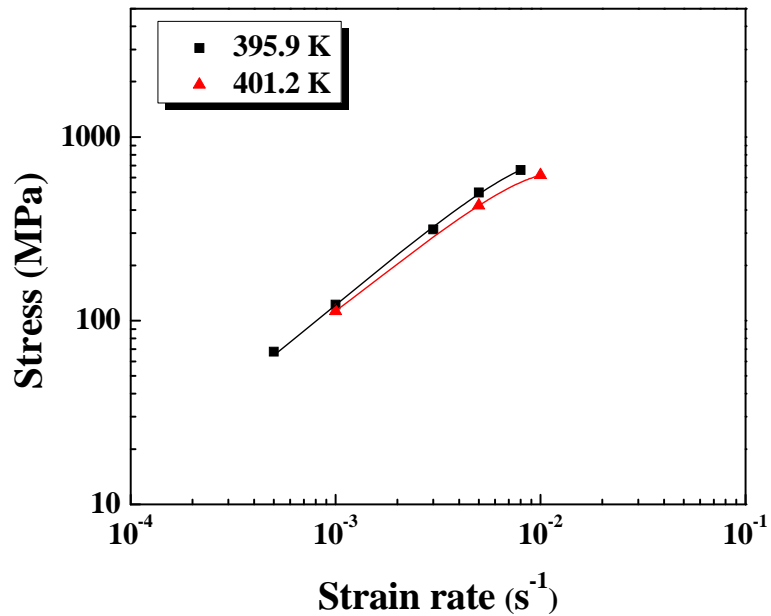


Figure 5.11 Stress vs strain rate for Au-based BMG pillar samples at different temperatures with curves fitted by Eq. (5-1).

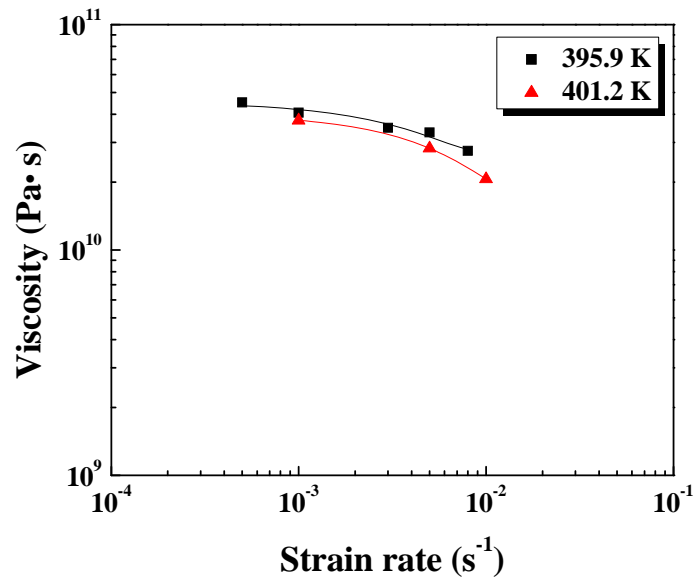


Figure 5.12 Strain-rate dependence of the viscosity in the Au-based BMG.